Development and analysis of Magnetic Resonance Imaging acquisition and reconstruction methods for functional and structural investigation of cardiac and lung tissues.

By

Fabio Gibiino

Thesis submitted for degree of Doctor of Philosophy in Engineering at the engineering school 'Leonardo Da Vinci'. Ph. D. cycle XXVI, Settore Scientifico Disciplinare ING-INF/06

February 2014

Thesis supervisor

Professor Luigi Landini

Supervisors in GE

Doctor Timo Schirmer

Doctor Florian Wiesinger

President of the PhD course

Professor Andrea Caiti

Department of Information Engineering (IET), University of Pisa. Via G. Caruso 16 - 56122 – Pisa, Italy.

A mio padre e mia madre.

ABSTRACT

The imaging of the lung and of the heart are often challenging in magnetic resonance due to the motion of the organs. In order to avoid motion artifacts it is possible to make the acquisition fast enough to fit in the breath-hold, or use some motion management methods in free breathing.

A fast image acquisition can be obtained with non-Cartesian acquisition schemes, which require specialized reconstruction methods. In this work the least-squares non-uniform fast Fourier transform (LS-NUFFT) was compared to the standard gridding (GR) taking the direct summation method (DS) as reference. LS-NUFFT obtained lower root mean square error (RMSE), but heavier geometric information loss. The performance improvement of the LS-NUFFT was studied using three regularization methods. The truncated SVD reduced the RMSE of the simple regularization-free LS-NUFFT.

Alternatively, the scan time can be shortened with some FOV reduction techniques. For cardiac imaging, the inner volume (IV) reduced-FOV selection was explored for the myocardial T_2 mapping. The FOV reduction successfully avoided aliasing and provided a scan time reduction from about 23s to 15s. However, undesired stimulated echoes caused an overestimation in the T_2 of about 20%. The effects of the inner volume excitation on the T_2 mapping were described and clarified.

Finally, motion management was explored for lung imaging in free-breathing, using a non-Cartesian acquisition trajectory. The rotating ultra-fast sequence (RUFIS) was demonstrated to be very suitable for the short T_2^* lung tissue. The respiratory motion was addressed with three methods: prospective triggering (PT), prospective gating (PG) and retrospective gating (RG). All methods were able to reconstruct a 3D high-resolution dataset. PG and RG could achieve 1.2 mm isotropic resolution in clinically reasonable scan time (~6min). The RG sequence could reconstruct multiple phases of the respiration cycle at cost of higher scan time.

Keywords: non-Cartesian acquisition, reconstruction, LS-NUFFT, geometric information, cardiac, T_2 mapping, inner volume, lung, RUFIS, navigators.

INDEX

LIST OF SIMBOLS AND ABBREVIATIONS

MRI: magnetic resonance imaging

RF: radio-frequency pulse

B_0: static magnetic field in the magnet

B_1: time-varying magnetic field associated with the RF

T_1: longitudinal relaxation time

T_2: transverse relaxation time

PD: proton density

TE: echo time

TR: repetition time

FA: flip angle

FOV: field of view

PE: phase encode

FE: frequency encode

SNR: signal-to-noise ratio

FFT: fast Fourier Transform

IDFT: inverse discrete Fourier Transform

DCF: density compensation function

LS-NUFFT: least squares non-uniform FFT

GR: gridding method with Keiser-Bessel interpolator

DS: direct summations method

RMSE: root mean square error

SL: Shepp-Logan (digital phantom)

τ: width of the 2D autocorrelation peak

τ_{rand}: width of the 2D autocorrelation after the pixel location randomization

G: geometric information loss index

R_τ: measure of the 2D autocorrelation peak anisotropy

VSD: variable density spiral

PSF: point spread function

TSVD: truncated singular value decomposition

TR: Tikhonov regularization method

L1R: L_1 regularization

q: size of the LS-NUFFT interpolator

GCV: generalized cross validation

FSE: fast spin echo

MEFSE: multi-echo FSE

ETL: echo train length in the FSE

rFOV: reduced FOV

IV: inner volume

2D-RF: multi-dimensional spatially selective pulses

ROI: region of interest

SLR: Shinnar-Le Roux transform

STE: stimulated echo

RUFIS: rotating ultra-fast imaging sequence

ZTE: zero-echo time

UTE: ultra-short echo time

FID: free induction decay

DC: static/ zero frequency

N_{avg}: number of averages

BW_{Rx}: receive bandwidth

PT: prospective triggering

PG: prospective gating

RG: retrospective gating

MIP: maximum intensity projection

INTRODUCTION

Magnetic Resonance Imaging (MRI) is an important medical technique extensively used for diagnostic purposes. MRI produces images of the human body showing anatomical and functional information with a level of details unimaginable only a few decades ago. MRI has been invented around the early 1970s and today thousands of MRI scanners are spread all over the world giving crucial information for medical diagnosis.

MRI is based on the sensitivity to the presence and properties of water in the human body. In the case of disease or injuries, the properties and amount of water in tissue can significantly change, hence making MRI a suitable technique for diagnostic. MRI uses non-ionizing radiations, thus it is generally considered not to be dangerous for the human body. Besides the anatomical information, MR is able to obtain functional or metabolic information as well.

In MRI the patient is put in a strong static magnetic field, generally referred as B_0, which generates an equilibrium state in the proton spins of the tissues. The spins in the tissues tend align to the static magnetic field, ending up in a precession motion around B_0. The precession motion is associated to a frequency called Larmor frequency, which is dependent on the static magnetic field strength and on the imaged nucleus. The most frequently imaged nucleus in magnetic resonance is the hydrogen (H). For H imaging at 1 Tesla magnetic field, the Larmor frequency is about 42MHz.

The equilibrium state of the spins is perturbed by electromagnetic pulses at the Larmor frequency as central frequency. The phenomenon of giving energy to the spins at the same precession frequency is called ‘resonance’ and that is where the imaging technique takes the name from.

After the radio-frequency (RF) pulse excitation, the spins try to go back to their equilibrium state with a speed dependent on the magnetic properties of the tissues. After excitation, the longitudinal magnetization signal (parallel to B_0) increases getting back to the equilibrium state value with an exponential law. Conversely, the signal on the transversal plane (perpendicular to B_0) decreases exponentially to zero. A receiving coil acquires the time-varying magnetic signal generated on the transversal plane by the spins while going back to equilibrium [1].

On the basis of these principles, MR is capable of acquiring enough information to reconstruct detailed images of the human body. Spatially-varying magnetic fields (generally referred as

gradients) are used to distinguish the spatial origin of the acquired signals. Three gradients applied on the different spatial directions are used in order to obtain a slice-encode (z axis), a phase-encode (y axis) and a frequency-encode (x axis). The gradients allow acquiring 2D or 3D image datasets, which need to be reconstructed with the Fourier Transform. In MRI, the physical magnetization vector is considered as phasor, with real and imaginary part. The acquired signal is an integration of all the spin phasors contribution from the whole imaged volume. From this consideration, the acquired signal fills the Fourier domain (k-space) and a Fourier transform is needed to obtain the desired image in the space domain [2].

Motion during the acquisition is one of the most common sources of artifact for MRI. During the acquisition the location of the spins is assumed not to change. However it is often difficult to keep organs still for a time long enough to acquire the interesting signals. Respiration is an example of motion that cannot be interrupted for a long time. The heart-beating is an example frequent and uncontrolled movement which needs careful management to prevent from artifact formation. The easiest way to avoid motion artifacts is to stop the motion during the acquisition. For the respiratory motion, the acquisition can be accelerated to fit in the breath-hold. Alternatively the motion can be left running free, but some motion management needs to be adopted. For cardiac motion, the heart beat cannot be interrupted; hence it is common to synchronize the acquisition with a specific phase of the heart cycle (e.g. diastole).

In this work of thesis the cardiac and lung imaging and reconstruction techniques have been investigated. The work is divided in two main sections. The first section is focused on reconstruction techniques from fast acquisition schemes, which better fit the acquisition in the breath-hold. Non-Cartesian sampling of the k-space is a good way to keep the acquisition fast and reduce the echo time (TE) as much as possible. An analysis of the reconstruction method performance for non-Cartesian datasets is presented in this work. First a study is presented on the reconstruction error and the geometric information loss associated with the reconstruction method. Secondly three regularization methods are presented and applied to the reconstruction method in order to improve its performance.

The second section is focused on pulse sequence development. This topic is required solving problems of both software engineering and MRI physics.

In the first place a sequence was developed for cardiac applications. In the case of heart imaging, both cardiac and respiratory motions need to be managed in order to avoid motion artifacts.

Regarding respiratory motion, breath-holding during the acquisition was adopted in order to avoid artifacts. Regarding cardiac motion, the acquisition was synchronized to the diastole using the ECG signal. The inner volume excitation was explored as scan acceleration method in order to comfortably fit the acquisition in the breath-hold. The T_2 mapping was chosen cardiac application to accelerate. The T_2 mapping is a quantitative imaging technique which requires the acquisition of the same T_2 weighted cardiac image multiple times at different TE. Therefore, the scan time can easily exceed the breath-hold.

The sequence development was focusing on lung imaging as well, presented in the second part of the second section. In this case the acquisition was rendered as fast as possible using a radial acquisition in the K-space. However the breath-hold might not be long enough to acquire all the necessary data, especially for 3D datasets. Therefore the respiration was kept running free using some motion management methods. The motion managements were implemented in a zero-TE sequence, very suitable for acquiring the short lived signal of the lung.

Finally some tests were performed in order to merge the skills gained in both cardiac and lung imaging. The same approach used for the lung imaging sequence was used for the cardiac imaging as well.

1. SECTION 1: RECONSTRUCTION TECHNIQUES

1.1. INTRODUCTION

As mentioned above, the MRI technique acquires signal filling the k-space of the desired image. The acquisition needs to be as fast as possible in order to better fit the scan in the breath-hold, or to acquire the signal before its quick decay.

Methods to obtain a rapid acquisition include echo planar imaging [3], compressed sensing [4], and parallel imaging with restriction to multi-channel receiver coils [5, 6]. Alternatively, non-Cartesian trajectories, e.g. spirals [7, 8], can be used to rapidly fill the k-space and thus accelerate the scan. Non-Cartesian trajectories starting the acquisition from the center of the k-space acquire most of the relevant information of the image before the signal decays.

Handling non-Cartesian data is a problem widespread in many different areas. Besides MRI, non-Cartesian samples are acquired, for example, in radio astronomy [9], or in several kinds of medical imaging techniques [10, 11]. Cartesian trajectories are often preferred in MRI because Fast Fourier Transform (FFT) can be used directly in this case. If N is the number of input data, then $O(N \log(N))$ will be the computational complexity of FFT, so FFT will be very fast. On the other hand, Non-Cartesian trajectories like spirals can fill the k-space with attractive performances. They can obtain variable sampling density on the k-space. Spirals sample fewer data, thus shortening acquisition time and they oversample the center of the k-space, thus reducing movement artifacts. However, FFT cannot be used directly, because FFT requires evenly spaced samples in input, and this is the main disadvantage of non-Cartesian data. Specialized reconstruction methods are needed to obtain image in the spatial domain in a reasonable time. Fig. 1 shows an example of spiral acquisition trajectory compared to a Cartesian sampling pattern.

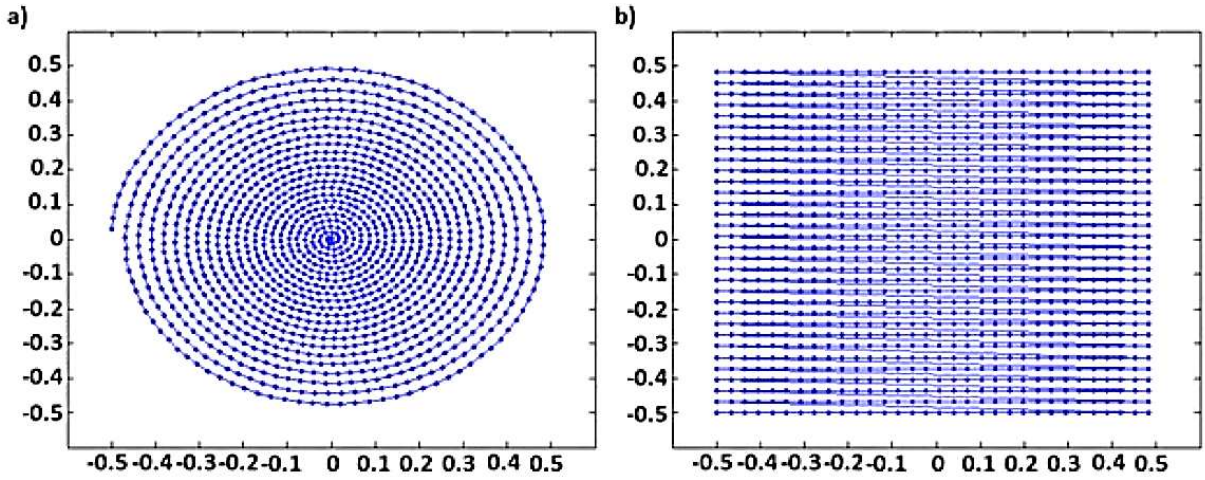

Fig. 1 *Example of a) spiral trajectory, b) Cartesian trajectory*

Several reconstruction methods have been proposed in literature [12 - 15]. Direct Summation (DS) method [16, 17] is usually taken as reference method because it directly applies the definition of the Inverse Discrete Fourier Transform (IDFT). Most reconstruction methods need to compensate the variable sampling density on the k-space. The compensation function is usually called Density Compensation Function (DCF). Extensive work has been presented in literature regarding the optimal choice of DCF [18]. In this work of thesis the term *gridding* is referring to any reconstruction method performing an interpolation followed by FFT. The interpolation evaluates data onto Cartesian grid of k-space, so FFT can then be used. The most common gridding reconstruction uses a Keiser-Bessel window interpolator before applying the FFT [19, 20]. In this work the Keiser-Bessel gridding method will be referred as GR.

In this work, the attention has been mainly focuses on a gridding method called Least Squares Non-Uniform Fast Fourier Transform (LS-NUFFT) [21 - 24]. LS-NUFFT is a development of NUFFT [25]. NUFFT uses a Gaussian operator, which has been shown to be effective in several applications [26, 27]. LS-NUFFT is supposed to obtain good performance thanks to a pseudo inverse matrix guiding the choice for gridding interpolator.

LS-NUFFT was analyzed under two main aspects. The geometric information loss of the reconstruction method was introduced and analyzed for both LS-NUFFT and GR. Additionally three regularization techniques were applied to LS-NUFFT in order to reduce the reconstruction error using a wider interpolation kernel.

1.2. THEORY: RECONSTRUCTION METHODS

In this section the reconstruction methods used in the present work are described. An explanation will be given of the characteristics of the DS method (which is taken as reference), the GR method and the LS-NUFFT method (obtained as a development from NUFFT).

1.2.1. Direct Summation (DS)

In principle, a perfect reconstruction of an MR image would require a continuous two-dimensional Fourier transform applied to a continuous acquired k-space.

Ideally, the general relationship between the space image $I(\vec{r})$ and the signal $S(\vec{k})$ acquired by the MR scanner is determined by the inverse Fourier Transform:

$$I(\vec{r}) = \int S(\vec{k}) e^{i\vec{k}\cdot\vec{r}}\, d\vec{k}. \tag{1}$$

Vector $\vec{r}$ represents the space location and $\vec{k}$ represents the frequency location in the k-space. In practice it is only possible to acquire a finite number of samples (N_s) on the k-space, so the Inverse Discrete Fourier Transform (IDFT) has to be used to reconstruct the image. Discrete Fourier Transform and its inverse are well-known tools that keep on being analyzed also in recent works [28, 29]. DS method simply uses the definition of the IDFT in the case of non-Cartesian trajectories. Let us consider the mono-dimensional version of IDFT for simplicity:

$$I_j = \sum_{h=0}^{N_s-1} S_h e^{i\omega_h \cdot j\Delta x}\, \Delta\omega_h \quad j = 0 \dots M-1, \tag{2}$$

I_j is the value of IDFT at location j. Δx is the sample spacing of the IDTF, $j\Delta x$ is the discrete space location and M is the number of reconstructed space locations. ω_h is the sampled pulsation (i.e. the discrete 1D version of vector $\vec{k}$) and N_s is the number of samples on the non-uniform trajectory. S_h represents the sampled data at the discrete k-space location ω_h.

$\Delta\omega_h$ is the discretized integration interval. If the acquisition trajectory is Cartesian, $\Delta\omega_h$ does not depend on h. For non-Cartesian trajectories, the use of an adaptive $\Delta\omega_h$ avoids overweighting the samples acquired in heavily sampled areas of the k-space. Hence, the previously introduced DCF function equals $1/\Delta\omega_h$. The value of $\Delta\omega_h$ can be calculated using the Jacobian of the trajectory mathematical expression [30]. Alternatively $\Delta\omega_h$ can be determined using the Voronoi diagram

[31, 32] using the area of the region associated with each point of the trajectory on the k-space. A spiral trajectory with one interleave is shown in Fig. 2a with the associated Voronoi diagram in Fig. 2b.

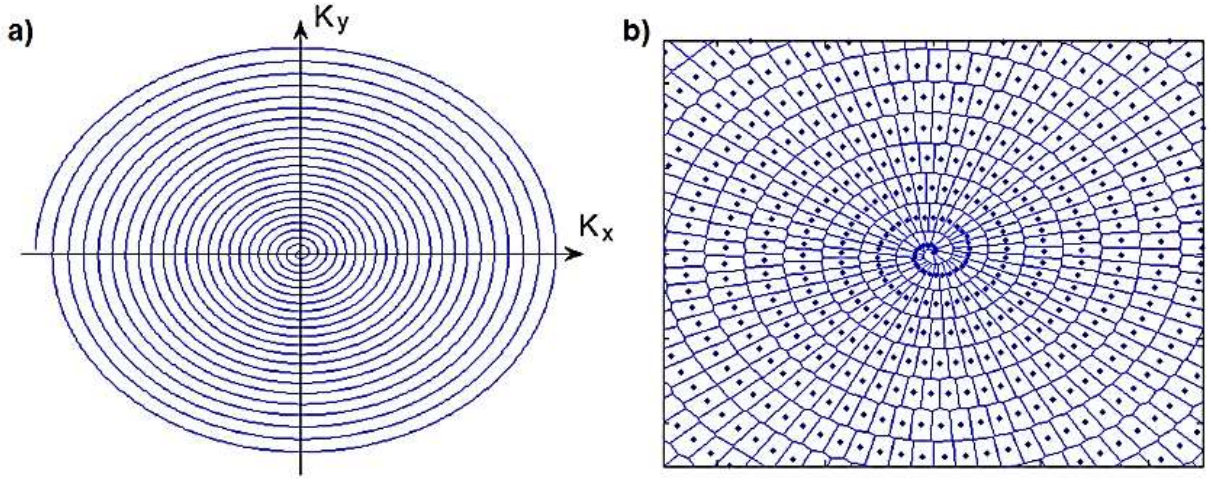

Fig. 2 *: a) Example of spiral trajectory with one interleaf. The centre of the K-space is sampled with higher density than periphery. b) Zoomed Voronoi diagram of a spiral trajectory with only one interleave.*

The main disadvantage associated with the DS method is the high computational complexity. If N_s samples are acquired and the reconstructed image is defined on M^2 pixels, then the computational complexity equals $O(M^2N_s)$.

1.2.2. Gridding reconstruction (GR)

The use of the FFT algorithm makes the gridding reconstruction method fast. Before using FFT, sampled data need to be interpolated on a Cartesian grid. The interpolation process is called '*gridding*'.

Considering the 1D case, S is the sampled data (i.e., the signal) and DCF the density compensation function depending on the chosen trajectory [12]. DCF is proportional to the inverse of the $\Delta\omega_h$ mentioned in the previous section. C is a chosen convolution kernel and III is the Cartesian grid where data are to be interpolated. The gridding process can thus be summarized as follows:

$$S_g = \{[(S/DCF)\otimes C]\cdot III\}\otimes^{-1} C\,, \tag{3}$$

where S_g represents the gridded data and $\otimes$ is the convolution operator. Gridding is done with three main steps i) convolution between density compensated data and a chosen kernel C ii) re-sampling data onto a Cartesian grid iii) scaling of the space image. Scaling corresponds to deconvolve ($\otimes^{-1}$) the obtained dataset with C in the frequency domain. The extension to 2D case is straightforward.

In this work, a 4-pixel-wide Kaiser-Bessel (KB) window was used as C kernel. The Kaiser-Bessel function is defined as follows:

$$\psi(k) = f_J^m(k)\frac{I_m\left(\alpha f_J(k)\right)}{I_m(\alpha)} \tag{4}$$

Where I_m represents the modified Bessel function of order m, α is a parameter that determines the shape, and

$$f_J(k) = \begin{cases} \sqrt{1-\left(\dfrac{k}{J/2}\right)^2}, & |k| < \dfrac{J}{2} \\ 0, & otherwise. \end{cases} \tag{5}$$

The interpolation was calculated on a two-fold field-of-view (FOV) to reduce aliasing as suggested in [12]. The Voronoi areas associated with the trajectory were used to calculate 1/DCF.

The interpolation of GR can be represented with a linear operation $S_g\otimes C = TDS$. Matrix T is the interpolator. D is the diagonal matrix with *1/DCF* on the diagonal. Kernel C can be defined to be non-zero on a very small number of points. This allows matrix T to be sparse and makes gridding very fast. Finally reconstruction is obtained with the inverse FFT algorithm applied to S_g. The computational complexity of the convolution step is strictly dependent on the width (w) of the convolution kernel. The number of multiplication required for the convolution equals $N_s w^2$ in the 2D case. The complexity associated to the 2D FFT algorithm is $O(M^2 log(M^2))$. The total computational complexity is $O(M^2 log(M^2) + N_s w^2)$ for 2D GR. The M^2 multiplications needed for final space scaling have little importance in this evaluation.

1.2.3. Least Squares Non Uniform Fast Fourier Transform (LS-NUFFT)

LS-NUFFT has been developed on the basis of NUFFT method. NUFFT was introduced for the first time by Dutt and Rokhlin [14] and is based on the approximation of a complex exponential. According to reference [25], the following 1D approximation can be written:

$$e^{i\omega_h x} e^{-bx^2} \cong \sum_{k=[\omega_h]-\frac{q}{2}}^{[\omega_h]+\frac{q}{2}} \rho_k(\omega_h) \cdot e^{ikx}, \tag{6}$$

Where $\alpha(\omega_h)$ denotes the integer value closest to ω_h. This expression is valid if $b > 0.5$ and $\omega_h > 0$ are real numbers. It is also required that $q \geq 4b\pi$ is an integer number and $x \in [-\pi,\pi]$. We can consider ω_h as pulsation and x as space coordinate. $\rho_k(\omega_h)$ can be expressed as:

$$\rho_k(\omega_h) = \frac{1}{2\sqrt{b\pi}} e^{-\frac{(\omega_h - k)^2}{4b}}. \tag{7}$$

Defining $x \in \left[-\frac{M}{2}\Delta x, \frac{M}{2}\Delta x\right]$, $c = \left[\frac{\omega_h mM\Delta x}{2\pi}\right]$, $\alpha_h = S_h \cdot DCF^{-1}$ and $m \geq 2$ an integer number, Eq. 6 can be used in the definition of IDFT expressed in Eq. 2 obtaining what follows ([25, 23]):

$$I_j \cong \frac{1}{e^{-b\left(\frac{j2\pi}{mM}\right)^2}} \sum_{k=c-\frac{q}{2}}^{c+\frac{q}{2}} \sum_{h=0}^{N_s-1} \alpha_h \cdot \rho_k(\omega_h) \cdot e^{ik\left(\frac{j2\pi}{mM}\right)} \tag{8}$$

Eq. 8 shows that every pixel in the reconstructed image is obtained with two summations. The inner summation performs an interpolation of data on equidistant frequency locations k. The outer summation is an IDFT that can be performed using FFT. Interpolators are often used to make the reconstruction process faster. Interpolation uses a window of the samples to determine the value of Fourier transform on the interesting Cartesian locations. The width and shape of the window affects the quality of the reconstructed image. If the width is kept low, the reconstruction can be faster. In Eq. 8, parameter q represents the number of samples used by the interpolator.

NUFFT is a gridding method that uses a Gaussian interpolator [17] and can be compared to the classical gridding proposed by Jackson et al. [12], (i.e. what is called GR in this work). The

factor *m* is increasing factor for the FOV to reduce aliasing (FOV = M·Δx). $\rho_k(\omega_h)$ is the interpolator and its width depends on parameter *q*. $\rho_k(\omega_h)$ is a *(q+1)×N* matrix in which *k* identifies the row and *h* the column. The scaling factors in the spatial domain are represented by $e^{-b\left(\frac{j2\pi}{mM}\right)^2}$.

LS-NUFFT is a development of NUFFT that was presented by Nguyen and Liu [21] and uses scaling factors different from Gaussian. Let s_j be the scaling factors and $w=e^{i\frac{2\pi}{mM}}$, then we can write a generalization of Eq. 6 as follows:

$$s_j w^{jm\omega_h} = \sum_{k=[m\cdot\omega_h]-\frac{q}{2}}^{[m\cdot\omega_h]+\frac{q}{2}} \rho_k(\omega_h)\cdot w^{jk} \tag{9}$$

The user needs to choose the scaling factors. The interpolator $\rho_k(\omega_h)$ is determined using a pseudo inverse matrix. We can rewrite Eq. 9 using matrix notation:

$$v_j(\omega_h) = A\rho(\omega_h) \quad j = 0...M-1 \tag{10}$$

with $v_j(\omega_h) = s_j w^{jm\omega_h}$ and matrix A gathers all factors w^{jk}. A is a Fourier matrix and has size $M\times(q+1)$. Finally the interpolator that minimizes $\left\|A\cdot\rho_k(\omega_h) - v(\omega_h)\right\|_2^2$ can be obtained using the Moore-Penrose pseudoinverse matrix:

$$\rho_{LS} = A^{\dagger}v(\omega_h) = \left(A^H A\right)^{-1} A^H v(\omega_h) \tag{11}$$

Matrix A^H is the conjugate transpose of *A*. The interpolator in Eq. 11 has been extensively studied by Fessler and Sutton [22]. Fessler and Sutton have shown that ρ_{LS} is the interpolator that minimizes the maximum approximation error. A 2D version LS-NUFFT has also been applied on medical imaging [23].

The number of multiplications required for the interpolation is $N_s q^2$ in the 2D case. The complexity associated with the 2D FFT algorithm is $O(M^2 log(M^2))$. The total computational complexity is $O(M^2 log(M^2)+N_s q^2)$ for both 2D NUFFT and LS-NUFFT.

The calculation of the interpolator before reconstruction is the only computational difference between NUFFT and LS-NUFFT.

1.3. GEOMETRIC INFORMATION LOSS

The performance of the reconstruction methods is generally evaluated using the error image. The error image is calculated as difference image between the reconstruction image of the tested method and the reconstructed image of the reference method (typically DS). The error image basically corresponds to the difference image. In literature, often the root mean square error (RMSE) [23] has been evaluated in order to estimate the performance of the reconstruction method. Fig. 3 shows an example of this comparison, described in [23] for *in vivo* experiments.

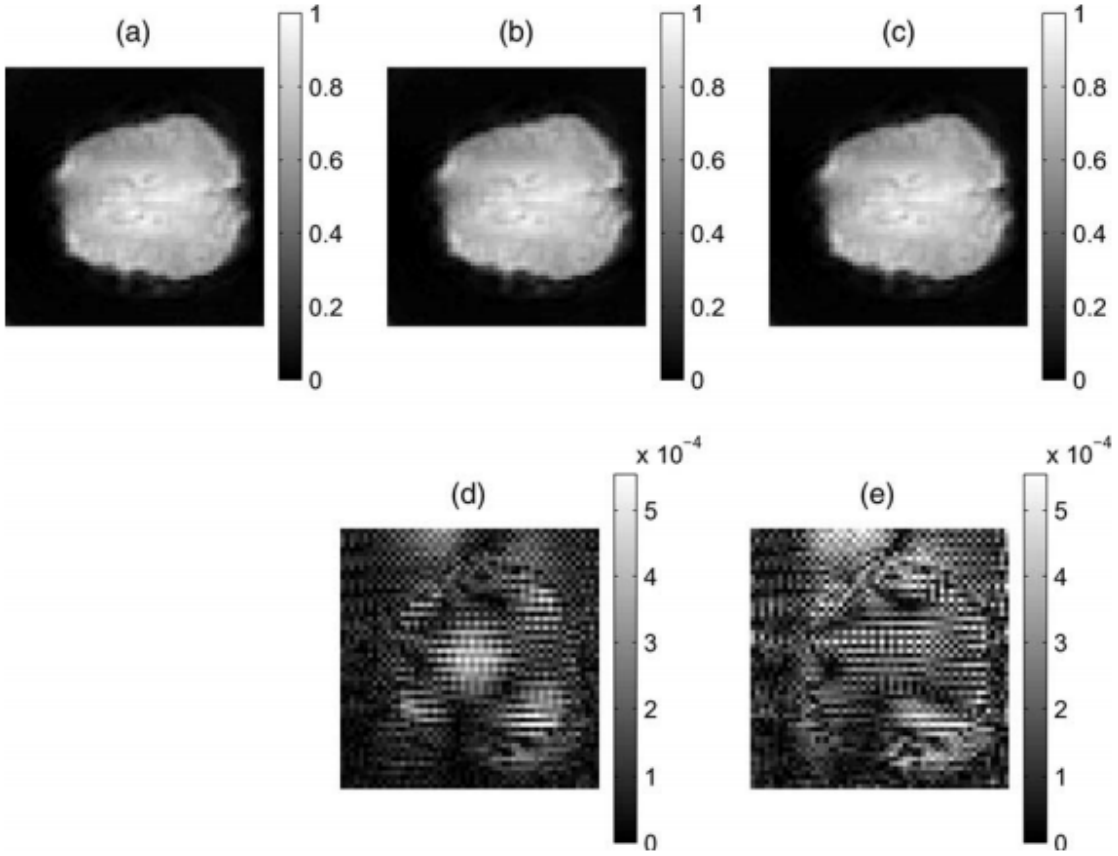

Fig. 3 *Comparison of LS-NUFFT and GR methods using in vivo experiment data, taken from [23]: (a) DS, (b) LS_NUFFT, (c) GR (d) Absolute error between DS and LS-NUFFT reconstructed images (d) Absolute error between DS and GR reconstructed images.*

The RMSE is a first-order statistic estimator; therefore it provides an indication of the error amplitude. Besides RMSE, also other first order statistic methods have been presented in literature, e.g. the entropy of the image [33].

However, the first-order statistic indices cannot recognize any geometrical structure in error image. The presence of structures in the error image implies that the reconstruction method lost some of the interesting geometric information. Tissue shape preservation and correct depiction of image details are key issues in diagnostic image applications. The presence of structures in the error image can be associated to any value of the RMSE and can only be detected using second-order statistical methods [33, 34]. These methods analyze the relationships between pixels or groups of pixels (usually two), finding correlations in case of structured images. The geometric information loss can be analyzed using the co-occurrence matrix [35], which measures the joint probability of pair of pixels. However the co-occurrence matrix limits the analysis to the relationship of pixels with a fixed geometric position relative to each other. Moreover this method is very sensitive to the noise level in the image. Alternatively, the 2D autocorrelation can provide information about the structures in the image as well [36]. The autocorrelation analyzes the relationships between pixels in any direction and at any distance on the image. Therefore, the autocorrelation provides an indication of how the structures are distributed globally in the image. In fact, in the autocorrelation image it is possible to detect the geometry of the object present in the image.

The reconstruction methods were tested using both a digital phantom and an experimental data set. 3D hyperpolarized ^{13}C *in vivo* data [37] sampled with a spiral trajectory were chosen as exemplary experimental dataset. Chemical Shift Imaging (CSI) of infused hyperpolarized ^{13}C-labelled compounds allows spectroscopy to detect an extensive range of compounds. Tissue perfusion requires the use of ^{13}C-enriched molecules [38] and hyperpolarization [39] to achieve enough sensitivity. The use of hyperpolarized ^{13}C-labeled pyruvate allows a real-time monitor the metabolic conversion of pyruvate to lactate, alanine and bicarbonate in both normal and malignant tissues [40]. Conversion of pyruvate in bicarbonate and lactate is the main factor characterizing aerobic and anaerobic behavior of the heart metabolism [41 - 43]. The [1-

^{13}C]pyruvate tracer fast decay (about 60 sec) requires a very fast acquisition strategy. This is why non-Cartesian trajectories are often used to accelerate the acquisition.

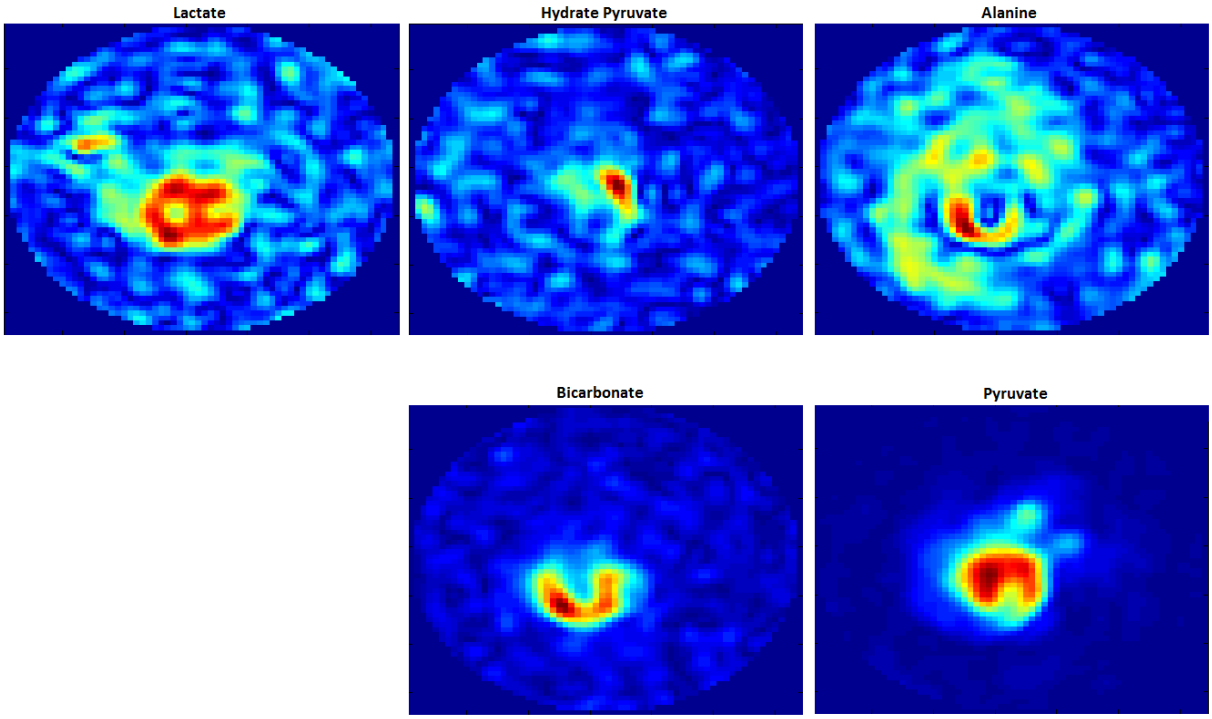

Fig. 4 *Example of typical images of the metabolites obtained with hyperpolarized C13 imaging.*

The performance of LS-NUFFT and GR methods were tested taking DS as reference for the comparison. The geometric information loss was measured analyzing the structures present in the error image, besides calculating the RMSE.

1.3.1. Reconstruction error analysis

The reconstruction error can be analyzed calculating the error image as the difference between the reconstructed image of tested method and of the reference method (i.e. DS). The error image can be modeled as the sum of two error components: structured and random. The amplitude of the overall error can be measured with RMSE. The estimation of the structured component required calculating the 2D autocorrelation of the error image [33, 36]. The presence of

structures in an image can be detected with the width of the central peak of the 2D autocorrelation of the image. A wider peak is associated with more evident structures, hence a heavier loss of geometric information in the error image. Moreover, the geometry of the error image is transferred in the anisotropy of the autocorrelation central peak. In case of an object with a size bigger than the other one, the correlation along the bigger size is kept for longer distance than for the smaller size. The two main widths associated with the autocorrelation central peak were calculated with a fitting described by the following exponential model applied to the normalized error image:

$$g(x,y) = e^{-\left(\frac{x}{\tau_1}+\frac{y}{\tau_2}\right)}. \quad (12)$$

Two decay constants τ_1 and τ_2 were calculated the autocorrelation image, taking the mean decay constant τ as representative of the width central peak. The ratio $R_\tau = \tau_1/\tau_2$ was taken as index of anisotropy of the autocorrelation peak.

The parameter τ is sensitive to the presence of a random component in the image, as any other second-order statistic metric [33]. The presence of noise decreases the correlation of the pixels in the image. Conversely, the entropy or mutual entropy tends to increase with the noise level. Both the noise sensitivity of τ and of the entropy of the co-occurrence matrix was investigated.

In order to obtain an index of structured error relative to the random component level, the method of surrogate data was used [44]. After calculating τ for the image, the pixel location in the image was randomized and a new width of the autocorrelation peak (τ_{rand}) was calculated. The randomized version of the dataset is called 'surrogate' data. The randomization of the pixel locations destroys any structure present in the image, keeping a correlation level dependent on the amplitude of the pixels. The ratio $G = \tau/\tau_{rand}$ was taken as index of loss in geometric information.

1.3.2. Datasets

Experiments were performed on both digital phantom data and real experimental data.

All the implementations of reconstruction methods were done using MATLAB (The Mathworks, Natick, MA, USA) software tool**.** The time elapsed by the reconstruction was reported as well,

using a 1.20 GHz AMD Athlon(tm) X2 Dual Core Processor with 4 Gb of RAM, with Windows 7 Operating System.

MR synthetic data were generated from a 64x64 Shepp-Logan digital phantom considering FOV = 30cm. The spectrum of the image was interpolated on spiral K-space locations.

In order to mimic the spiral sampling used in the real applications, a maximum distance of *1/FOV* was imposed between adjacent turns of the spiral to avoid aliasing, following the Nyquist criterion. A variable density spiral (VDS) was used as filling trajectory for the K-space [45]. VDS are often used in order to spend more time in the center of the k-space, where most of the interesting information lays. The distance between adjacent turns was designed to linearly increase from 0.5/FOV to 1/FOV moving further from the center of the K-space (Fig. 5a). This allows acquiring the center of the K-space more densely and thus gaining better signal-to-noise ratio (SNR).

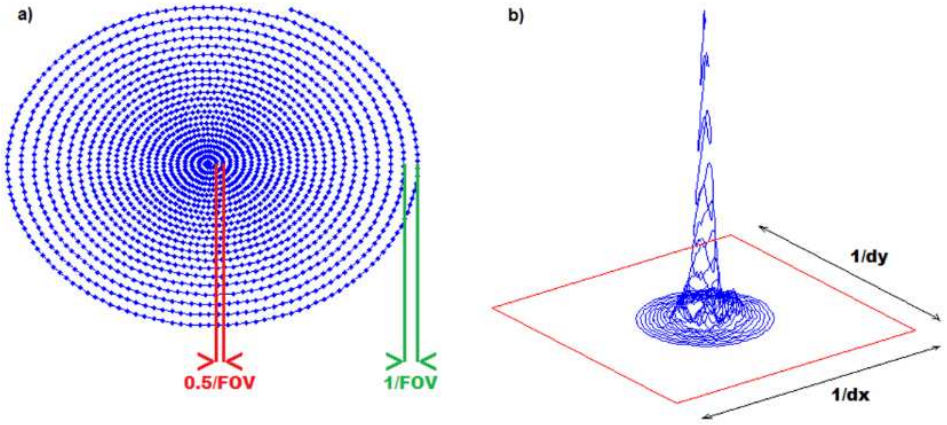

Fig. 5 *a) VDS used for simulation and experiments. Distance between adjacent turns linearly increases moving toward periphery of K-space. b) Modulus of K-space acquired data plotted onto the sampling trajectory. The width of the trajectory does not cover the inverse of spatial resolution. This implies zero padding and thus blurring on the reconstructed image.*

The point spread function (PSF) [46] was calculated to characterize the behavior of the reconstruction methods.

Regarding the experimental dataset, metabolic information covering the heart was obtained using a 3D IDEAL spiral CSI with FOV of 30cm and slab thickness of 10cm. A 3D dataset was acquired using a pulse-and-acquire sequence with 2D spiral readout and Cartesian phase

encoding (PE) along the slice-encode direction (*z*). Sampling along *z* direction was Cartesian. Thus slices could directly be obtained performing a 1D-FFT on *z* direction. The following acquisition parameters were used: 14 PE along *z*, 11 echoes per PE at different echo time (TE), constant TE increment = 0.9 ms, 1824 samples per echo, flip angle = 7°, receiving bandwidth = ±62.5 kHz. The animal experiment was performed on a healthy male mini-pig using a 3T GE HDx Excite MR scanner (GE Healthcare, Waukesha, WI, USA) with a ^{13}C quadrature birdcage coil. [1-^{13}C]pyruvate hyperpolarization was obtained using a HyperSense DNP polarizer (Oxford Instruments, Oxford, UK) with subsequent dissolution.

Before reconstruction, experimental raw data were processed with the IDEAL method as described in [47, 48]. Fig. 6 explains the process performed on each dataset of different pigs. Data were firstly low-pass-filtered to improve SNR and reduce ringing artifact. Secondly, resonance frequencies of the metabolites were identified with a matching pursuit algorithm. Afterwards the IDEAL method was applied using the pseudo-inverse matrix.

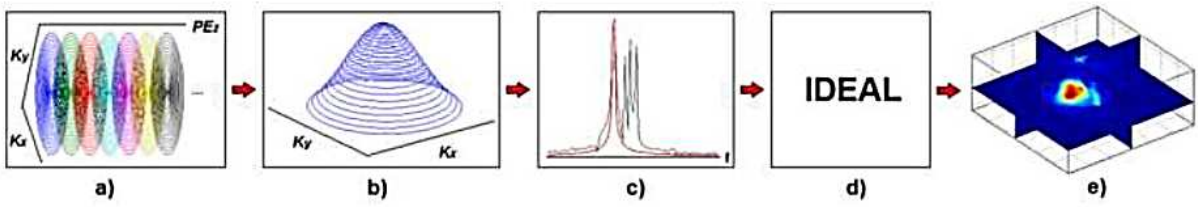

Fig. 6 *Diagram of the processing procedure performed on experimental data. a) Acquisition. A spiral trajectory was used for each Phase Encode along the third direction. b) Filtering. For each single slice, data were Low-Pass-filtered to reduce noise level of high frequencies and ringing artifact. c) Matching Pursuit. Accurate resonance frequencies were detected for each metabolite. d) IDEAL. A pseudo-inverse matrix allowed us to obtain spectrum data. e) Reconstruction. Space 3D volumes were reconstructed and visualized.*

Finally the reconstruction methods were applied separately for the 2D images of each slice. The acquired VDS trajectory was similar to the one used for simulations. A zero padding interpolation (Fig. 5b) was applied to obtain 64x64x64 images, but the actual resolution of the image is bigger than the pixel size. The actual resolution is also worsened by the application of

the Gaussian low-pass filter to reduce the truncation artifact and remove part of the high-frequency noise. The actual in-plane resolution of the dataset was about 12mm.

1.3.3. Results

The performance of τ was analyzed simulating the progressive presence of structures and random error (Fig. 7a). A 128x128 Shepp-Logan phantom was used for the simulation and the results were averaged over 30 repetitions. The parameter τ is sensitive to different levels of structures present in the image. When more structures are present, the width of the autocorrelation widens. However, as the level of simulated random error increases, τ loses sensibility to the image structures. Fig. 7b shows the behavior of parameter *G* obtained in the same simulation. As the intensity of the random error increases, *G* approaches 1. Conversely, when detectable structures are present in the error image, *G* increases. G can be considered equal to 1 for error levels higher than about 3 times the maximum signal of the structured error.

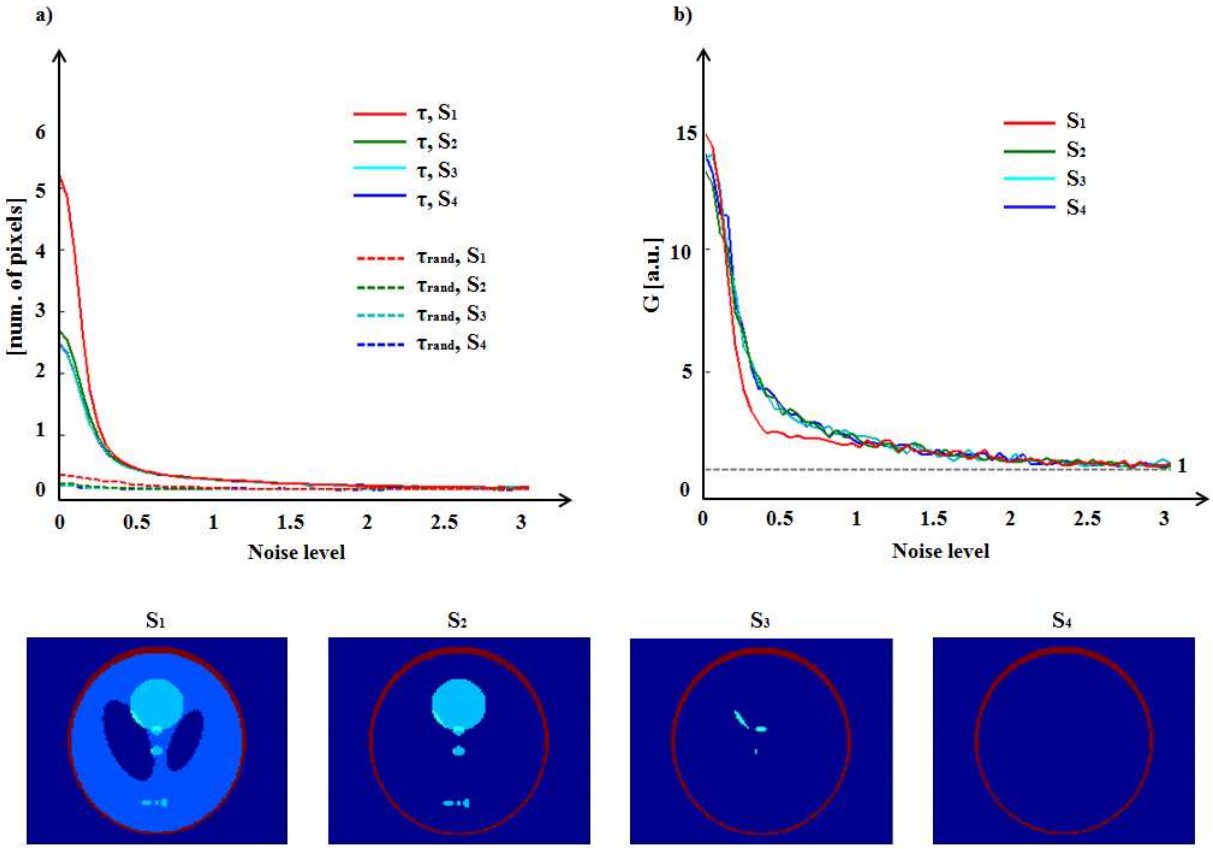

Fig. 7 *Analysis of the structure detection performance in presence of noise. The noise level is the ratio between the amplitude of the noise variance and the structure maximum signal. The bottom row depicts the decreasing levels of structure (S_1, S_2, S_3, S_4) used in the analysis. The behaviour of τ and τ_{rand} are shown in (a) as the noise level increases and for different level structures. The behaviour of the relative index G is shown in (b).*

The same analysis was done also for another second-order statistic index, i.e. the entropy of the co-occurrence matrix. This index appeared to be very sensitive to the level of random error present in the image. Even a small amount of noise was able to blind the metric with very little difference among different level of structured error. The results shown in Fig. 8 suggest that the width of the autocorrelation matrix is a better index to determine the geometric information loss.

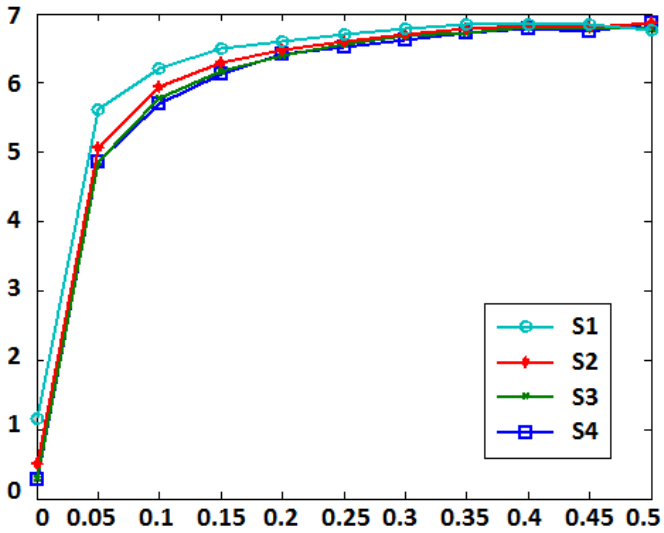

Fig. 8 *Analysis of the entropy of the co-occurrence matrix dependency over the structured and random errors. The metric appear to be too sensitive to the level of random error in the image.*

The PSF was calculated for both reconstruction methods. The PSF characterizes how the method behaves with a general reconstructed image. The error image and the autocorrelation were calculated for the PSF (Fig. 9). The autocorrelation of the PSF decreased more slowly than in the case of LS-NUFFT than GR. From the PSF, the error associated with LS-NUFFT appears more correlated than the error associated with GR.

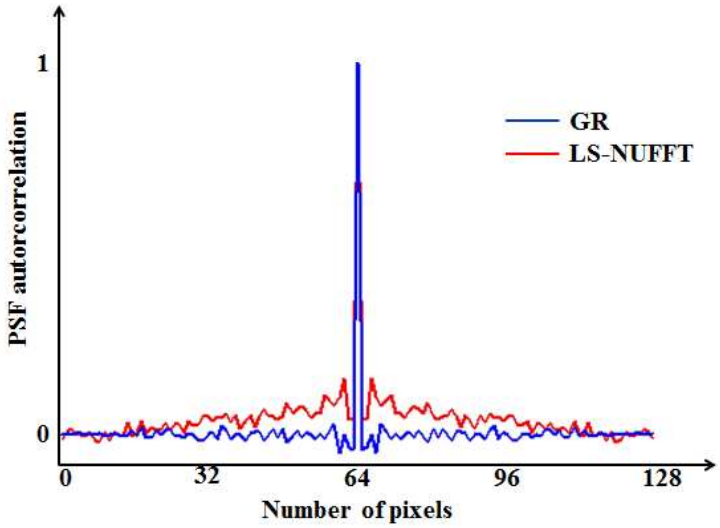

Fig. 9 *Middle line of the normalized 2D autocorrelation for the PSF for both reconstruction methods. The curve for LS-NUFFT decreases more slowly than GR. Therefore, the PSF analysis shows that the error image of the LS-NUFFT is more structured than GR.*

For the digital phantom experiments on the reconstruction methods, GR obtained τ = 12.9mm, G =9.3, R_τ = 1.6 and RMSE = $5.1 \cdot 10^{-4}$, whereas LS-NUFFT obtained τ = 52.6mm, G = 35.0, R_τ = 1.4 and RMSE = $9.6 \cdot 10^{-5}$. Therefore, LS-NUFFT allows the reconstruction to have an improvement of 5.3 times in the RMSE, as previously shown in literature [23]. However, in the case of LS-NUFFT the structured error is 35 times more relevant than the random error, whereas only 9.3 times in the case of GR. Fig. 10 shows the error images and autocorrelations for both methods. The shape of the autocorrelation follows the one of the reconstructed object (Fig. 10d, Fig. 10e). The parameter R_τ keeps track of the image anisotropy. In the case of an object with one dimension longer than the other one, the correlation will be preserved for longer distance than for the shorter dimension and R_τ will be bigger than one.

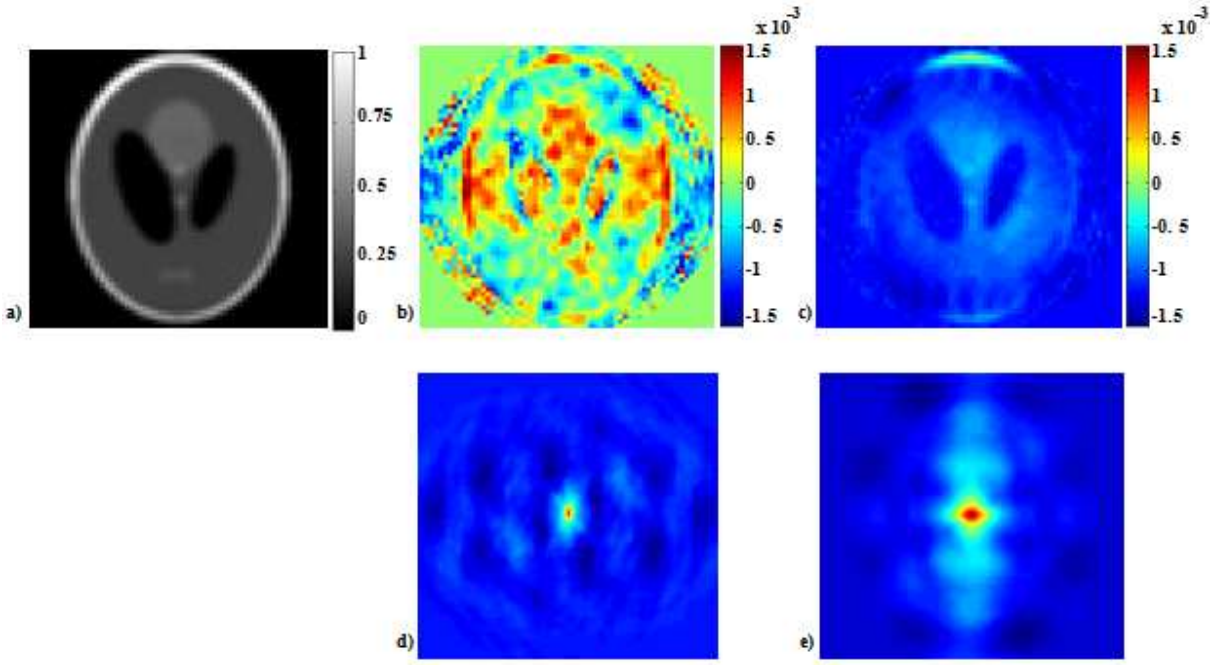

Fig. 10 *Simulation results. a) Reconstructed image with DS method. The image has been normalized by its maximum value. b, c) Error image of GR method (b) and LS-NUFFT (c) using DS as reference. FOV is circular for both images. d, e) Image of the 2D autocorrelation for the error image in GR (d) and LS-NUFFT (e) method.*

The values of τ, G, R_τ and RMSE were evaluated for experimental data as well (Tab. 1). Fig. 11 shows the exemplary result images for pyruvate on central slice.

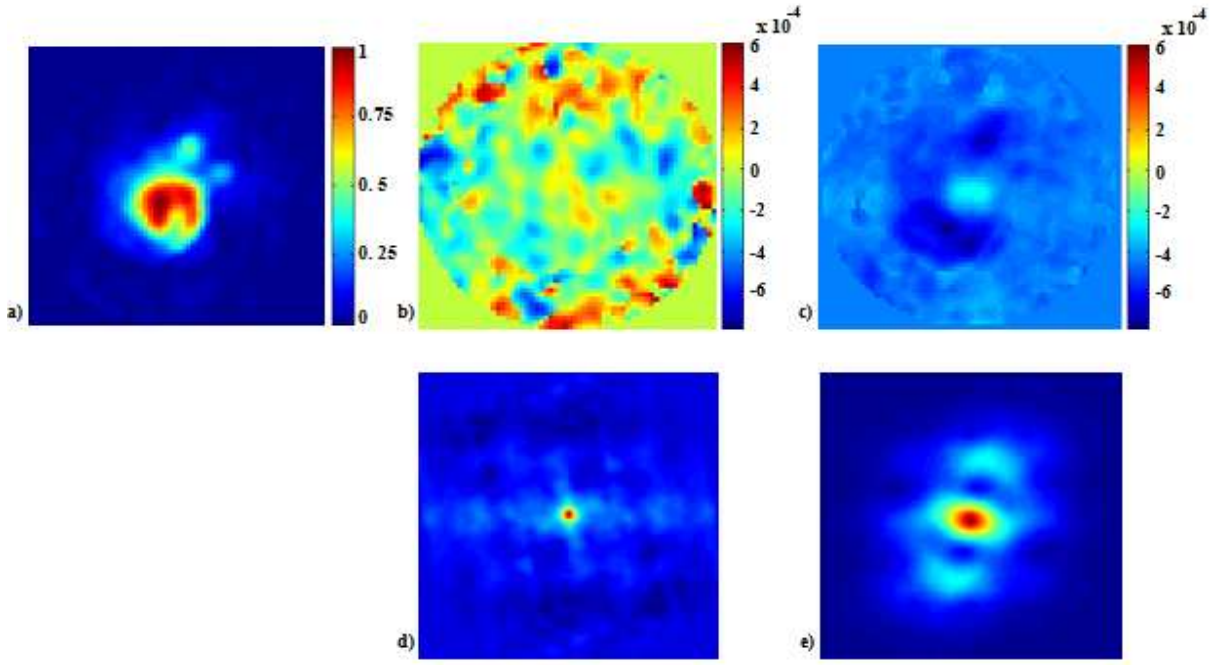

Fig. 11 *Experimental results shown for Pyruvate on central slice. a) Modulus of reconstructed image using DS. Image has been normalized by its maximum value. b, c) error image of GR method (b) and LS-NUFFT (c) using DS as reference. FOV is circular for both images. d, e) Image of the 2D autocorrelation for the error image in GR (d) and LS-NUFFT (e) method.*

GR	Lactate	hydrate pyruvate	alanine	bicarbonate	Pyruvate
RMSEx10^{-5}	3.4±0.4	3.4±0.4	3.9±0.6	3.6±0.6	12.0±5.5
τ [mm]	9.3±0.6	12.4±1.7	16.6±2.5	10.9±1.1	13.3±1.6
R_τ	1.14±0.05	1.13±0.05	1.20±0.07	1.08±0.05	1.16±0.06
G	6.5±0.5	7.9±0.8	8.4±0.8	7.0±0.6	11.8±1.8

LS-NUFFT	lactate	hydrate pyruvate	alanine	bicarbonate	Pyruvate
RMSEx10^{-5}	0.89±0.12	0.89±0.14	1.31±0.34	0.95±0.20	2.76±1.17
τ [mm]	53.3±3.1	55.1±1.9	57.8±1.9	55.3±2.9	44.1±8.5
R_τ	1.47±0.08	1.50±0.03	1.57±0.02	1.54±0.04	1.44±0.12
G	13.6±0.5	13.0±0.8	10.8±1.8	13.8±0.9	17.3±0.9

Tab. 1 *Results obtained with the experimental dataset for each metabolite (lactate, hydrate pyruvate, alanine, bicarbonate and pyruvate). The values showed are averaged over the 64 slices of the reconstructed dataset.*

The reconstruction time of the methods was reported as well. GR and LS-NUFFT obtained about the same reconstruction time of 10±1ms, because they are both gridding methods, based on the use of FFT. The reconstruction time was 690±1ms for the DS method. GR and LS-NUFFT appear about two orders of magnitude faster than the DS method due to the different computational complexity.

The DS method and the gridding methods are different in terms of reconstruction accuracy. The signal-to-noise ratio (SNR) in the reconstructed image is also dependent on the reconstruction method that is used. Comparing the GR method with the DS, for example, it is possible to observe that the DS method has a lower associated SNR then GR [49]. This is shown in the following figure, where the relative SNR ($(SNR_{DS}-SNR_{GR})/SNR_{DS}$) was calculated for all the slices and all metabolites of the experimental dataset.

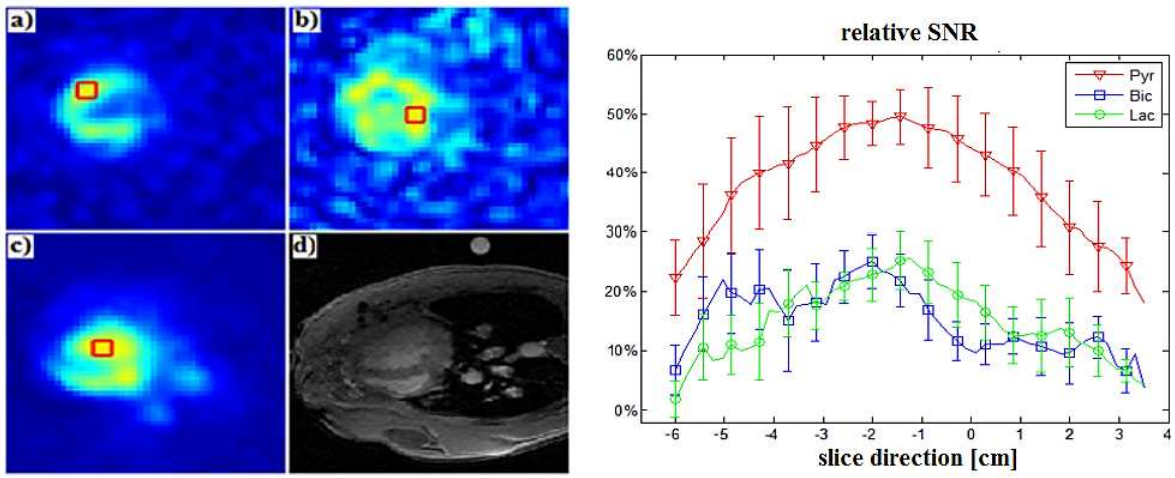

Fig. 12 *Right images of the bicarbonate (a), lactate (b) and pyruvate (c) on the central slice with associated anatomical image (d). The region-of-interest (ROI) for the calculation of the SNR is depicted as red square. The relative SNR over the slices for the three metabolites is depicted on the right.*

This result justifies the fact that the DS method is typically taken as reference for the reconstruction methods. However DS is much slower than the gridding methods, like GR or LS-NUFFT, and therefore not often used in the practice. This side result points out that the error present in the reconstructed image is also generated by the noise superposed to the input data. Moreover the noise transmitted to the reconstructed image depending also on the reconstruction method that is used.

1.3.4. Discussion on the geometric information loss

The LS-NUFFT and GR methods were compared using the DS method as reference. As shown in previous works in literature [23], LS_NUFFT obtained a lower RMSE than GR for both simulated and experimental datasets. Here the analysis was extended to the geometrical information loss of the reconstruction method. An index of geometric information loss (G) was presented and calculated using the 2D autocorrelation of the error images.

The use of the 2D autocorrelation to quantify the presence of structures in the image was shown to be effective. The simulation performed with different levels of structured and random noise, shows the limitation associated with the use of the width of the autocorrelation peak directly. The parameter τ is an absolute measure sensitive to both structured and random errors. Therefore the observation of τ alone does not allow the distinction from the two types of error. The index G was introduced in order to have relative index for geometrical loss, valid for any level of structure in the image. The index G measures how much the structured errors are relevant compared to the random errors. The parameter G was shown to have a reduced dependency on structures in the image, comparing to τ. In fact, especially in the case of several structures, the surrogate method does not cause the total loss of correlation in the image even randomizing the pixel locations. The residual correlation present in the surrogate data is associated to the amplitudes of the pixels in the image. The following figure depicts this concept. For an image with all pixels equal to 1, the associated autocorrelation has a central line which is shaped as a triangle. In case of random noise, the autocorrelation is a Dirac delta (i.e. just a central peak). For all the surrogate images the amplitude of the pixels in the image creates an autocorrelation that is something in between these two extreme examples, i.e. a triangle shape with a higher central

peak. The triangle shape is wider in case of more pixels with coherent amplitude, therefore in case of more structures in the image.

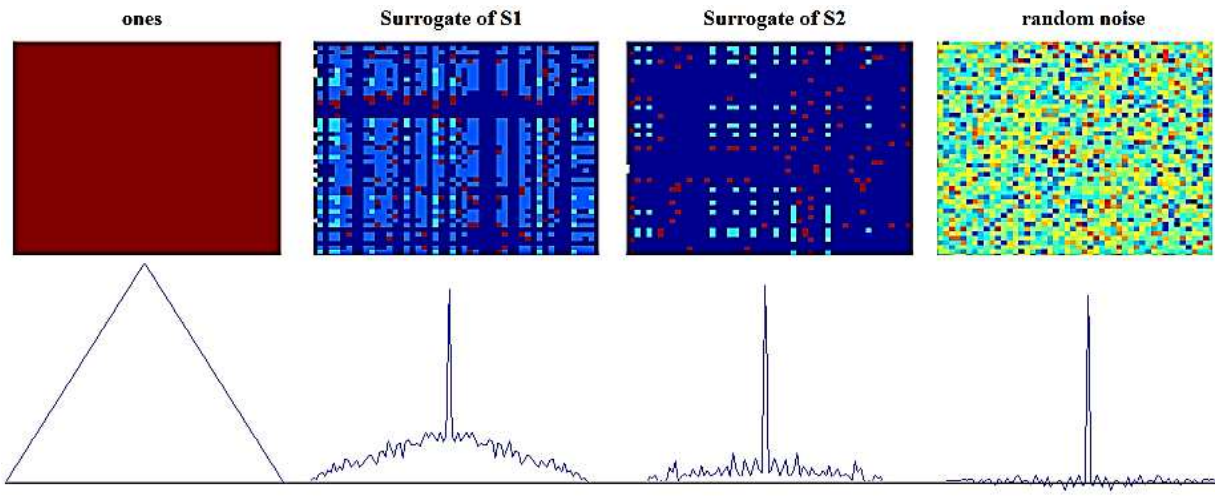

Fig. 13 *From left to right on the top row: image of ones, surrogate image of S1 level of structures, surrogate image of S2 level of structures, random Gaussian noise. S1 and S2 are referred to Fig. 7. Bottom row: central line of the autocorrelation associated to the images on the top row.*

For these reasons, a memory of the behavior of τ can still be found in $\tau_{rand,}$ thus making G less dependent on the structure level.

The estimation of geometric information loss as performance index represents an important improvement in evaluation of reconstruction methods. Previous studies only focused on RMSE of reconstruction which is only able to give information about the first-order statistics of the reconstruction error. The presence of structures in the error image can be detected only by using a second-order statistic index, like the autocorrelation. The entropy of the co-occurrence matrix was shown to be too sensitive to random errors for these applications. Structures may be present in the error image also in case of low RMSE. Therefore a performance analysis limited to the RMSE does not benefit from all the information available in the error image. Despite the lower RMSE, LS-NUFFT showed an error image more structured than GR. A comparison limited to the RMSE would not have been able to recognize that also LS-NUFFT loses relevant information in the reconstruction process.

For both the simulated and experimental datasets, LS-NUFFT obtained a *G* value higher than GR. However, the relative difference between the *G* values of the two reconstruction methods is higher in the case of the simulated data. This is due to the different level of structure and acquisition noise in the analyzed images. In fact, the acquisition noise increases the random error component, hence decreasing the value of *G*. The level of noise present in the reconstructed image also depends on the reconstruction method as suggested in [49].

The shape and the size of the interpolation kernel for gridding methods is a key issue in determining the accuracy of the reconstruction [20 - 22]. For example, the characteristics of the gridding kernel can change the amplitude of the reconstruction error or the shading on the reconstructed image. For LS-NUFFT the choice of the gridding kernel is guided by the pseudo-inverse matrix, hence minimizing the approximation error. For LS-NUFFT the size of the kernel can cause relevant reconstruction error related to the matrix pseudo-inverse calculation [24]. Therefore the kernel size was carefully chosen in order to make the two reconstruction methods comparable and avoid the need for a regularization method for the pseudo-inverse calculation.

In this study the same weighting function was used for the data to compare the reconstructions methods. The DCF was evaluated using the Voronoi diagram for all three methods considered. DCF has a relevant influence on the reconstructed image, as proved by the extensive studies on its shape [12, 18]. LS-NUFFT differs from GR only in operations coming after data weighting. The use of different DCFs would not allow distinguishing the differences in reconstructed images due to DCF, and the ones due to the interpolator. In this work the effect of the DCF on the reconstructed image was not considered. The study of the effect of DCF over the loss in geometric information could be an interesting development of the present work.

The use of the 2D autocorrelation function could also be useful in parallel imaging applications [5, 6]. Parallel imaging techniques commonly suffer from coherent aliasing artifacts, which could easily be detected by the 2D autocorrelation function. The presence of an image ghost would be detected with a secondary peak placed in the same spatial location of the ghost (Fig. 14). Ghosts might also appear in many other different applications, like the typical N/2 ghosts of the EPI sequence [1]. For this application the amplitude of the autocorrelation peak, rather than the width, could be useful to quantify the intensity of the ghost.

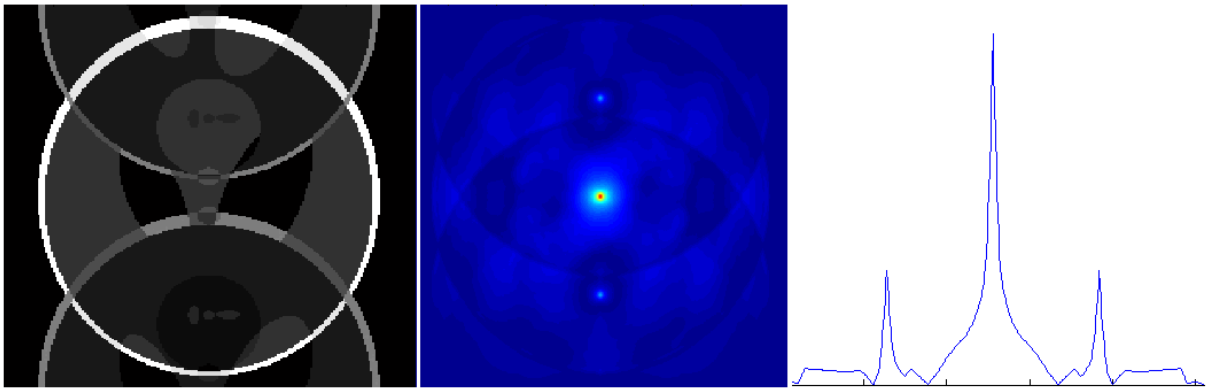

Fig. 14 *Example of image with N/2 ghosting (left) with associated 2D autocorrelation (middle) and autocorrelation vertical profile (right).*

1.3.5. Conclusions on the geometric information loss

The LS-NUFFT and the GR reconstruction methods were compared testing their performances on both simulations and hyperpolarized ^{13}C 3D CSI *in vivo* data. LS-NUFFT obtained smaller RMSE than GR, but the error image of LS-NUFFT appeared more structured than GR. These results strongly suggest that both reconstruction error and geometrical loss of information indices should be adopted for a complete evaluation of reconstruction methods. Even though LS-NUFFT shows better reconstruction accuracy, it is relevant to be aware that the reconstruction process lost interesting information and not only noise.

1.4. REGULARIZATION METHODS APPLIED TO LS-NUFFT

As mentioned above, LS-NUFFT is a gridding method that uses a pseudo-inverse calculation in order to obtain the interpolation kernel. Generally, when the width of the interpolator grows, the performance of reconstruction is improves because more samples are used to evaluate the sample on the Cartesian grid. However, for LS-NUFFT the increase of the interpolator width might make the inversion problem ill-conditioned [22].

An ill-conditioned problem is associated to a matrix which is close to be singular. For a singular matrix, the reachable subspace is squeezed on a dimension lower than the smaller dimension of the matrix (i.e. the rank is not maximum). In the case of ill-conditioned problems, even though the rank is maximum, the subspace spanned by the matrix has some dimensions on which the output vectors will not have high components. The singular-value-decomposition (SVD) analysis clarifies this concept immediately. Taken a full-rank matrix, the problem is well-posed in case the singular values are all significant and comparable to one another. In case some singular values are significantly lower than the other ones, the associated auto-vector direction will have small projections of the data on itself. The following image shows an example of the span of a 3x3 matrix with 3, 2 or only 1 significant singular value.

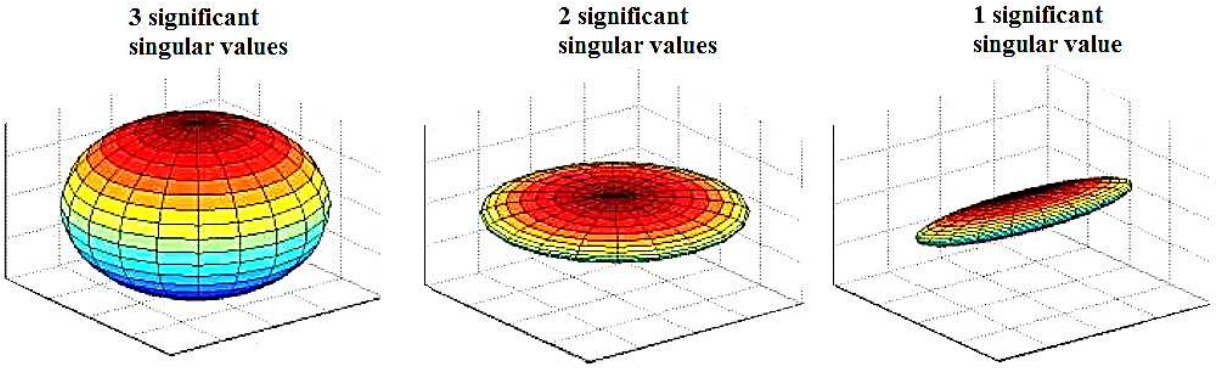

Fig. 15 *Example of the span of a 3x3 matrix with full rank and 3, 2 and only 1 significant singular value.*

When the problem becomes ill-conditioned, reconstruction is not acceptable because even a minimal input error or noise contribute is dramatically amplified in the reconstructed image. A regularization technique can be used in order to be able to perform a pseudo-inversion on an ill-

conditioned matrix. The term 'regularization' generally refers to any technique including some *a priori* information in the analysis. This additional information is capable of reducing the conditioning number of the problem and allows calculating the solution with acceptable accuracy.

Three different regularization methods were applied to LS-NUFFT in order to achieve an acceptable reconstructed image despite ill-conditioning. An analysis was performed in order to determine which one of the regularization methods is more suitable for LS-NUFFT, performing tests on both simulated and experimental data. The processing time required to calculate the interpolator was also considered in the analysis.

1.4.1. Regularization methods applied to LS-NUFFT

When the interpolator width is too big, the inversion problem in Eq. 11 becomes ill conditioned [22]. In this case a regularization technique can be used to achieve accurate reconstruction. Three regularization techniques were tested on LS-NUFFT.

The Truncated Singular Value Decomposition (TSVD) [50] was used in the first place. TSVD uses the SVD decomposition to obtain a pseudoinverse matrix. A threshold (*th*) on singular values is used to regularize the problem. If the SVD of A is $U\Sigma V^T$, the expression of TSVD pseudoinverse is the following:

$$A_{TSVD}^{\dagger} = V\Sigma^{\dagger}U^T \tag{13}$$

where $\Sigma^{\dagger}$ is a diagonal matrix. On the diagonal of $\Sigma^{\dagger}$ there are the inverses of singular values bigger than the threshold.

The Tikhonov Regularization (TR) was used as well [50]. TR can be formulated as a multiple objective minimization. The following objective function is to be minimized:

$$S_{TR} = \left\| A \cdot \rho_k(\omega_h) - v(\omega_h) \right\|_2^2 + \lambda_{L2} \left\| \rho_k(\omega_h) \right\|_2^2 \tag{14}$$

TR minimizes the error and keeps the Euclidean norm of the interpolator low at the same time. It has been shown that TR is very similar to TSVD [50]. TR does not use a threshold on singular values, but it filters them. Filtering shape depends on the λ_{L2} parameter.

Finally the L_1 regularization (L1R) [51, 52] was also used. L1R can also be expressed as a multiple minimization. L1R minimizes the following objective function:

$$S_{L1R} = \left\| A \cdot \rho_k(\omega_h) - v(\omega_h) \right\|_2^2 + \lambda_{L1} \left\| \rho_k(\omega_h) \right\|_1 \quad (15)$$

L1R minimizes both the square of Euclidean norm of approximation error and the L_1 norm of the interpolator. Minimization of $\left\| \rho_k(\omega_h) \right\|_1$ is intended to define an interpolator with as many zero coefficients as possible. We refer to this kind of interpolator as sparse. The sparsity in the interpolator is a reasonable target, because interpolated samples are likely to depend more strongly on close locations than on far ones.

We will refer to LS-NUFFT without regularization as NR, which stands for 'No Regularization'.

In general all these different regularization methods can be considered as belonging to the same big family of regularization methods formulated by Tikhonov in his theory. However, a change in the formulation of the additional *a priori* information included with the regularization term can change significantly the solution of the problem.

1.4.2. Simulation and experimental setup

Both simulated and experimental datasets were used to evaluate the performance of the reconstruction method using regularization techniques. The Shepp-Logan (SL) phantom was used as simulated dataset. The spectrum of a modified SL phantom was calculated on a spiral trajectory.

The experimental data were acquired from a human abdomen. We used a 1.5T Signa Excite MR scanner (GE Healthcare, Waukesha, WI, USA). An eight-element cardiac phased-array receiver surface coil was used for signal reception. A spiral scanning sequence was used with the following scan parameters: FA=25°, TE=16ms, single interleaf, 5860 samples, FOV=30cm, slice thickness = 5mm, 128×128 images.

1.4.3. Implementation

The specification of the implementation are similar to the one stated above for the evaluation of geometric information loss. Also for the study on regularization a variable-density-spiral (VSD)

was used and the DS method was taken as reference to evaluate the performance of the regularization method on LS-NUFFT.

In this case the density compensation function (DCF) for both DS and LS-NUFFT was calculated using the Jacobian matrix, as suggested by Meyer et al. [53]:

$$DCF\left(\vec{k}(t)\right)^{-1} = \left|\vec{k}'(t)\right| \cdot \left|\sin\left(\arg\left(\vec{k}'(t)\right) - \arg\left(\vec{k}(t)\right)\right)\right| \tag{16}$$

$\vec{k}(t)$ is the k-space location acquired along the sampling trajectory at time *t* and $\vec{k}'(t) = \frac{d\vec{k}(t)}{dt}$.

The LS-NUFFT was implemented similarly as described above, choosing a Kaiser-Bessel shape as scaling function, as suggested by Fessler and Sutton [22]. The actual implementation of LS-NUFFT was done following the formulation by Fessler and Sutton [22].

Reconstruction performance was measured only by the calculation of the root mean square of reconstruction error (*RMSE*). The *RMSE(q)* was calculated for increasing values of *q*. First the *RMSE(q)* was calculated for LS-NUFFT without regularization to show when regularization is actually needed. Then *RMSE(q)* was evaluated for each of the three regularization methods. We considered integer values of *q* up to the size of reconstructed image *M*. This range for *q* keeps matrix *A* skinny or square.

LS-NUFFT requires calculating a pseudoinverse and its regularization parameter for all acquired frequencies and for all tested values of *q*. For TSVD, the regularization parameter is the number of preserved singular values of matrix *A*. The number of preserved singular values was calculated using Generalized Cross Validation (GCV) [55]. GCV chooses the regularization parameter so that missing data values can be predicted well by regularized pseudoinverse. The chosen regularization parameter is the one that minimizes the following function:

$$G(\lambda) = \frac{\left\| A \cdot \rho_k(\omega_h) - v(\omega_h) \right\|_2^2}{tr\left(I - AA^{\#}\right)} \tag{17}$$

λ is the regularization parameter, $A^{\#}$ is the regularized matrix, and *tr(.)* is the trace operator. $\rho_\lambda(\omega_h)$ is the interpolator found using λ as regularization parameter.

TR was implemented using the following expression:

$$\rho_{TR} = \left(A^H A + \lambda_{L2} I \right)^{-1} A^H v(\omega_h) \tag{18}$$

ρ_{TR} is the interpolator found using TR. GCV was used to determine the TR regularization parameter (λ_{L2}) as well.

L1R was implemented using Convex Optimization [51]. Duality allows us to handle the L_1 non-linear estimator. Convex Optimization was implemented using the Newton's Interior Point method [51] to iteratively search for the solution of the minimization problem. The regularization parameter (λ_{L1}) was defined as the one that minimizes the RMSE of the reconstructed image, keeping calculation time for the interpolator as low as possible.

The parameter sensitivity was tested for each regularization method, calculating the reconstruction error using different values of the regularization parameters.

The processing time was evaluated in order to calculate the interpolator by averaging the processing time over ten experiments with the computer configuration previously described. The reported processing time is not the one needed for the reconstruction, but it is the time needed to calculate the interpolator. Once the interpolator has been calculated, it can be stored and the reconstruction takes place with $O(M^2 log(M^2)+N_s q^2)$ computational complexity. It is worth noting that the number of multiplications needed for the 2D interpolation is $N_s \cdot q^2$.

1.4.4. Results

The 2D LS-NUFFT of SL phantom and experimental data were computed using 128×128 as the size of the reconstructed image. Fig. 16 shows the *G* function of Eq. 17 to determine the number of singular values to be preserved for TSVD. For every value of q we chose the value of regularization parameter that minimizes the *G* function. For $q \leq 20$ all singular values were preserved. For $q > 20$ the smallest preserved singular value was always about 10^{-6}. For TR, GCV let us obtain the values for λ_{L2} as function of q. The λ_{L2} was above 10^{-8} for $q > 14$, whereas it drops to about 10^{-12} for $q \leq 14$.

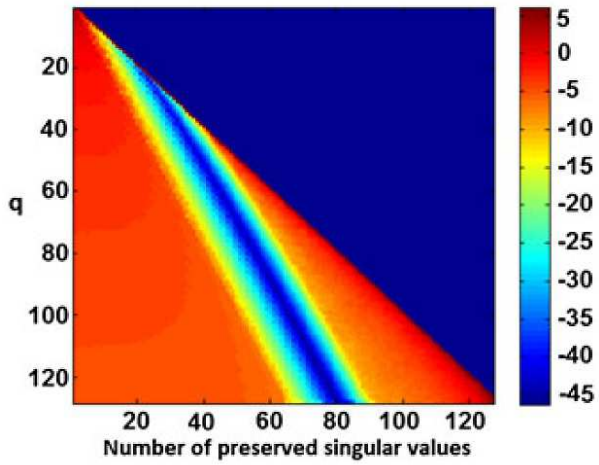

Fig. 16 *: G function in GCV for choosing the number of preserved singular values in TSVD. q is on the vertical axis and the number of preserved singular values is on the horizontal axis. The color scale is logarithmic. The range of q goes from 2 to 128. The interesting values of G are below the main diagonal. The minimum value of G determines where to put the threshold for truncating the singular values.*

A simulation was done in order to measure the reconstruction error for each regularization method in dependence of different regularization parameters (Fig. 17). For the TSVD and TR methods, the simulation confirmed the optimal values previously found (Fig. 17a and Fig. 17b).
For L1R, we experimentally found that the error curve E_{rms} becomes stable for λ_{L1} lower than 10^{-7} for $q > 14$, whereas the optimal λ_{L1} was zero for $q \leq 14$ (Fig. 17c). The optimal regularization parameter was the same using different values of frequency for all techniques.
Sensitivity of the reconstruction error with respect to parameter values can be observed in Fig. 17. For TSVD, the error decreased with the value of threshold *th* on singular values until the optimal value was reached. A further decrease of *th* is associated with an increase in the error. The TR method shows the same trend with a higher sensitivity. L1R also showed a decrease in the error moving towards the optimal value. The error became stable for λ_{L1} values lower than the chosen one.

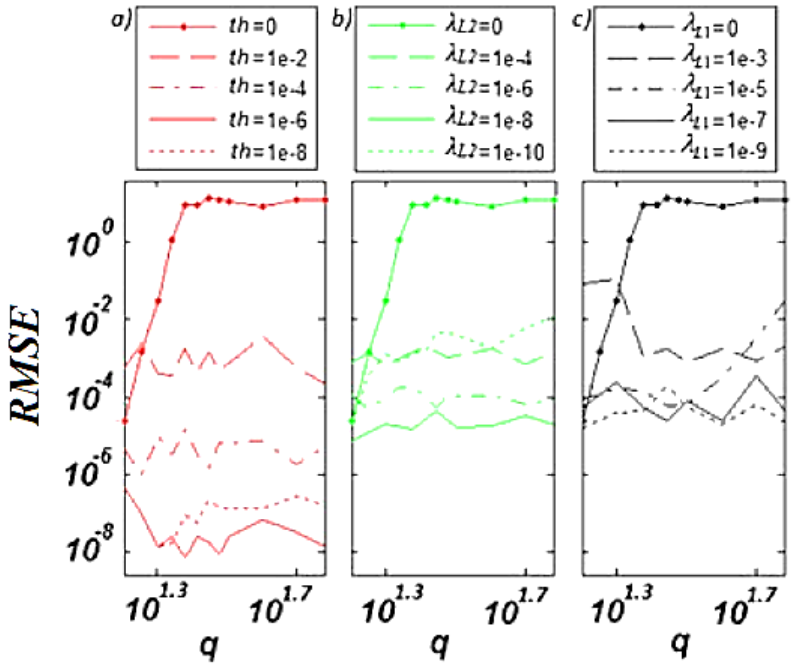

Fig. 17 *Parameter sensitivity for regularization methods. We used values of the regularization parameter different from the optimal one we found. a) TSVD with threshold th on singular values as regularization parameter, b) TR with λ_{L2} as regularization parameter, c) L1R with λ_{L1} as regularization parameter.*

Fig. 18 shows the value of *RMSE(q)* with and without using regularization in the SL phantom using 64×64 and 128×128 as size of reconstructed image. For 64×64 the curve was evaluated only up to *q=64* to keep *A* skinny or square. As shown in Fig. 18, *RMSE(q)* is largely independent of the reconstructed image size. This behaviour was verified on other sizes of the reconstructed image.

Considering LS-NUFFT without regularization, for low *q* a wider interpolator is associated with a better reconstruction. This is due to the higher number of samples used by a wider interpolator, so a higher *q* allows us to achieve more accuracy in the interpolation. *RMSE(q)* has a minimum at *q = 14*. For *q > 14*, *RMSE(q)* starts to increase, so regularization is needed. *RMSE(q)* is shown also using the regularization methods. For $q \leq 14$ the reconstruction error associated with the regularization methods is exactly the same as the NR method. TSVD obtained the smallest minimum value of *RMSE(q)* among the three methods, while L1R obtained the highest. TR

showed an almost stable error, intermediate between the error of TSVD and L1R. The results found for raw data are consistent with results for simulated data (Fig. 19).

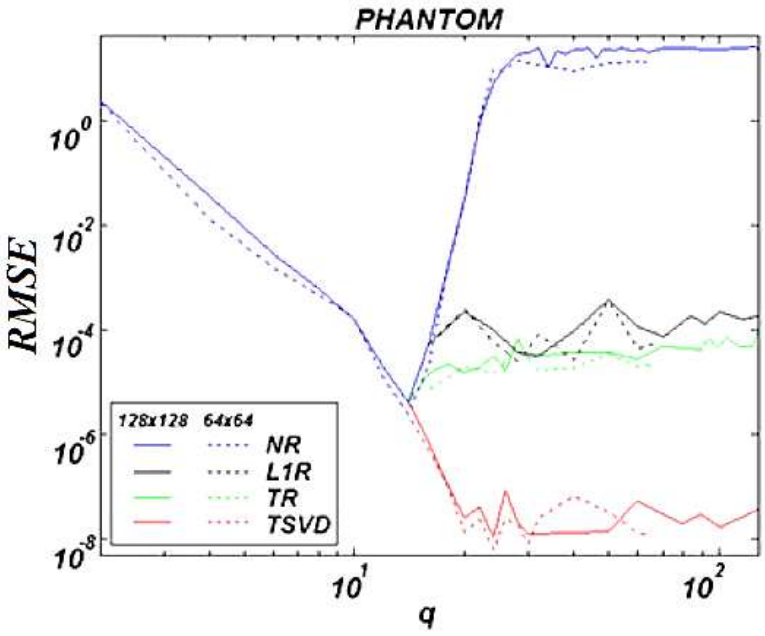

Fig. 18 *RMSE(q) for LS_NUFFT with and without regularization using simulated data. Logarithmic scale is used for both vertical and horizontal axis. Shapes are plotted for 128×128 (solid line) and 64×64 (dotted line) as size of reconstructed image. RMSE(q) is also plotted for all three regularization methods using* $q \geq 14$.

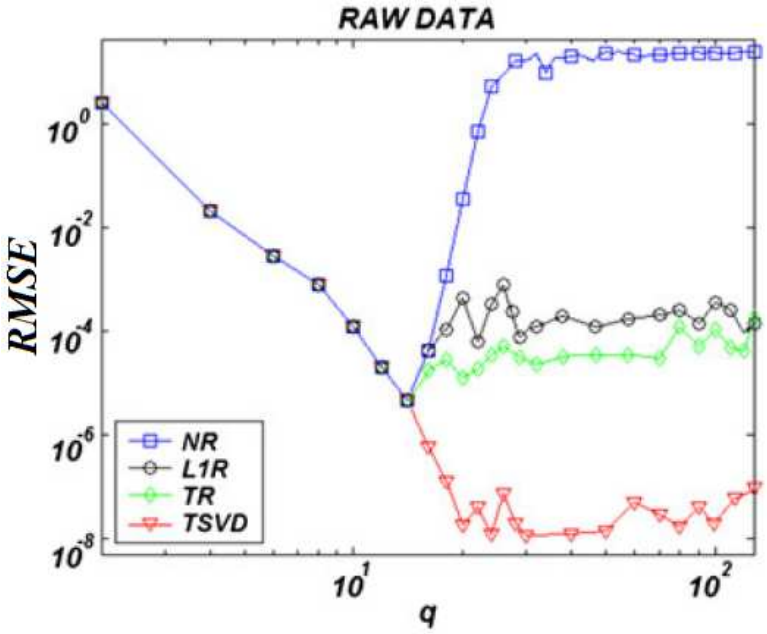

Fig. 19 *RMSE(q) for LS_NUFFT with and without regularization using raw data. Logarithmic scale is used for both vertical and horizontal axis. RMSE(q) is plotted for all three regularization methods using* $q \geq 14$.

The following figures show the difference images obtained using the calculated interpolators. Fig. 20 is referring to simulated data and Fig. 21 refers to raw data. For each regularization method we showed only the difference image associated with the interpolator that obtains the minimum *RMSE(q)*.

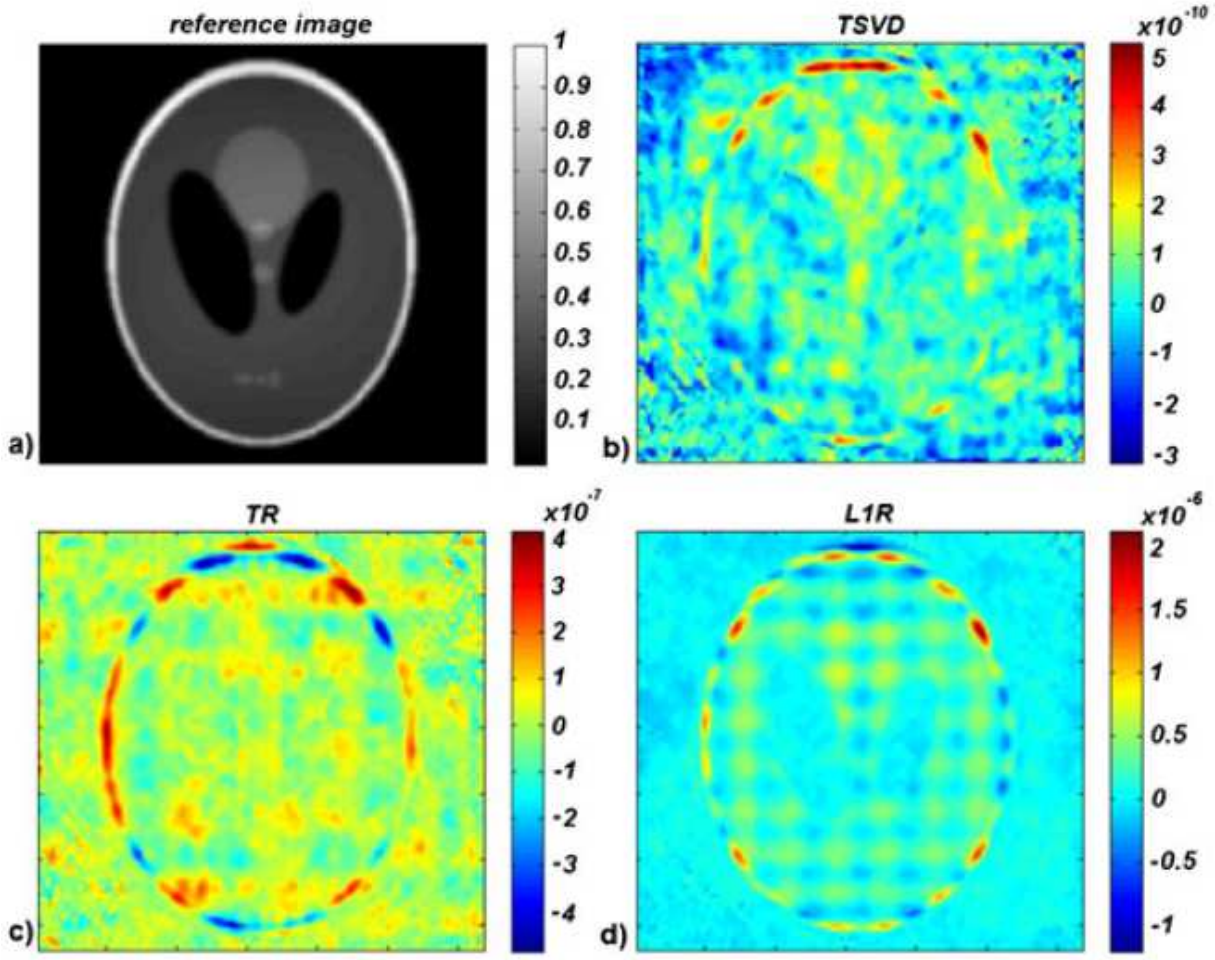

Fig. 20 *Difference image for simulated data from SL phantom. a) Reference reconstructed image (128×128) obtained using DS. b) Difference image for the best interpolator obtained with TSVD (q=24). c) Difference image for the best interpolator obtained with TR (q=14). d) Difference image for the best interpolator obtained with L1R (q=30).*

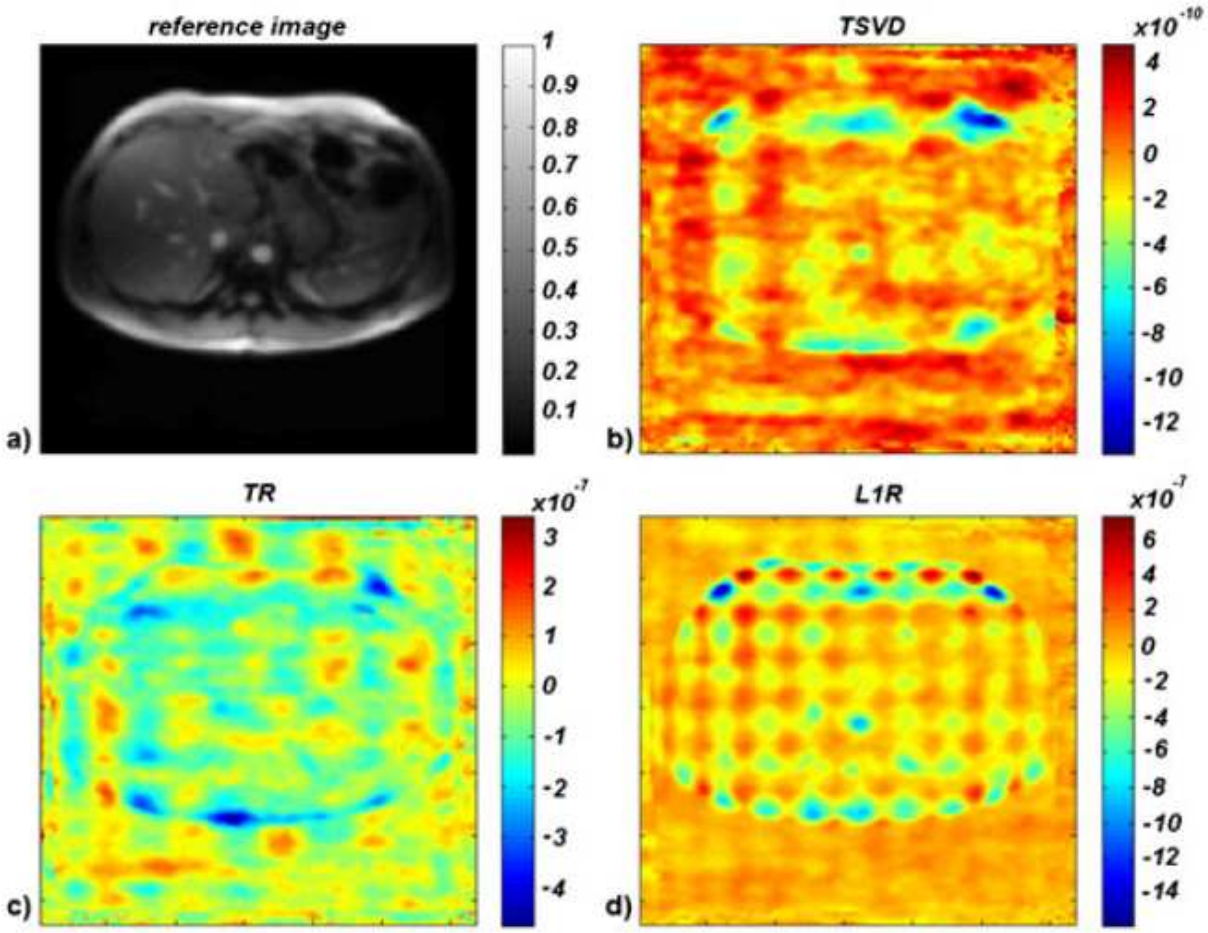

Fig. 21 *Difference image for raw data from human abdomen. a) Reference reconstructed image (128×128) obtained using DS. b) Difference image for the best interpolator obtained with TSVD (q=24). c) Difference image for the best interpolator obtained with TR (q=14). d) Difference image for the best interpolator obtained with L1R (q=30).*

The following figure shows the results for the processing time needed to calculate the interpolator. As the value of *q* increases, more time is required for calculations. It is possible to observe that the TR interpolator was the quickest to be calculated. The TR interpolator was calculated approximately as rapidly as the interpolator without regularization. The TSVD interpolator required a longer time for calculation, whereas the L1R interpolator was by far the slowest to be calculated.

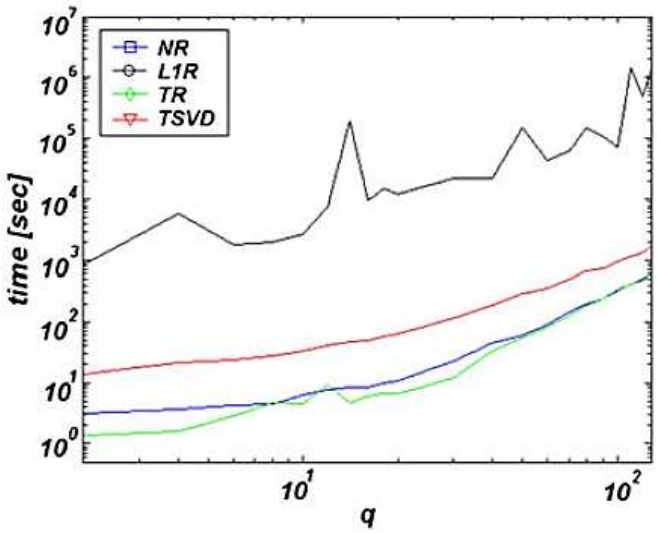

Fig. 22 *Processing time needed to calculate the interpolator for LS_NUFFT with NR and for regularized reconstruction. Processing time is plotted as a function of q using logarithmic scale for vertical axis.*

1.4.5. Discussion on the regularization methods applied to LS-NUFFT

The guide role of pseudoinverse for choosing the interpolator allows LS-NUFFT to obtain a remarkable efficiency of reconstruction. The increase in interpolator width makes the problem ill-conditioned, limiting the possibilities of the reconstruction method. The choice of the most appropriate regularization technique is a key point to fully take advantage of the LS-NUFFT method. The aim of the present study was to determine which regularization technique performs the best for LS-NUFFT.

Three well-known regularization methods where tested on the reconstruction method. TSVD was able to obtain a minimum value of *RMSE(q)* smaller than without any regularization. Therefore TSVD can be used to improve the performance of the reconstruction method. However, the required processing time is about one order of magnitude higher compared to the NR method, because SVD decomposition has to be calculated and this is time consuming. The value of *RMSE(q)* for TR is about the same as the error for the best interpolator without regularization. Hence, increasing *q* applying TR will not increase the quality of reconstruction. The performance of L1R was similar to TR, although a little worse. For L1R the reconstructed image had an acceptable *RMSE(q)* but it was bigger than the error for the other regularization methods.

Moreover, the processing time required by the L1R algorithm was three orders of magnitude higher than that of NR. A possible explanation is the fact that the Newton's interior point method becomes slower as the regularization parameter λ_{L1} decreases to values similar to the one we used.

The presence of noise on the input data seems to have no effect on the results. In fact the results obtained with the SL phantom and with the real dataset are comparable.

The study results showed that TR and L1R regularization algorithms do not provide significant improvements in image reconstruction with respect to standard reconstruction without regularization. An interpolation dimension of $q = 14$ without regularization will provide a lower reconstruction error with respect to TR and L1R. A possible application of the TR method is to obtain a good reconstructed image eve in the case of erroneous choice of the q value, without a significant increment in the processing time.

The only regularization algorithm able to outperform the standard reconstruction method is the TSVD method. We found that the increased interpolator size in TSVD improves the reconstruction accuracy. TSVD had a minimum value of *RMSE(q)* for $q = 24$ in simulated data. After this point, the *RMSE(q)* remains stable increasing q. However, if the interpolator is wider, the computational cost of the interpolation increases accordingly, so a trade-off exists between reconstruction quality and processing time. The increase of q is advisable in case it is more interesting to reduce the reconstruction error, instead of saving processing time.

Many aspects of the acquisition depend on the sampling trajectory to fill the k-space. If the trajectory undersamples the k-space, the reconstructed image will show artifacts. However, the trajectory shape does not have any effect on the conditioning number of matrix A. This is confirmed by the formulation of Fessler and Sutton [22]. They showed more clearly that the interpolator is calculated using the pseudoinverse of the matrix (called *SC* in reference [22]) that does not depend on the sampled pulsation. This shows that trajectory design cannot improve the conditioning of the problem.

In this paper only values of q up to M were considered in order to keep the A matrix skinny or square, looking for the least square solution of the linear system. If $q > M$ then the linear system becomes underdetermined, and it may be interesting to investigate the behaviour of the least norm solution. However, even if the least norm interpolator improves reconstruction accuracy,

the associated computational complexity would be even higher than for least squares interpolator; thus, it may be not suitable for the user's purposes.

Moreover in the present analysis of the regularization methods, the geometric information loss was not included. A variation of the error image structure was observed in the data, but further investigation on this topic is still to be done and could be an interesting development of the present study.

The term regularization generally refers to any method that includes additional information to solve a problem. Other numerical methods and regularized processing techniques applied to biomedical field can be found for example in [56, 57]. This study focused on the analysis of a proper regularized interpolator for LS-NUFFT on MRI data. The interpolator is basically used as a filter in the Fourier domain, in order to determine the interesting values of the transform. A class of local spectral wavelet filters, discrete singular convolution (DSC) filters, has recently been introduced in [58]. This kind of low-pass filter can be adjusted in order to achieve very good performance in the removal of Gibbs oscillations while retaining the high resolution features. Another kind of high-performance low-pass filter, has been recently described in [59] and [60]. These filters are based on the proper choice of parameters for nonlinear partial differential equation (PDE) models. A comparison between the regularized filters proposed in [56 -60] and the one proposed in the present work for interpolation, would be an interesting topic for future work.

1.4.6. Conclusions for the regularization methods study

Three regularization methods were applied to the LS-NUFFT reconstruction method. The increase in interpolator width improves reconstruction as long as $q \leq 14$. For $q > 14$ regularization is advisable in order to improve the performance. Tikhonov Regularization (TR) method is able to preserve the reconstruction quality for $q > 14$ without increasing the processing time. Hence, TR may be useful if the optimal value of q cannot be determined in advance and processing time is an important constraint. Truncated Singular Value Decomposition (TSVD) was able to obtain a minimum error (*RMSE*) about two orders of magnitude smaller than the minimum *RMSE* of LS-NUFFT without regularization. However, the processing time associated

with TSVD is significantly higher, so an appropriate compromise between processing time and reconstruction quality should be adopted.

2. SECTION 2: PULSE SEQUENCE DEVELOPMENT

2.1. INTRODUCTION

The research on MRI topics can be distinguished in three main branches: software, hardware and reconstruction. The software development takes care about which electromagnetic field the machine should play in order to collect the interesting data. The hardware field is focused on how the signal can be physically acquired. The reconstruction field studies how to retrieve the interesting information from what has been collected.

The pulse sequence development belongs to the software field of research. Every company building MR scanner has its own proprietary development environment for pulse sequences. However the problems to overcome do not only concern coding issues, but there is always a close relationship with the physics of the MR technology. The following figure, shows and example of how coding 'bugs' can strongly influence the appearance of the resulting image. On the left is shown the correct image of a phantom obtained with a Fast Spin Echo (FSE) sequence. On the right is shown the image obtained with the same sequence, but setting the wrong value to the isodelay of the excitation pulse. A wrong isodelay results in a wrong value of the area of the rephrasing pulse after the slice selection gradient. Therefore it is as if in the sequence there was an additional gradient which modulates the spins, similarly to the tagging sequences.

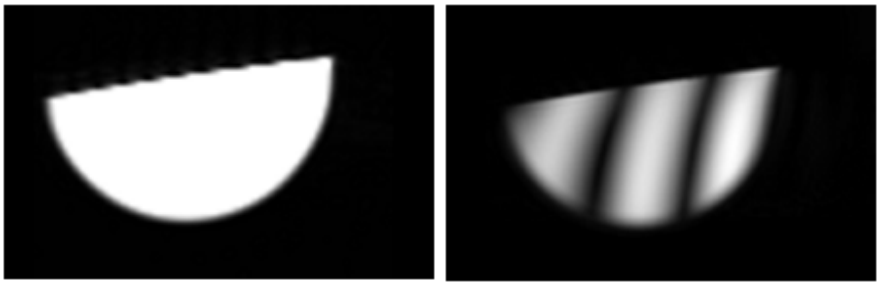

Fig. 23 *Example of image obtained with a wrong value of isodelay for the excitation pulse.*

A 'sequence' is the series of RF pulses and gradients that the scanner is supposed to play. The structure of the sequence and the timings associated with it determine the type of information

collected from the tissues. Depending on the information that one wants to gain from the tissues, the sequence needs to be adapted for that purpose.

In this work of thesis the pulse sequence development was focused on two main topics: cardiac imaging and lung imaging. Both these topics have the common problem that the interesting organ is moving periodically. The acquisition needs to avoid the motion synchronizing always with the same phase of the motion. For the lung it is possible to control the motion and stop breathing for a limited time. Conversely, for the heart, the motion cannot be controlled and the acquisition needs to adapt to the heart behaviour.

2.2. CARDIAC IMAGING

2.2.1. Introduction on cardiac imaging sequence development

An interesting research area for heart imaging is the quantitative map analysis. MRI generally produces images with a contrast depending on more than one parameter characterizing the tissues (PD, T_1 and T_2). From these images it is possible to have a qualitative inspection of the health condition of the organs. However there are some quantitative approaches which allow a more objective exploration of the condition of the tissues.

The transverse relaxation time (T_2) of the myocardial tissue is altered in several pathological conditions. In case of edema following an acute myocardial infarct, an increase in T_2 is observed owing to the altered water content of the myocardial tissue [61, 62]. An increase in myocardial T_2 can be associated with severe transient myocardial ischemia [63, 64] or myocarditis [65], as well as heart transplant rejection [66]. However, a decrease in the myocardial T_2 may also be observed, for example, in case of iron overload in the heart [67]. Iron overload is typically associated with thalassemia, a disease in which the production of globin is defective and unbalanced [68, 69]. Thalassemia is caused by the weakening and destruction of red blood cells, due to the variant or missing genes that affect how the body makes hemoglobin. Cardiac failure can be facilitated by thalassemia, and thus, an early diagnosis of myocardium iron overload is the best strategy to reduce mortality in such cases [70]. Iron accumulation in myocardial tissue leads to a decrease in T_2* and T_2 in the tissues, owing to a susceptibility-induced relaxation [71].

Changes in T_2 in pathological tissue can be visualized using T_2-weighted imaging [72], which is prone to inaccuracy arising from several possible sources [73, 74]. The main cause of this inaccuracy lies in the qualitative nature of T_2-weighted images, where contrast can change depending on sequence parameters like the echo time or the repetition time. Stagnant blood can appear with a high signal, so that it can be difficult to distinguish it from edema. It has been demonstrated that T_2 maps have higher accuracy than T_2-weighted images for detecting pathological tissue in the myocardium [75]. The higher accuracy can be attributed to the quantitative nature of the T_2 maps.

The following image shows how the T_2 maps can actually identify myocardial infarction as good as with the use of a contrast agent.

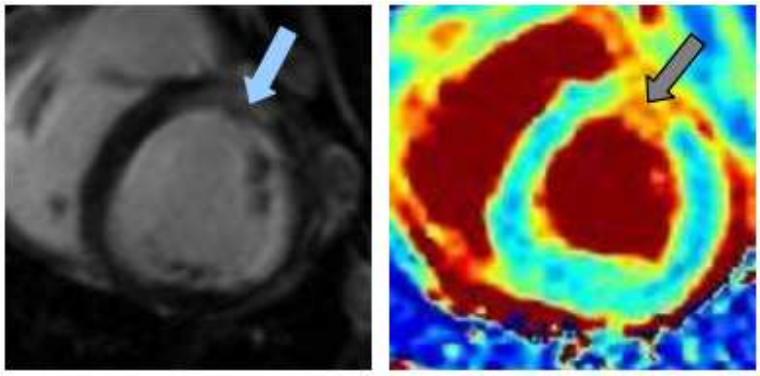

Fig. 24 *Comparison of Lade Gadolinium Enhancement (left) and T_2 map on pig with visible myocardial infarction. [75]*

Various T_2 mapping techniques have been proposed for generating T_2 maps of the heart. Double inversion recovery Multiple-Echo Fast Spin Echo (MEFSE) is the most common pulse sequence [76 - 79]. The double inversion recovery preparation nulls the signal from blood, thus avoiding flow artifacts [72]. T_2 maps can also be generated using sequences with a T_2-preparation, followed by a fast acquisition, such as FIESTA [79] or spiral [80]. Double inversion recovery MEFSE has been shown to provide the highest signal-to-noise ratio (SNR) among the different T_2 mapping techniques [81], and hence, it was considered for the present work.

For cardiac imaging, the low B_0 magnetic fields are generally preferred. In the case of lower fields (e.g. 1.5T) typically fewer artifacts appear in the images (e.g. 3T). This is due to the wave length of the RF used, which directly proportional to the static B_0 field as the Larmor formula

states. For higher fields the wave length will become smaller and comparable with the size of the body, especially in the case of chest imaging. Therefore the RF pulses will generate interference patterns and thus B_1 inhomogeneities causing artifacts in the images. For the present study a 3T scanner was used in order to optimize this technology. Better images can be obtained at 3T using a dielectric padding on the chest of the patient. This padding acts on the RF reaching the tissues, making the B_1 more homogeneous and stronger on the whole chest. The following image shows the signal improvement obtained with the use of the padding:

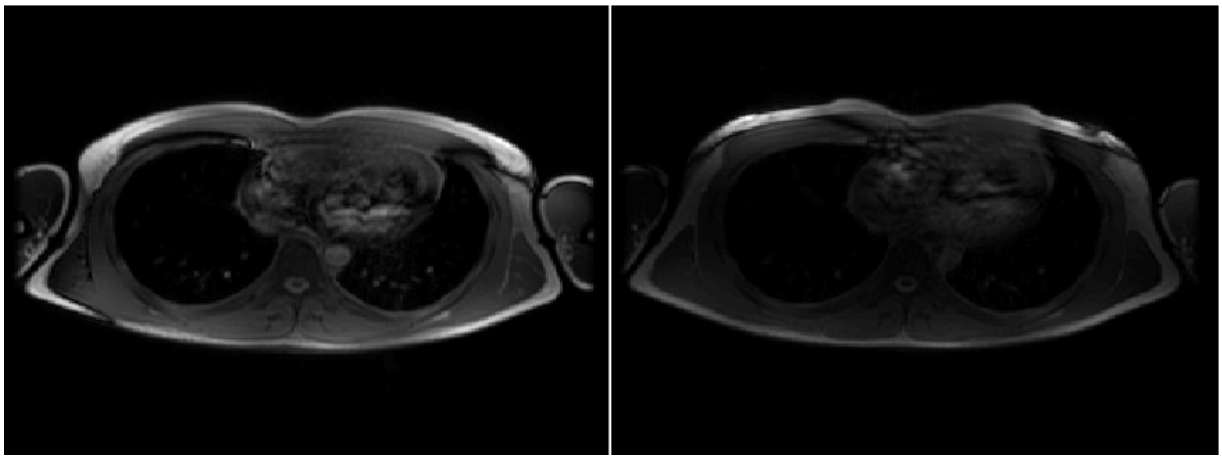

Fig. 25 *Chest image from a FGRE localizer sequence with dielectric padding (left) and without it (right).*

For cardiac MRI, the acquired field-of-view (FOV) is often larger than the region of interest. To avoid image aliasing, the FOV must be extended to areas of the chest far from the heart. The acquisition of a FOV larger than that required can lead to a prolongation of scan time. Moreover, if the FOV needs to be large to avoid image aliasing, the spatial resolution achievable at a fixed scan time is lower.

Techniques to acquire signal from a limited volume include inner volume (IV) and multi-dimensional pulses. IV is a FOV reduction method that requires both excitation and refocusing pulses. IV uses orthogonal slice selection planes for excitation and refocusing, thus generating a spin-echo only from a restricted portion of the FOV [82 - 84]. The following figure shows a scheme of how the IV excitation and refocalization work:

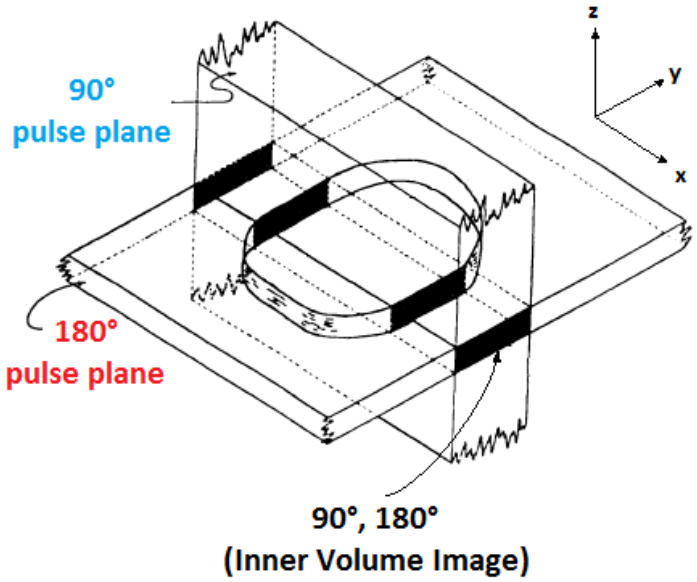

Fig. 26 *The inner volume excitation and refocalization are played with orthogonal slice selection gradients.*

Multi-dimensional spatially selective pulses (2D-RF) have been proposed as an alternative method to reduce the FOV without aliasing [85, 86]. These pulses are similar to spectral-spatial pulses [87, 88], except that they encode the spectral information along the slice direction. 2D-RF pulses are generally much longer than common excitation pulses, making it difficult to sample the short T_2 decay of the myocardium quickly enough. The duration of 2D-RF pulses can be reduced using parallel transmission, which takes advantage of the coil sensitivities of the transmit coil arrays [89]. However, this work focuses on a clinical MRI system that is not capable of applying parallel excitation. Another disadvantage of 2D-RF pulses is their sensitivity to off-resonance. The following scheme shows how the 2DRF selection happens:

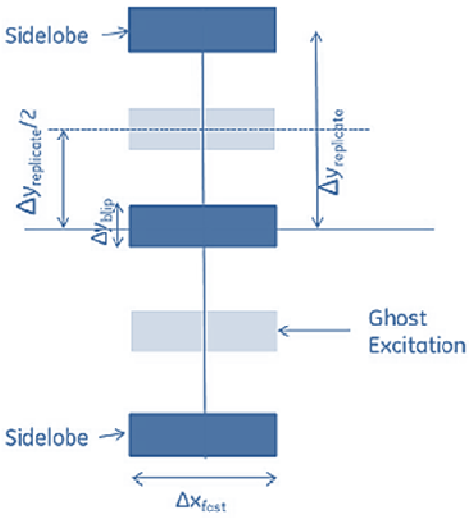

Fig. 27 *2D-RF excitation scheme. The frequency modulation of a spectral-spatial pulse is mapped on the slice encode direction. The ghost excitation patterns need to be cropped out with some selective refocusing pulse.*

The IV was chosen as preferred FOV reduction technique because it fits the fast spin echo pulse sequence well. However some tests were performed using a 2D-RF pulse as well. The results obtained with the 2D-RF excitation will be shown, even though the work on this topic is still in progress.

The IV technique for FOV reduction was combined with the double inversion recovery MEFSE sequence (called IV-MEFSE) to produce T_2 maps in the myocardium. The T_2 values obtained with MEFSE were taken as reference for comparison. The new pulse sequence was evaluated in phantoms and healthy volunteers pointing out the effects of the IV excitation over the T_2 maps evaluation.

2.2.2. Sequence implementation and experimental setting

The T_2 maps were obtained with the double inversion recovery MEFSE sequence and triggering by the ECG signal. Within a single breath-hold *N* images at different echo times were acquired to create the T_2 maps. The echo train of the MEFSE sequence was split into *N* groups (dotted line in Fig. 28) and the phase encode (PE) ordering was repeated for each group. The repetition of the PE ordering at different time delays from the excitation pulse enabled acquisition *N* images at

different echo times (TE). The shortest TE is determined by the center-out PE ordering. Later images have a fixed TE increment (ΔTE) depending on the echo spacing (ESP), the echo-train-length (ETL), and the number of images acquired (*N*): ΔTE = (ETL/*N*)*ESP.

Inner volume imaging was accomplished by perpendicular slice selection for the excitation and refocusing pulses. As shown in Fig. 28, the excitation pulse is applied together with a slice selection gradient in the PE direction, whereas the slice selection gradients of the refocusing pulses are applied along the slice encode direction (SE).

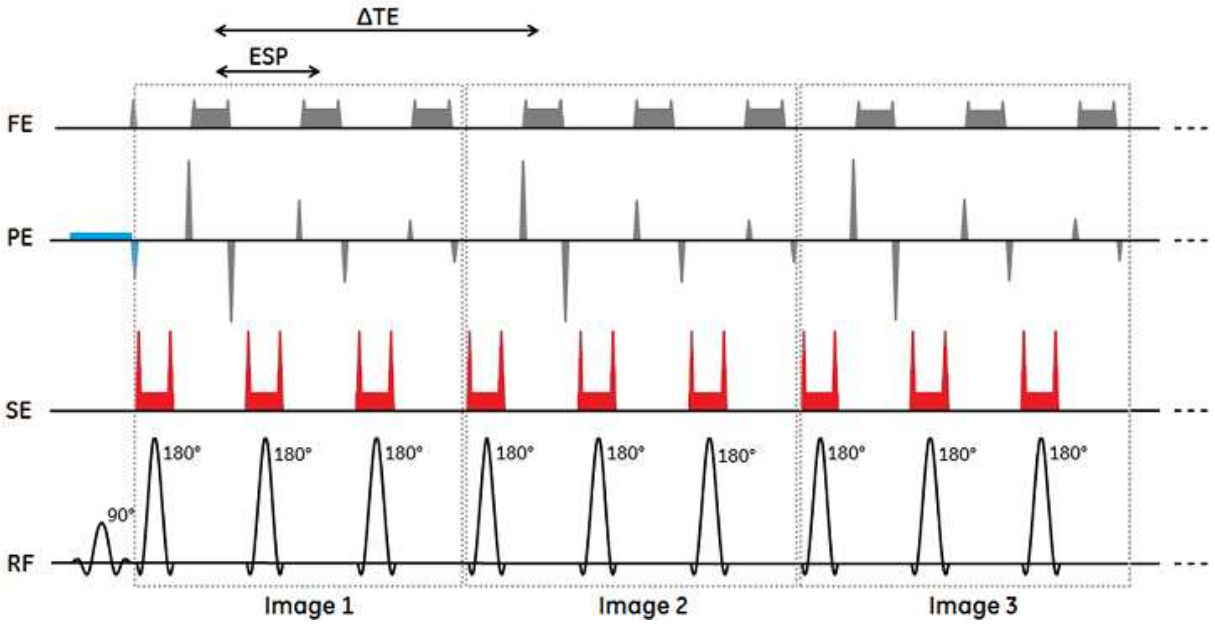

Fig. 28 *Diagram of the IV-MEFSE sequence. The slice selection gradient for the excitation pulse is in the phase-encode direction (PE), whereas the slice selection gradients for the refocusing pulses are in the slice-encode direction (SE). The frequency-encode direction (FE) and RF pulses are shown as well. The figure represents an example of ETL = 12 and 4 images (echo times). For this example, the TE increment in the images equals ΔTE = 3*ESP.*

A highly selective profile of the excitation pulse is the key for successful IV acquisition. A signal generated outside of the region-of-interest (ROI) can be neglected only if the sharpness of the excitation profile and the suppression of signal outside of the FOV is sufficient. For IV, the FOV in the PE direction corresponds to the slice thickness of the excitation pulse. Different excitation pulses were designed using the Shinnar-Le Roux (SLR) transform [90]. With the same maximum B_1, a better selectivity can be achieved with a longer pulse, having a higher time-bandwidth-

product. However, it is relevant to keep the duration of the RF pulses as short as possible, because the ESP and the ΔTE are directly dependent on it. Three different excitation pulses were compared: the default MEFSE linear-phase excitation pulse (RF1), a minimum-phase pulse (RF2), and a linear-phase pulse (RF3). The latter two had a more selective excitation profile than RF1. The following figure shows the profile of the excitation pulses used:

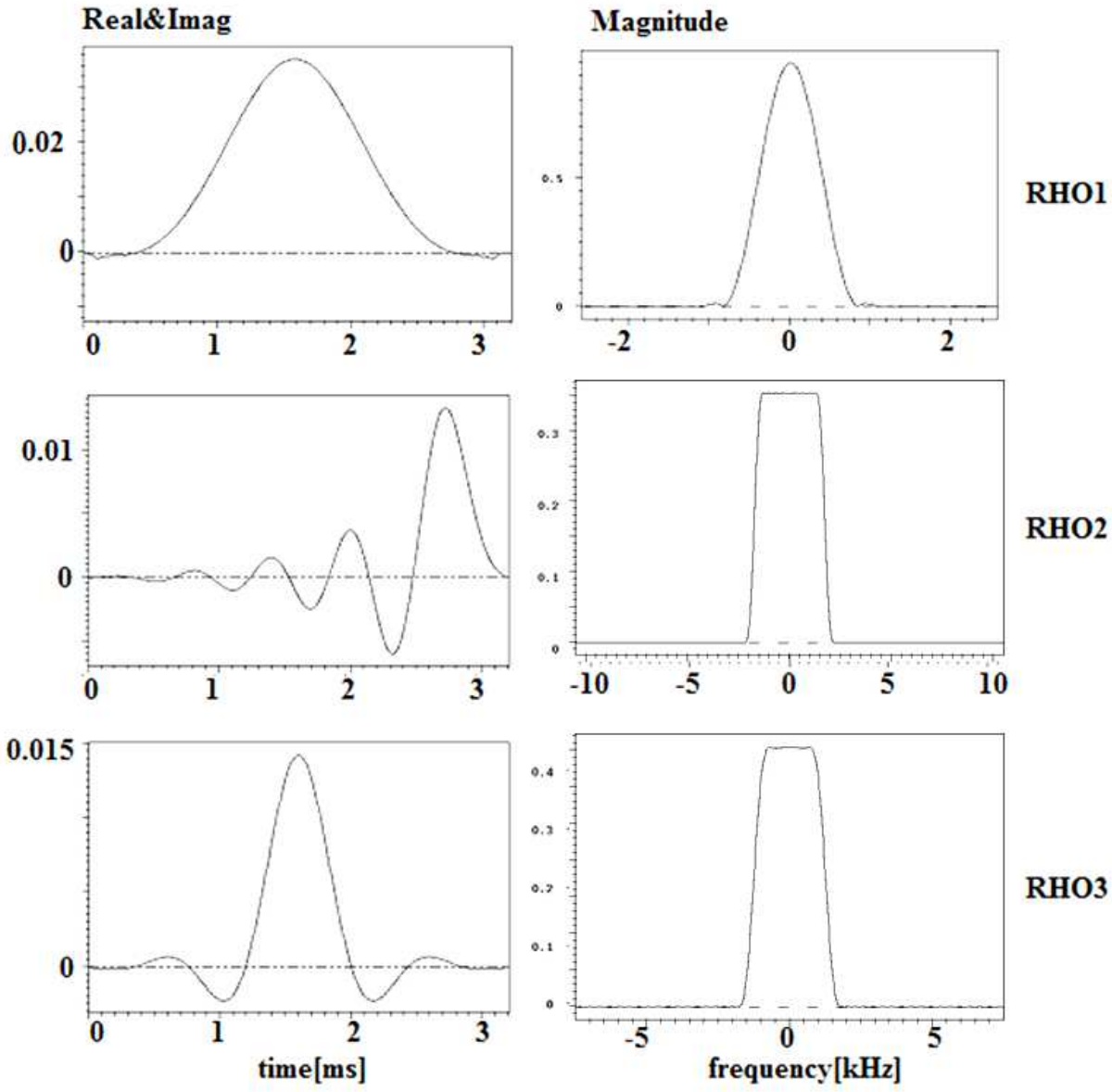

Fig. 29 *Profile of the excitation pulses tested in the time domain (left column) and in the frequency domain (right column). The pulses shown are RF1 (top row), RF2 (middle row), RF3 (bottom row).*

The parameters of these pulses are listed in Tab. 2. The experiments were performed on a simple phantom of water and copper sulfate ($CuSO_4$) [91], with T_2 similar to myocardium [92, 93]. The accuracy of the generated T_2 maps is strongly dependent on the presence of stimulated echoes (STEs), which may introduce a longitudinal relaxation time (T_1) contribution to the signal decay [94]. Three different refocusing pulses (RF4, RF5, and RF6) were designed, with different durations and thus different selectivity (Tab. 2), in order to explore the effect of the generated STEs.

Pulse	Pulse type	Pulse duration [ms]	Bandwidth [kHz]	Pass-band ripple (%)	Stop-band ripple (%)	max. B_1[G]
RF1	Excitation	2	1.28	1	1	0.08
RF2	Excitation	3	2.5	0.2	0.2	0.20
RF3	Excitation	3	2.5	0.2	0.2	0.16
RF4	Refocusing	1.2	1	1	1	0.24
RF5	Refocusing	2.1	1.2	0.5	0.5	0.24
RF6	Refocusing	6	1	0.5	0.1	0.23

Tab. 2 *Parameters of excitation and refocusing pulses. The nominal flip angle is 90° for excitation and 180° for refocusing. All pulses are linear-phase, except for the minimum-phase pulse RF2.*

Volunteer examinations were performed by acquiring short-axis T_2 maps of the myocardium within the breath-hold time. For MEFSE the following scan parameters were used: ELT = 24, N = 8 echo times, ESP = 5.7ms, FOV = 24 cm, 256 frequency encodes, 128 phase encodes, receive bandwidth ±62.5 kHz, 1 acquisition per heart-beat, black-blood preparation, half-echo acquisition, and scan time = 24s. For IV-MEFSE the longer excitation pulse (3ms) prolonged the ESP to 7.7ms. Double inversion recovery preparation was used for IV-MEFSE as well. All experiments were performed with an 8-channels torso surface-coil array on a GE 3T HDx scanner (GE Healthcare, Waukesha, WI, USA).

For the T_2 fitting the first echo was not used because of the presence of stimulated echoes starting from the second echo [94]. The T_2 maps were computed using a mono-exponential 2-parameter fitting model [95]. The following figure shows an example of decay where the first echo is lower than the following ones:

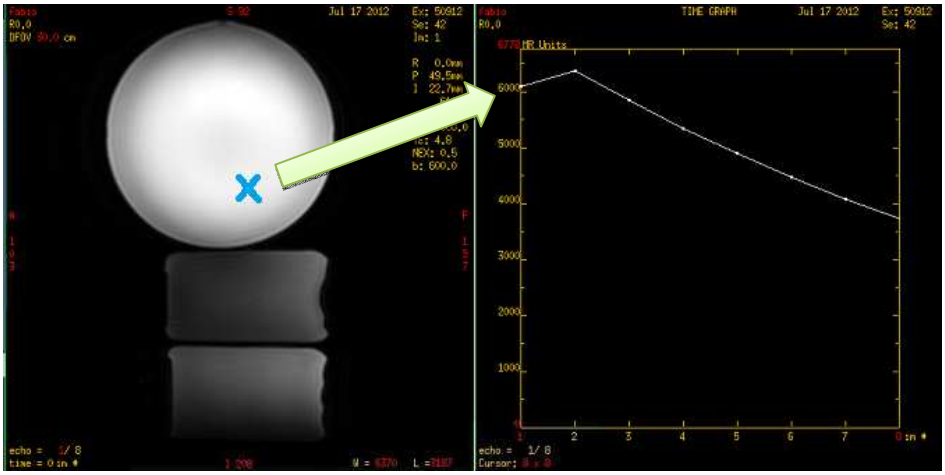

Fig. 30 *Example of decay on a phantom, where the first echo is lower than the following ones due to the absence of the stimulated echoes.*

2.2.3. Results

IV-MEFSE was first evaluated on phantoms. Fig. 31 shows the results obtained using different excitation pulses on the phantom. The short linear-phase pulse (RF1) did not lead to sharp edges of the FOV (Fig. 31(a)). For RF1, the excitation profile is clearly visible as shading on the imaged FOV. Fig. 31(b) shows that the minimum-phase pulse RF2 could produce sharp edges in the selected FOV. However, some artifacts are visible due to the inability of the linear gradient to rephase the spins completely. The artifacts appear as dark bands along the PE direction and extend outside the selected FOV. Fig. 31(c) shows that the linear-phase pulse RF3 was the only pulse that could apply inner volume selection with sharp edges, while avoiding the phase dispersion of the spins and thus avoiding artifacts.

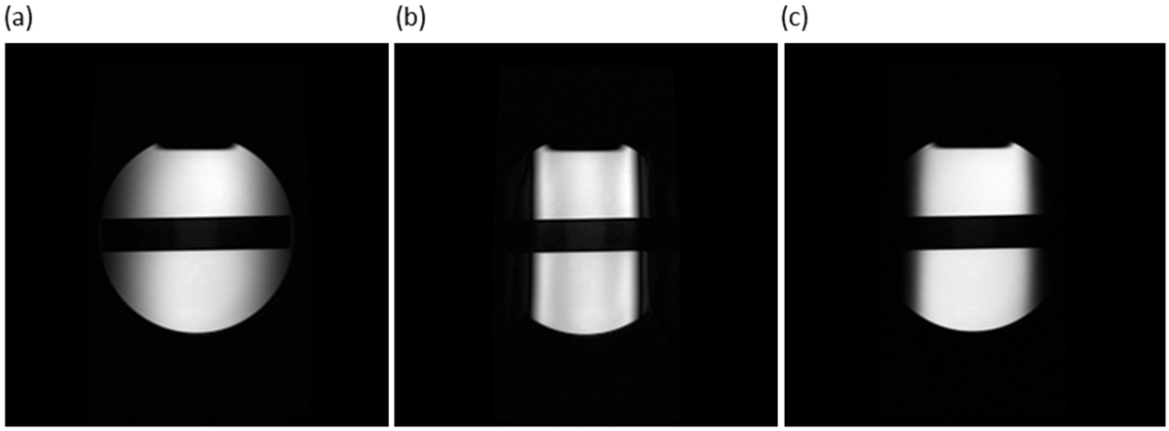

Fig. 31 *Results of IV-MEFSE on a phantom using different excitation pulses. (a) IV-MEFSE with standard short linear-phase excitation pulse (RF1): the FOV does not have sharp edges. (b) IV-MEFSE with sharp minimum-phase excitation pulse (RF2): even though the FOV edges are sharp, the non-linear phase dispersion cannot be rewound. Artifacts are visible as dark bands along the PE direction. (c) Highly selective linear-phase excitation pulse (RF3): the FOV edges are sharp and the linear phase dispersion is rewound with the rewind gradient, causing no artefact.*

In the phantom experiments, two FOVs were tested in order to analyze the effect of the transition bands of the excitation pulse on the formation of stimulated echoes (Fig. 32). The phantom was 30 cm wide along the PE direction. A large FOV of 44 cm (Fig. 32(a)) was used to make sure that the transition bands of the excitation pulse were outside of the phantom. A small FOV of 20 cm (Fig. 32(b)) was used to make sure that the transition bands of the excitation pulse were located inside the phantom. The averaged T_2 values measured with the sequences are listed in Tab. 3. IV excitation produced an overestimation of T_2 compared to MEFSE. IV-MEFSE using a large FOV led to a smaller T_2 overestimation with longer refocusing pulses (Fig. 32(c)). MEFSE with a large FOV did not show any T_2 overestimation with any of the refocusing pulses. In case of reduced FOV, IV-MEFSE caused overestimation with any refocusing pulse (Fig. 32(d)). The T_2 overestimation caused by the presence of the reduced FOV is dominant over the effect of different refocusing pulses. For phantom scans, IV caused an overestimation of 23±2% of the T_2 value compared to MEFSE.

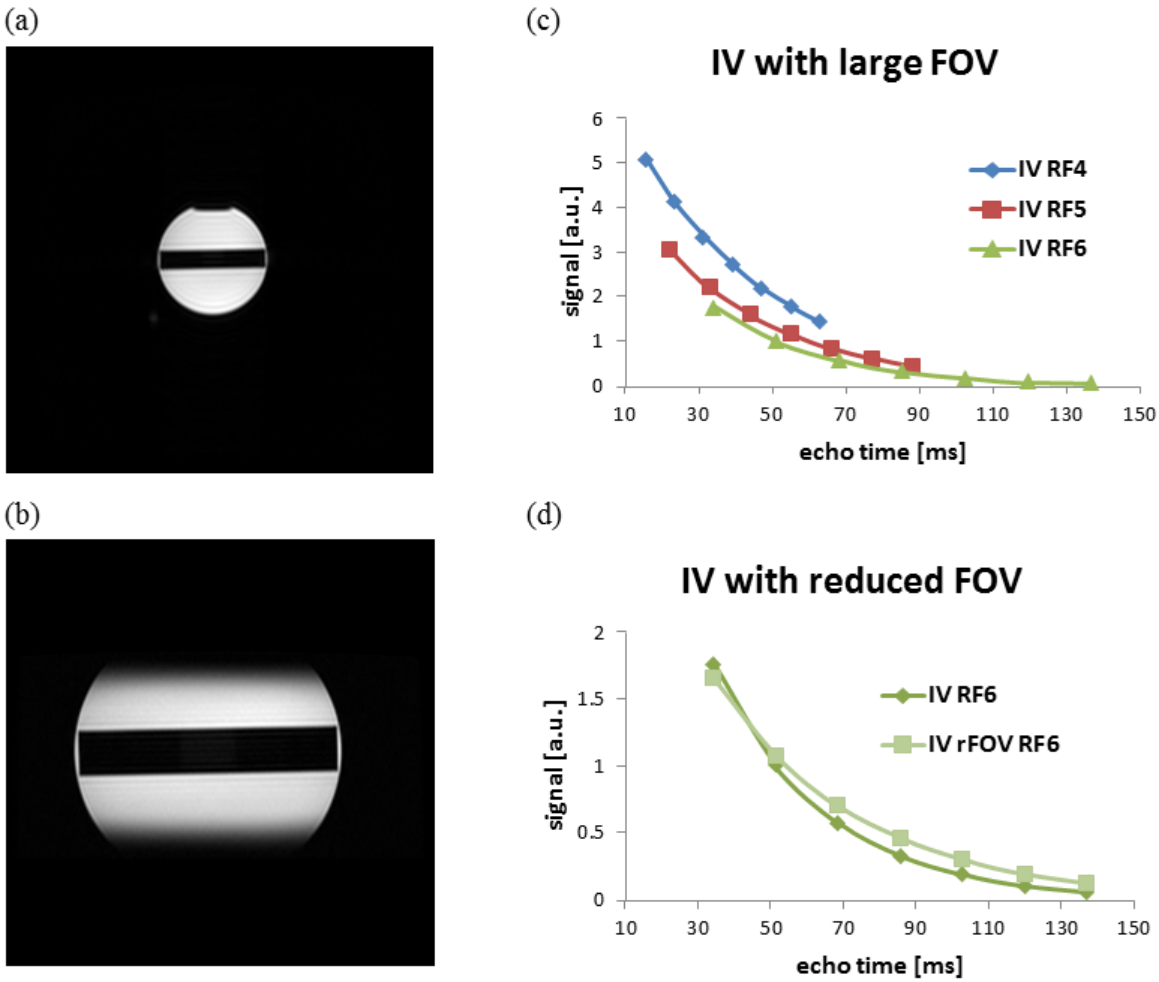

Fig. 32 *Phantom experiment using different FOVs and different refocusing pulses. The first column shows: (a) a large FOV (44 cm) covering the entire phantom so that the transition zones of the excitation pulse do not invest any spin; (b) a reduced FOV (20 cm) covering part of the phantom so that the transition zones invest some spins. The second column shows comparisons of the signal decays (echoes 2 to 8). (c) Decay curves obtained using RF4, RF5, and RF6 as refocusing pulses, with a large FOV. The acquisitions have different ESP. As the refocusing pulses becomes longer, the overestimation of the T_2 decreases. (d) Decay curves obtained using the same refocusing pulse (RF6) using MEFSE with large FOV and using IV-MEFSE with large FOV and with reduced FOV (rFOV). IV introduces an overestimation of T_2 that is more pronounced in case of reduced FOV.*

In a volunteer examination, IV-MEFSE enabled acquisition of a smaller FOV in the phase encode direction (Fig. 33), leading to a scan time reduction. With the halved FOV, the number of phase encodes could be reduced while keeping the same pixel size. Compared to MEFSE the scan time was reduced from 23s to 15s.

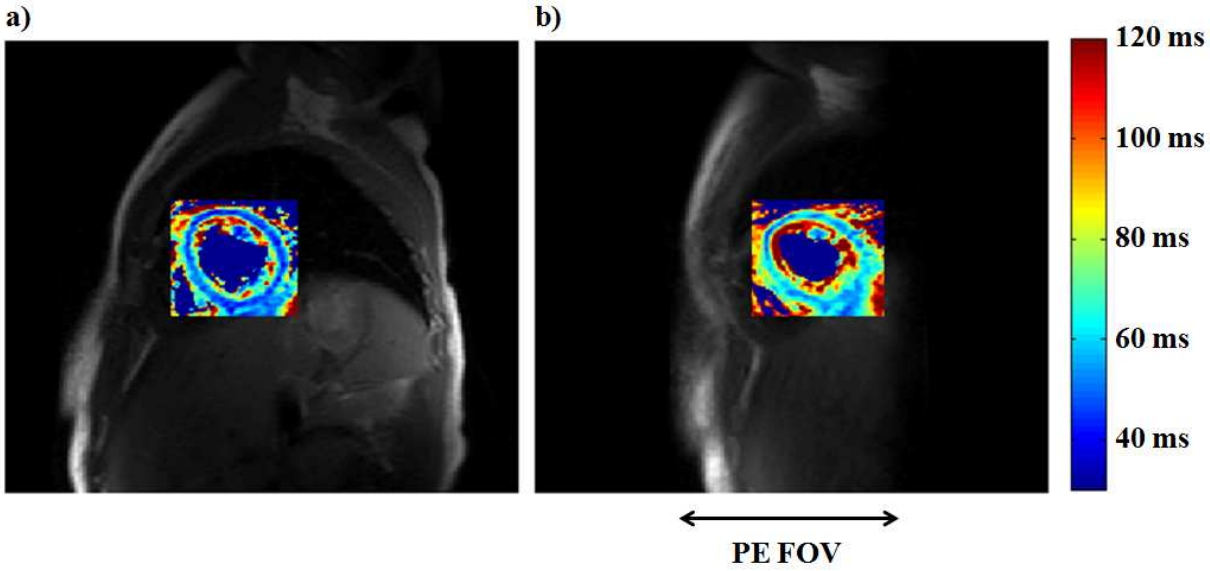

Fig. 33 *In vivo short axis plane using MEFSE (a) and IV-MEFSE (b) with same pixel size as MEFSE but halved scan time. In the case of inner volume, it is possible to observe an overestimation of the T_2 values on the maps. The arrow in (b) shows the reduced FOV selected along the PE direction.*

The following image shows how the inner volume excitation was successful in reducing the FOV without generating aliasing:

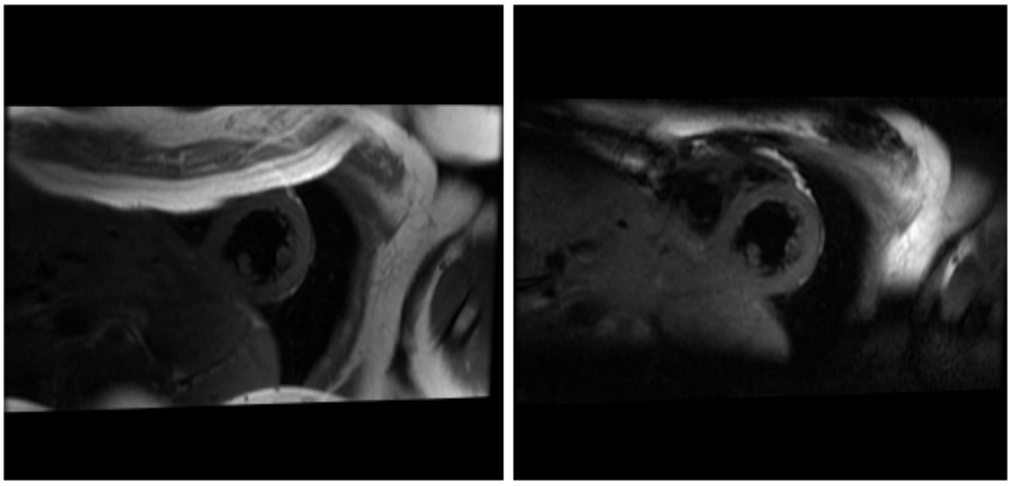

Fig. 34 *Left: FOV reduction with standard T_2 mapping and no inner volume selection; Right: same acquisition but using inner volume excitation. It is possible to observe that for MEFSE the aliasing of the image is prominent, whereas for the IV-MEFSE the signal outside of the selected FOV is negligible.*

In the volunteer examinations, a T_2 overestimation due to IV excitation was observed, similarly to the phantom experiments. Tab. 4 shows the mean values obtained over the myocardium of four representative volunteers. The average value of the myocardial T_2 was 55.2±6.8 ms for MEFSE and 66.0±8.1 ms for IV-MEFSE, corresponding to an overestimation of 20±7%.

Refocusing pulse type	FOV	IV	mean T_2 [ms]
RF4	large	no	38.3±1.2
RF5	large	no	39.2±2.1
RF6	large	no	39.1±3.3
RF4	large	yes	47.8±2.2
RF5	large	yes	44.5±2.1
RF6	large	yes	40.6±4.1
RF4	reduced	yes	49.1±2.2
RF5	reduced	yes	47.0±2.4
RF6	reduced	yes	48.2±4.7

Tab. 3 *Average T_2 values of phantom scans using different FOV and different refocusing pulses. The excitation pulse is RF3 in all cases.*

	Vol_1: T_2[ms]	Vol_2: T_2[ms]	Vol_3: T_2[ms]	Vol_4: T_2[ms]
MEFSE	53.1±6.1	52.1±6.4	60.2±7.2	55.4±8.1
IV-MSEFSE	60.2±9.1	71.2±9.4	65.5±8.5	66.9±6.6

Tab. 4 *Average T_2 values over the myocardium obtained in four representative volunteer scans at 3 Tesla.*

2.2.4. Discussion on Inner Volume T_2-mapping

A modified version of the MEFSE was presented, where it is possible to acquire a reduced FOV without image wrapping. The reduced FOV was obtained with inner volume excitation. The sequence was used to produce T_2 maps of the myocardium, significantly reducing scan time and remarkably facilitating the scan prescription. Scan time reduction obtained with IV can be relevant for patients that have difficulties in holding their breath. For the unmodified MEFSE the breath-hold time may be too short for the acquisition of multiple images at different TE. The prescription of a smaller FOV can significantly reduce the scan time, avoiding the acquisition of signal from outside the ROI. Moreover, IV excitation can make the prescription much easier since it is not associated with any image aliasing concern.

Instead of reducing scan time, IV-MEFSE can also be used for increasing image resolution. IV-MEFSE allows doubling the number of PE, while keeping the same scan time of the MEFSE examination, as suggested in [96]. The high-resolution T_2 maps reduce truncation artifacts that might be present as Gibbs ringing in the image.

Alternatively, the scan time could be spent to acquire once every 2 heart beat (i.e. 2 R-R) instead of once per heart beat (1 R-R). The repetition time of the sequence is dependent on the heart rate of the patient. On average the period of the heart cycle is about 60s and this might not be enough to allow a full recovery of the spins in the tissues. If this is the case the acquired images will have a T_1 weighting mixed to the T_2 weighting, causing inaccuracies to the T_2-map. A possible

way to avoid this effect is to increase the repetition time, for example acquiring only once every second heart beat.

An excitation pulse was designed for IV in order to improve the sharpness of the selected FOV, without exceeding a maximum B_1 of 0.2 Gauss. Minimum phase pulses (RF2) were found to be not suitable for inner volume selection. These pulses minimize the phase dispersion of the excited spins allowing a fast rewinding. However the phase dispersion produced by the minimum phase pulses is not linear, thus it cannot be fully rewound by a linear gradient. The residual phase dispersion after the rewind gradient causes artifacts. These artifacts can be avoided using a linear phase pulse for the IV excitation (RF3).

IV imaging caused an overestimation of the T_2 compared to the values obtained with MEFSE. Undesired stimulated echoes due to imperfect pulse profiles led to T_2 overestimation [98]. In order to minimize the formation of STEs, the nominal flip angle (FA) needs to be set to 90° for the excitation pulse and to 180° for the refocusing pulses. However, this may not be enough to make the STEs negligible in the signal decay. The shape of the refocusing pulse nominally produces a flip angle of 180° only in the center of the excitation profile, but the FA is lower in the transition zone, moving farther from the center of the slice. STEs may also be generated by an inaccuracy in the FA calibration of refocusing and excitation pulses. For IV, since excitation and refocusing slices are orthogonal, the number of spins that experience an inaccuracy in the FA for excitation or refocusing is higher than for a standard FSE as shown in Fig. 35. In the case of IV excitation (Fig. 35(a)), more spins are affected by transition zones because the transition zones are not overlapping as in the case of excitation without IV (Fig. 35(b)). The results listed in Tab. 3 show how the STE formation is dependent on the selection profile of both excitation and refocusing pulses.

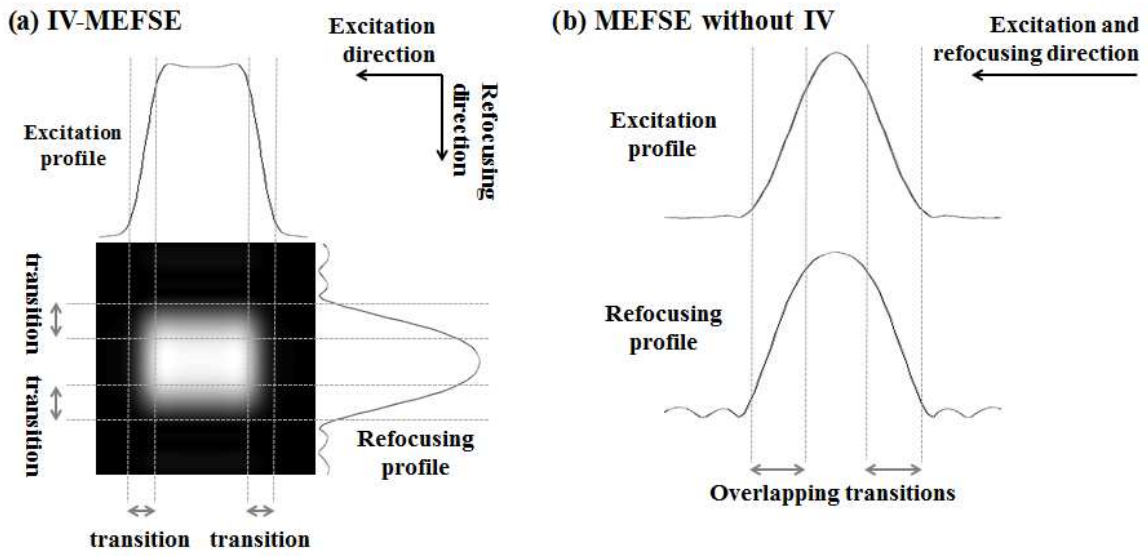

Fig. 35 *Transition bands of excitation pulse and refocusing pulses. (a) IV-MEFSE using RF3 as excitation pulse; (b) MEFSE without IV using RF1. For the orthogonal excitation of the inner volume, the number of spins falling in transition zones and producing STE is higher than in case of matching excitation and refocusing slice.*

In the case of large FOV, the STEs are generated by the transition zones of the refocusing pulses. For IV-MEFSE, if the refocusing pulse is more selective, the STE formation is reduced, resulting in less overestimated T_2 values. However, a more selective pulse has longer pulse duration and therefore may result in echo times that are too long to measure the short T_2 decay of the myocardium. Comparing to IV-MEFSE, MEFSE never led to a significant overestimation for any refocusing pulse used. This is due to the overlap of excitation and refocusing profiles in the slice for MEFSE. Because of the slice profile overlap, the spins experiencing a refocusing FA lower than 180° also experience an excitation FA lower than 90°. In the case of IV-MEFSE with large FOV, all the spins in the slice experience approximately the same nominal excitation FA close to 90°. Therefore, the formed STEs are weaker for MEFSE than for IV-MEFSE, thus not producing a significant prolongation of the T_2 decay.

In the case of small FOV, the transition zones of the excitation profile are within the phantom, and therefore cannot be neglected. Since the slice thickness for the excitation pulse is as large as the FOV in PE direction, the transition bands of the excitation pulse will be much wider than the ones of the refocusing pulses. Therefore, an overestimation will be produced even if the

refocusing pulses give little contribution in the formation of STEs. For *in vivo* scans, this is always the case, since it is possible to take advantage of IV only using a FOV reduction. The level of overestimation caused by IV-MEFSE does not significantly change using different refocusing pulses with reduced FOV. From this observation, the short refocusing pulse (RF4) was used for all *in vivo* acquisitions in order to minimize the ESP.

In volunteer examinations, IV led to an overestimation of the T_2 similar to the one observed in the phantoms scans. However, images showed no visible spatial variation of the maps throughout the myocardium. The STE influence on the T_2 overestimation may vary depending on the T_1 of the tissues experiencing the transition bands of the pulses and on the prescribed FOV. A wider FOV is associated with wider transition bands of the excitation pulse and thus to more STEs. Since the prescription of the reduced FOV cannot be generalized, it would be difficult to model the presence of the stimulated echoes in the decay for a potential correction of the overestimation as suggested in [97]. A T_2 overestimation of about 20% is representative for IV-MEFSE in volunteer examinations.

The solution to completely get rid of the T_2 overestimation would be the use of RF pulses as close as possible to the ideal shape in the frequency domain. However in order to obtain an RF pulse with a sharp frequency profile, the time-bandwidth product (TBP) needs to increase. Since the maximum B_1 usable on a human is generally <0.25G for safety reasons, the TBP can be increased only increasing the pulse duration. With longer pulses the T_2 decay becomes challenging to sample fast enough, especially in the case of the myocardium (T_2~50ms).

For all the effects associated to the use of IV, T_2 quantification using IV imaging should be exercised with caution. IV was presented in this work as a method to reduce scan time. Other scan acceleration methods, e.g. parallel imaging [98, 99] could be a valid alternative to prevent the effects of the IV excitation, obtaining the same advantage in terms of scan time.

2.2.5. Preliminary results on rFOV with 2DRF-MEFSE

As mentioned above a FOV reduction can be accomplished using a 2D-RF as an alternative to the IV approach. The idea of the 2D-RF is very similar to the one of the spectral-spatial pulses. In fact, it works as if the slice-direction selection pulse shape (slow shape) was discretized with a PE-selection selection shape (fast shape). The discretization of the slow pulse shape makes the spectrum periodic in the frequency domain, but this periodicity is mapped in the slice-direction

with a blipped gradient. The following figure shows the shape of the pulse which was used for the myocardial T_2 mapping application:

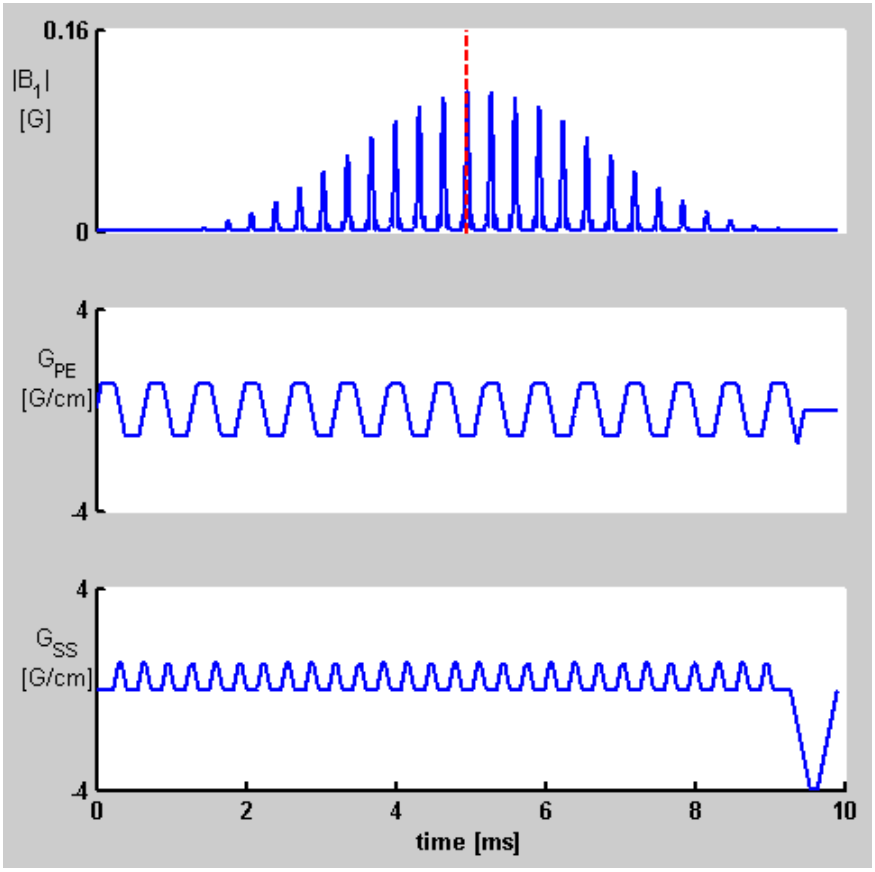

Fig. 36 *Shape of the 2D-RF pulse used for the myocardial T_2-mapping examinations. The pulse was designed to be 10ms long keeping the minimum $B_{1,max}$.*

The periodic excitation profile in the space is generally not desired; therefore a selective refocusing pulse is applied to refocus only the central excited spins. The periodicity of the ghost excitation is dependent on the number of fast shapes that are used in the slow shape. The ghosts get further if more fast shapes are used. Moreover, 2D-RFs generally suppress fat intrinsically because of the chemical shift separation between fat and water.

The problem of the 2D-RF pulses is that they are generally long pulses. As previously mentioned, the use of long pulses in not suitable to sample a fast T_2 decay. For the myocardial T_2-mapping application the 2D-RF was designed as short as possible, reaching the duration of 10ms. There is a trade-off between pulse duration, $B_{1,max}$ and fat suppression. In order to reduce the echo spacing in the FSE sequence scheme and sample the T_2 decay as fast as possible, it was

taken advantage of the difference in length between the 2D-RF excitation pulse and the 1D selective refocusing pulses (duration~2ms). The first echo was collected respecting the width of the excitation pulse, but the refocusing pulses were designed to be spaced as tightly as possible as shown in the following sequence diagram:

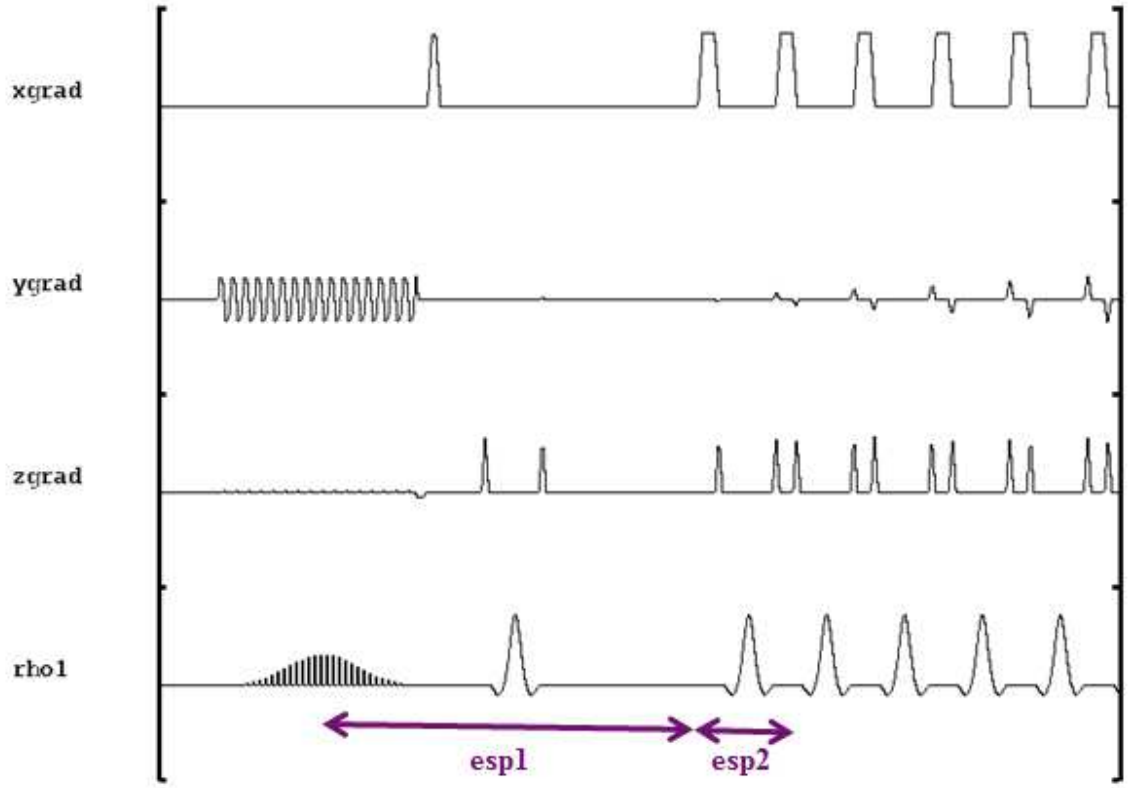

Fig. 37 *Diagram of the MEFSE sequence with the described 2D-RF excitation. As shown in the picture, the first echo spacing is different from the other ones.*

The first echo spacing (esp1) was designed to be an even multiple of the shorter echo spacing (esp2) so that the stimulate echo generated from the excitation pulse would coincide with a refocalization pulse and thus be crushed by the slice selection gradient. This concept is clarified by the following phase graph:

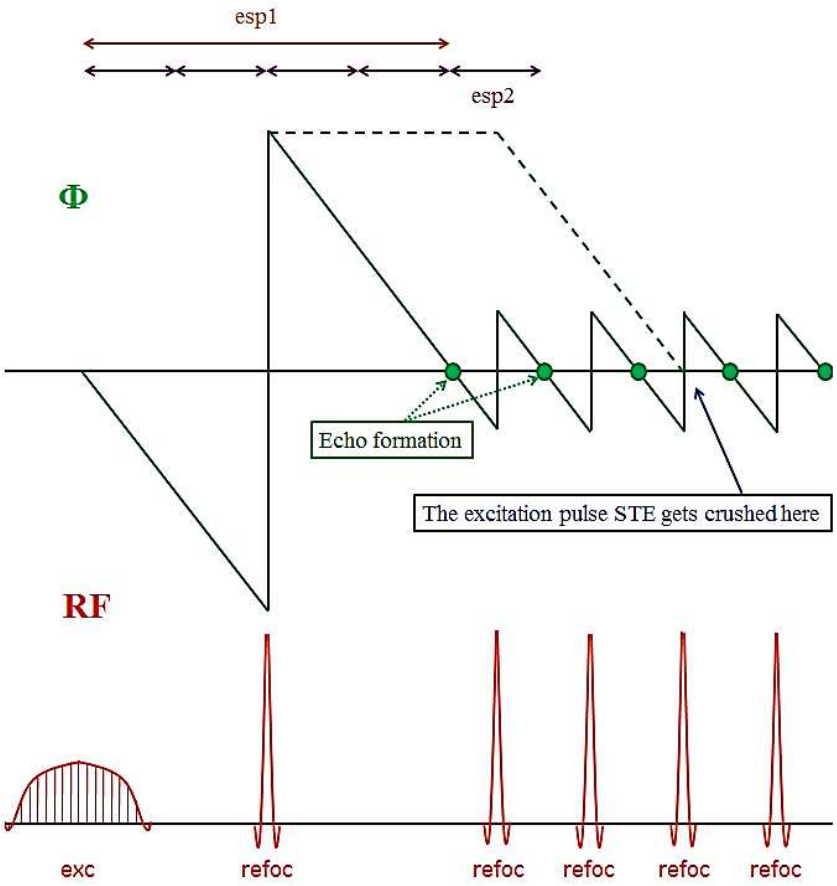

Fig. 38 *Phase graph associated to the 2DRF-MEFSE sequence scheme. The phase (Φ) of the spins is shown on top, whereas the RF pulses are shown in the bottom. When Φ crosses the 0, the spins are rephased and an echo is formed. The stimulated echo (STE) is generated from the magnetization stored in the longitudinal direction. Choosing esp1 equal to an even multiple of esp2, the STE coming from the excitation pulse (i.e. the strongest STE) ends up corresponding to one of the refocusing pulses. Therefore the STE will be crushed by the slice selection gradient associated with the refocusing pulse and will not interfere with the acquired signal.*

For the acquisition, esp1 was about 15-20ms and esp2 was about 5ms and again the scheme of MEFSE was kept the same (8 echoes with ETL=24). The first echo acquired in the T_2 decay was neglected also in this case; therefore the first available echo (i.e. the second echo) was coming at about 20ms+3*5ms= 35ms. For the phantom acquisitions the behavior of the 2D-RF was very promising as shown in the following depicted decays:

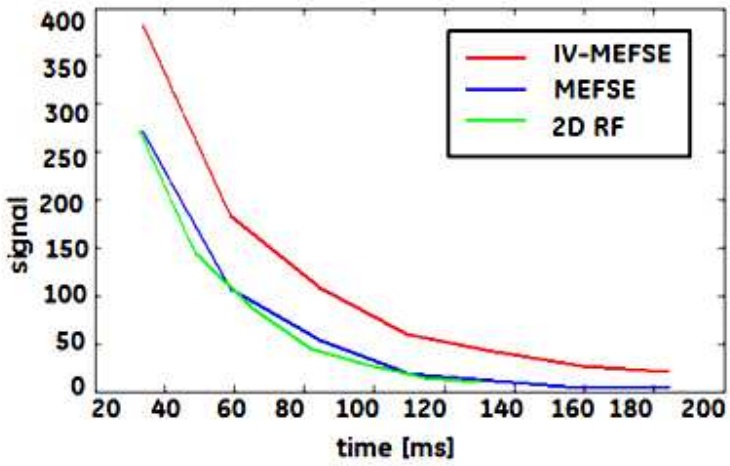

Fig. 39 *Decay curves obtained on a phantom with standard MEFSE, IV-MEFSE and with 2DRF-MEFSE. The T_2 decays are very similar in the case of MEFSE and 2DRF-MEFSE, with the same echo spacing. The decay acquired in the case of the IV-MEFSE is slower and has higher signal due to the more severe STEs contribution. For the IV-MEFSE the echo spacing is longer due to the longer excitation pulse.*

The decay in the case of the 2DRF-MEFSE was very similar to the decay acquired with standard MEFSE, even though the acquisition was starting much later (at about 40ms instead of 10ms).
The application of the 2DRF-MEFSE sequence on volunteer scans was not as successful as expected. Following an example of acquired T_2-map:

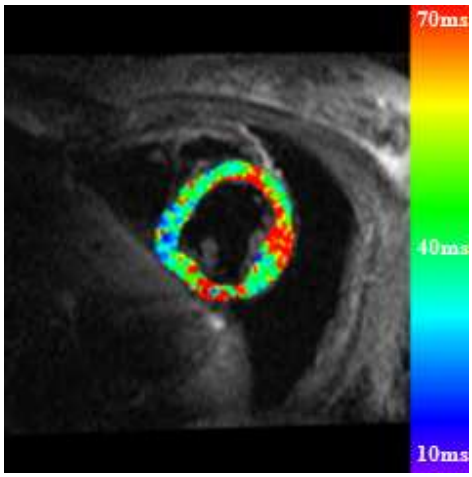

Fig. 40 *Example of T_2-map obtained with 2DRF-MEFSE.*

The reduce FOV excitation achieved with the 2D-RF was accomplished successfully with sharp edges and without wrapping. However, the T_2-map obtained using the 2D-RF excitation pulse was very inhomogeneous. The single acquired images had quite low SNR, which is probably the cause of the bad quality of the maps. Moreover some shading was observed in certain areas of the T_2-weighted images. This is due to the sensitivity of the 2D-RFs to off-resonance spins.
More tests need to be performed to optimize the use of 2D-RF pulses for T_2-mapping applications. The phantom studies showed promising results, but the *in vivo* tests need more refinement and parameter optimization in order to obtain good results and outperform the IV approach.

2.2.6. Conclusions on reduced-FOV T_2-mapping

A modified version of the MEFSE sequence was presented for generating T_2 maps of the heart. The IV-MEFSE was tested in phantoms and volunteers and was able to reduce the scan time from 23s to 15s, making the breath hold time more tolerable for the patient. Inner volume excitation does not have an aliasing concern, thus the scan prescription was much easier. IV led to the generation of more STEs, causing a 20% T_2 overestimation. Therefore the IV option should be used with caution in case of myocardial T_2 mapping.
The 2D-RF approach was explored as well, showing promising results on the phantom studies. In this case more tests and optimization need to be performed in order to obtain a good quality T_2-maps, capable of outperform the IV approach.

2.3. LUNG IMAGING

2.3.1. Introduction on lung imaging pulse sequence development

The human lung is a challenging target for structural MR imaging of its vessels and parenchyma. Generally, lung tissue is characterized by low proton density and associated low signal [100]. Rapid succession of air-tissue interfaces result in strong microscopic B_0 gradients and associated short signal lifetimes ($T_2^* \sim 0.5–3$ ms [101, 102]). Furthermore, the lungs are affected by respiratory and cardiac motion. If unaccounted, this leads to strong motion artifacts in the form

of ghosting and blurring dependent on the acquisition scheme. On the positive side, the dark background leads to good morphological contrast – assuming the challenging lung signals are well captured.

The current state of MR imaging of the lung was recently summarized in the following review articles [103 - 106]. There are four basic sequences that were identified to be effective for lung imaging, including: spoiled gradient echo [107], balanced steady state free precession (balanced-SSFP) [108, 109], fast spin echo [110] and ultra-short TE (UTE) [111, 112]. Derived MR protocols are generally optimized for short TE and high scan efficiency. The following figure shows some lung images obtained with some standard sequences at 1.5T and at 3T. The off-resonance effects make the lung imaging more challenging (i.e. more blurry images) at higher static magnetic field.

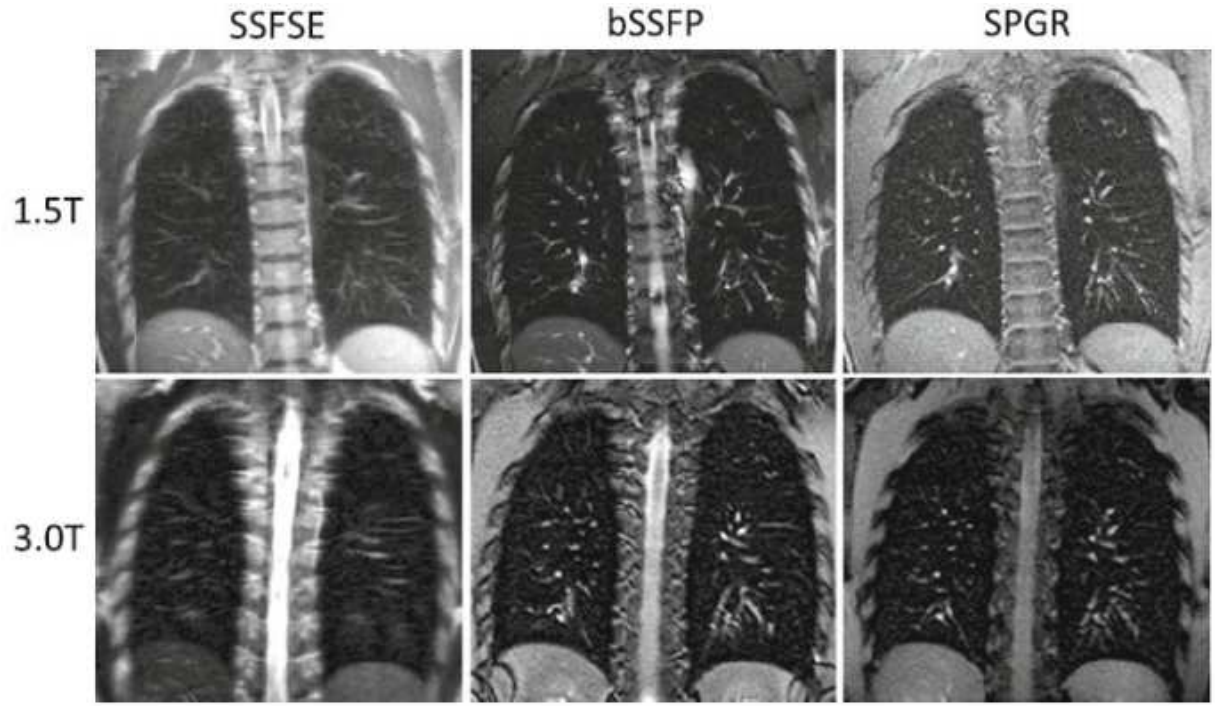

Fig. 41 *Lung images obtained using standard imaging sequences with low TE. From left to right: Single Shot Fast Spin Echo, balanced Steady State Free Precession, Spoiled Gradient Echo. [103]*

Functional studies of the lung are widespread as well [113 - 115]. Most of the techniques used for functional studies of the lung need to gain some contrast to be able to visualize the lung

perfusion. Contrast is often enhanced using hyperpolarized substances. Perfusion of the lung can be visualized with more standard contrast agents [116] or with pulsed arterial spin labeling [117]. In order to avoid motion artifacts, image data are acquired at a defined phase of the respiratory cycle; typically in the more prevalent end-expiratory phase. For this either the patient needs to adjust to the data acquisition (in form of breath holding), or vice versa the scanner prospectively adjusts to the free-breathing patient using respiratory triggering, or gating [118]. Alternatively, retrospective gating can also be applied by sorting data into different phases of the respiration cycle [119]. Independent of prospective or retrospective motion management, physiological signals are required that reflect the respiratory breathing state. Such signals are typically obtained using respiratory belts or navigators [120, 121].

First introduced in the 1990s, zero-TE pulse sequences – such as BLAST [122], RUFIS [123] and WASPI [124] – experienced a recent revival with associated refinements in the form of ZTE [125] and PETRA [126]. Zero TE imaging uses hard pulse excitation followed by 3D radial sampling to achieve isotropic and large field-of-view (FOV) coverage. With only minimal gradient ramping between spokes, the pulse sequence achieves a nominal TE of zero, is robust against gradient imperfections and is virtually silent. Using a high imaging bandwidth provides efficient sampling of short T_2 signals and also results in very fast scanning with TR ~ 1ms.

The zero-TE sequences are frequently used for the head imaging [127], for example for brain or also for the bones. With RUFIS it is possible to acquired nice 3D datasets with a PD contrast (or also T_1 or T_2 contrast in case an appropriate preparation pulse is applied). Interestingly the resulting images show details not visible with other standard imaging sequences, e.g. the bones or the coil elements. The following figure is a head RUFIS scan, in which it is possible to recognize the coil elements:

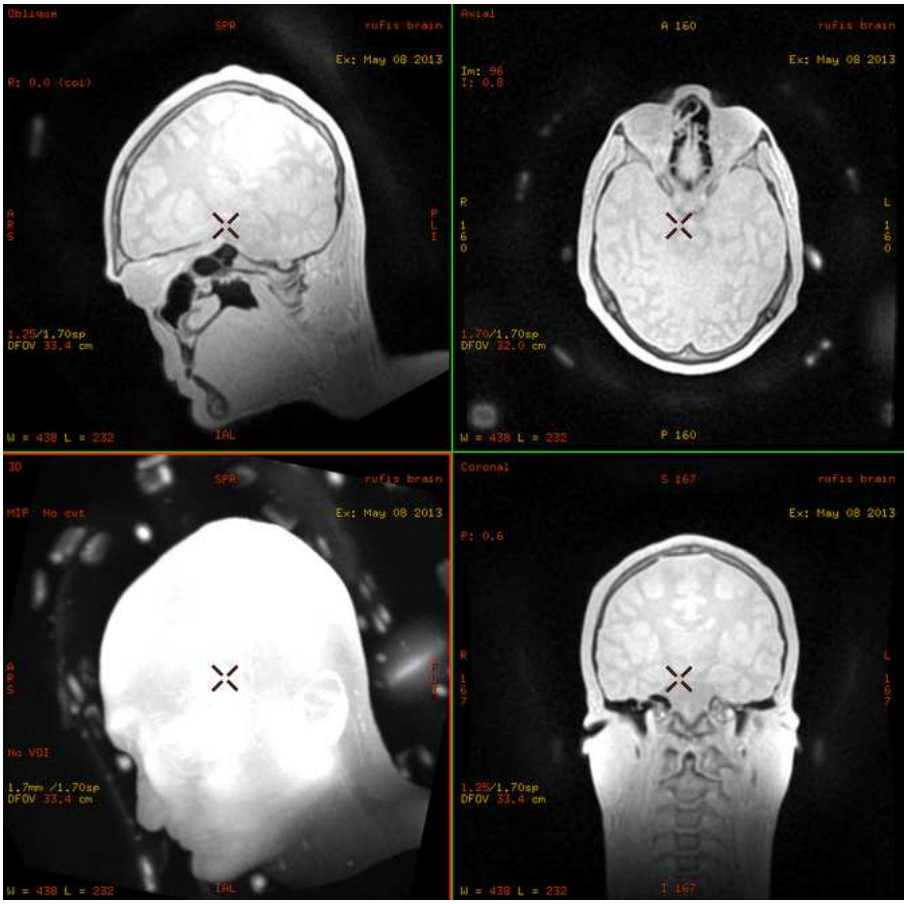

Fig. 42 *RUFIS imaging of my head at 3T. From the PD image it is possible to recognize the bones and the coil elements around the head, especially in the Maximum-Intensity-Projection render (bottom left).*

The RUFIS-type zero TE imaging was adapted and optimized for MRI of the lung. Prospective and retrospective respiratory motion management were implemented and compared relative to free breathing and breath holding. Breathing information was derived from either respiratory belts or navigator signals. For the latter, pencil beam and DC navigators were interleaved into the pulse sequence. The methods are demonstrated in volunteer studies.

2.3.2. Pulse Sequence

Zero TE imaging was implemented similarly to the RUFIS method [123]. This pulse sequence consists of a non-selective hard pulse excitation followed by 3D center-out radial sampling.

Unlike most MR pulse sequences, the readout gradients are not ramped down between repetitions. Accordingly, image encoding starts immediately at full speed (i.e. without requiring initial gradient ramping) and also leads to a nominal TE = 0, with the nominal TE defined as the center k-space echo time. The diagram of the pulse sequence is shown in the following figure:

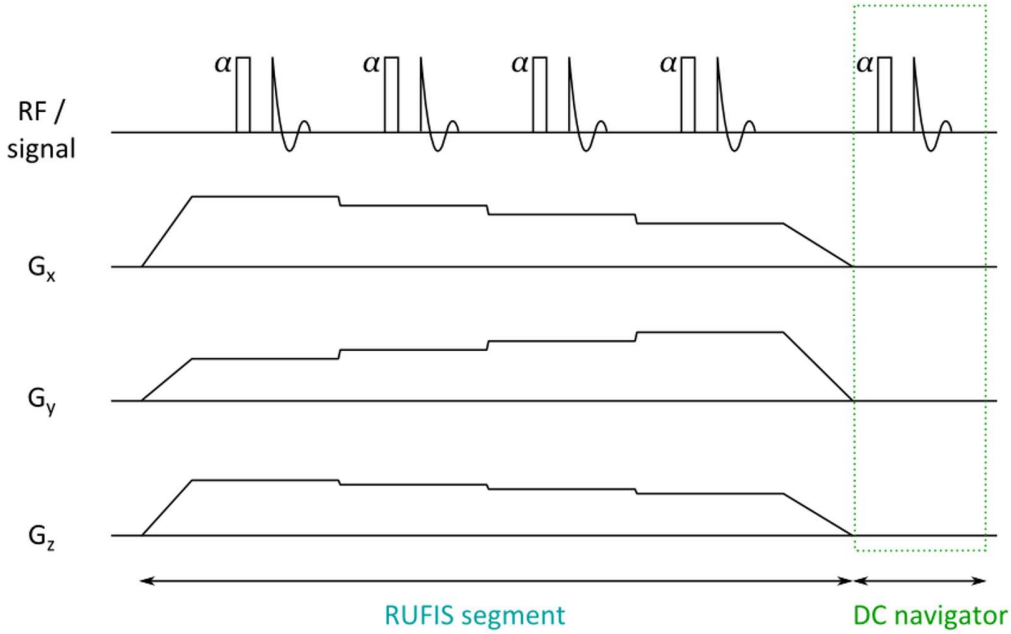

Fig. 43 *RUFIS sequence diagram. Figure shows one segment of the sequence, followed by the DC navigator acquisition. The DC navigator is present only for RG and is replaced by the pencil beam navigator module in the case of PG. α is the flip angle of the RF.*

The residual magnetization between consecutive excitations is canceled using both gradient and RF spoiling. The pulse sequence was grouped into segments, each containing a certain number of spokes. This grouping allows interleaving navigator modules (for real-time or retrospective motion correction), and preparation pulses (for contrast preparation or chemical shift selective saturation).

In order for the imaging gradients to not significantly disturb spin excitation, the excitation bandwidth (BW_{Tx}) needs to be wider than the imaging bandwidth (BW_{Rx}) [127, 129]. For typical B_1 amplitudes of clinical whole-body MR scanners (~15μT) this leads to flip angles of a few degrees maximum, resulting in native proton density type image contrast. Importantly, the minimal gradient ramping and short RF pulsing translates into very short TRs (~1ms range), high sampling efficiency and hence fast, SNR-efficient scanning.

The 3D radial spokes were uniformly distributed in all directions and sequentially ordered along a spiral path [130]. This limits the gradient switching between repetitions to incremental directional updates only, resulting in robustness to eddy currents and virtually silent scanning. For a certain FOV and a number of readout points (N_{RX}), the number of radial spokes corresponding to the exact Nyquist sampling at the k-space periphery is $4\pi(N_{RX})^2$. In order to keep the acquisition fast without significant aliasing artifacts, the number of spokes was chosen to be $4(N_{RX})^2$ and twofold oversampling was applied along the radial direction. The reconstruction was performed using a 3D version of the gridding method mentioned in the reconstruction section [12]. The following figure shows how the spokes are distributed on a low resolution trajectory:

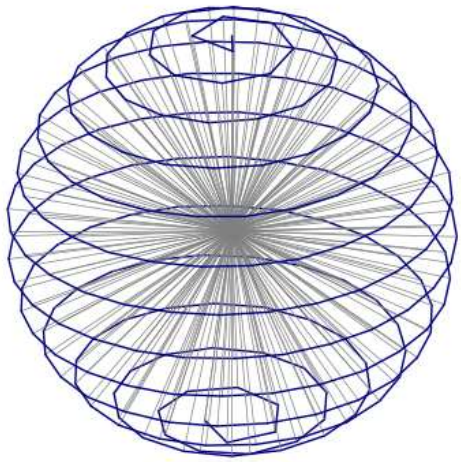

Fig. 44 *Under sampled 3D spiral trajectory used for low-resolution acquisition. Trajectory for high resolution data has a similar pattern. Trajectory (blue) with spokes (gray) distributed on it.*

In-vivo volunteer experiments and tests on phantom were conducted on a GE 3T MR750w scanner, equipped with a GEM Suite whole-body receive array (GE Healthcare, Waukesha, WI).

2.3.3. Motion management

Respiratory motion was addressed via i) prospective triggering (PT), ii) prospective gating (PG), iii) retrospective gating (RG) and compared to free-breathing (FB) and breath-hold (BH) examinations. Prospective triggering was implemented using the respiratory belt as triggering device. The triggering was adjusted to end-expiration by selecting appropriate trigger delay (~1s)

and acquisition duration for each subject. The acquisition duration per respiratory cycle was prescribed by the number of segments per trigger; with each segment containing a certain number of spokes. The following figure shows the acquisition scheme of the prospective triggering (left) and the respiratory belt (right).

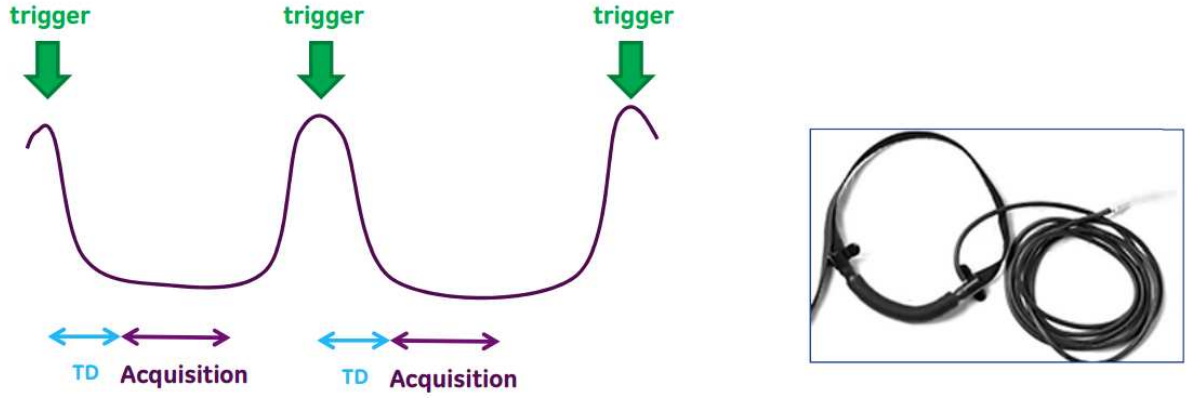

Fig. 45 *Acquisition scheme of the prospective triggering (left) driven by the respiration signal acquired by the respiratory belt (right). TD stands for trigger delay.*

Prospective gating was implemented based on respiration signals derived from a pencil beam navigator, which was interleaved in the sequence, and applied between every segment of spokes [118]. The pencil beam navigator was implemented in the form of a 2D selective spiral RF pulse followed by 1D readout along the excited pencil beam [131]. The gating decision was based on the selection of a gating level and window, which was automatically derived after a training period of a few respiratory cycles.

Retrospective gating was implemented based on center k-space DC navigator signals [132, 133]. Because the center k-space DC signals are intrinsically missed in zero TE with finite transmit-receive switching, a separate FID navigator module was interleaved into the sequence and applied between every segment of spokes. DC navigator signals were recorded together with the actual imaging and were used to retrospectively bin the individual spokes into different respiratory phases. In order to obtain sufficient statistics, several averages (N_{avg}) were applied and individually stored.

2.3.4. Data analysis

Image results were compared measuring SNR and blurriness in the anatomical structures. A region of interest (ROI) was manually selected in the liver and the SNR was evaluated as the ratio between mean and standard deviation of the signal in the ROI. The blurriness of the structures was evaluated using the metric described in [134], which is based on the observation that a low-pass filter has more effect on sharp images than on blurry images. The calculated blurring value measures the relative change in the overall gradient amplitude of the image before and after the low-pass filtering. A 4x4 moving average low-pass filter was used for this work. The effectiveness of motion management was evaluated measuring the sharpness of gray level transition at the boundary of the diaphragm. Deficient motion management mixes inconsistent respiratory phases in the reconstructed image resulting in enhanced blurring at the lung – diaphragm interface.

2.3.5. Results

Fig. 46 illustrates simulations of the acquisition time and point spread function of ZTE (solid lines) versus UTE (dashed lines) for different imaging bandwidths (color coded). The simulations were performed assuming certain gradient specifications (S_{max}=120mT/m, G_{max}=unconstrained), isotropic image encoding for a high nominal resolution of π/k_{max}=0.4mm, and negligible transmit-receive switching with data sampling starting immediately after RF excitation. Fig. 46a shows the acquisition time (T_{ACQ}) required for different imaging bandwidths. Higher BW_{Rx} requires longer ramping in case of UTE and correspondingly longer T_{ACQ} for UTE, due to higher readout gradients. Considering also the longer RF excitation pulses and additional ramping of the spoiler gradients characteristic for UTE, the actual speed advantage of ZTE gets even more pronounced. Fig. 46b illustrates the 1D profile of the 3D, rotationally-symmetric point-spread-function (PSF) of the ZTE sequence for different BW_{Rx}, assuming an effective T_2*=0.5ms characteristic for lung parenchyma [102]. Higher BW_{Rx} enables faster and hence more efficient and accurate signal capture of the fast decaying lung signals. Conversely, signal decay during lower BW_{Rx} acquisitions translates in a broadening of the PSF and associated image blurring. The intrinsically lower SNR efficiency at higher BW_{Rx} ($SNR \sim BW_{Rx}^{-1/2}$) can be compensated via averaging ($SNR \sim N_{avg}^{1/2}$); both effects are not accounted in the simulation. This tradeoff is especially advantageous for ZTE, which has a sampling efficiency close to 100%. It is

important to note that the maximum flip angle in ZTE is inversely proportional to the BW_{Rx}. This is illustrated in Fig. 46c showing the PSF multiplied by the flip angle, with the full-width-half-maximum (FWHM) quantified in the figure legend. Considering both the signal capture efficiency (PSF height) and depiction accuracy (PSF width) an imaging bandwidth of around ±62.5kHz appears optimal for ZTE imaging of the lung.

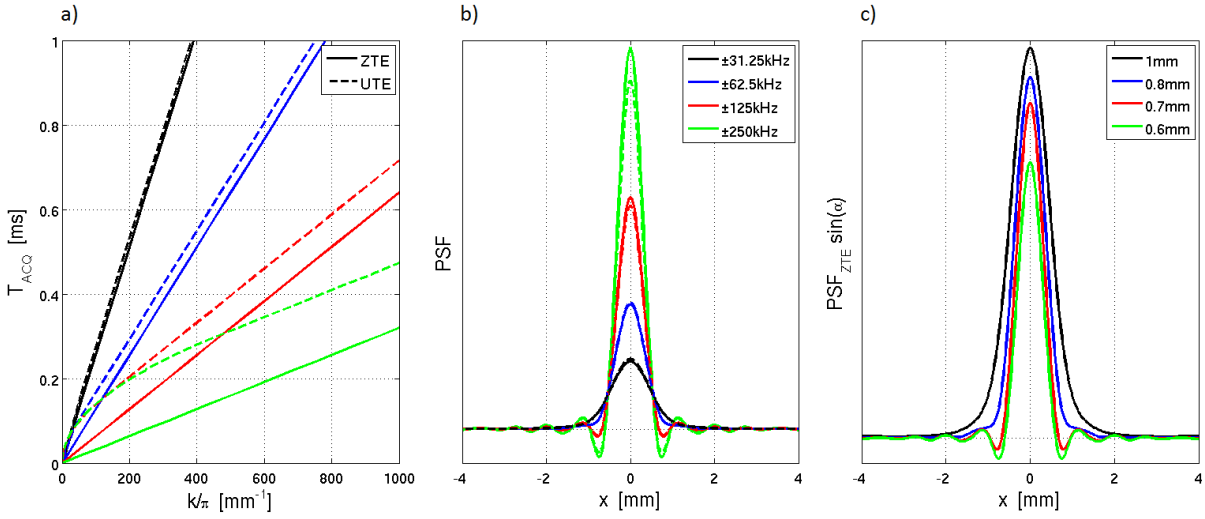

Fig. 46 *Simulation results for spatial resolution dependency over BW_{Rx}. (a) Due to gradient ramping, UTE needs longer scan time compared to ZTE in order to obtain the same resolution. (b) Faster signal decay at lower BW_{Rx} causes a broadening of the PSF and associated image blurring. (c) On the other hand, low BW_{Rx} increases the achievable SNR, as shown by the PSF normalized for the maximum flip angle (α) associated to the specific BW_{Rx}.*

Besides affecting SNR and resolution characteristics, the imaging bandwidth also impacts the contrast behavior. Fig. 47 shows a BW_{Rx} comparison for a volunteer using real-time prospective triggering. Higher BW_{Rx} with faster sampling reduces T_2*-induced blurring, improves image resolution, and decreases scan time, although at the cost of SNR. The longer signal readout at lower BW_{Rx} results in enhanced fat-water off-resonance contrast as can be seen in the borders between organs and fat/water tissues. Interestingly, the pulse sequence also captures plastic signal from the respiratory belt, the coils, and the table, which can be seen most clearly above and below the subject in the top row with BW_{Rx} = ±125 kHz. The scan parameters for these examinations, together with the SNR and blurriness metrics are listed in Tab. 5.

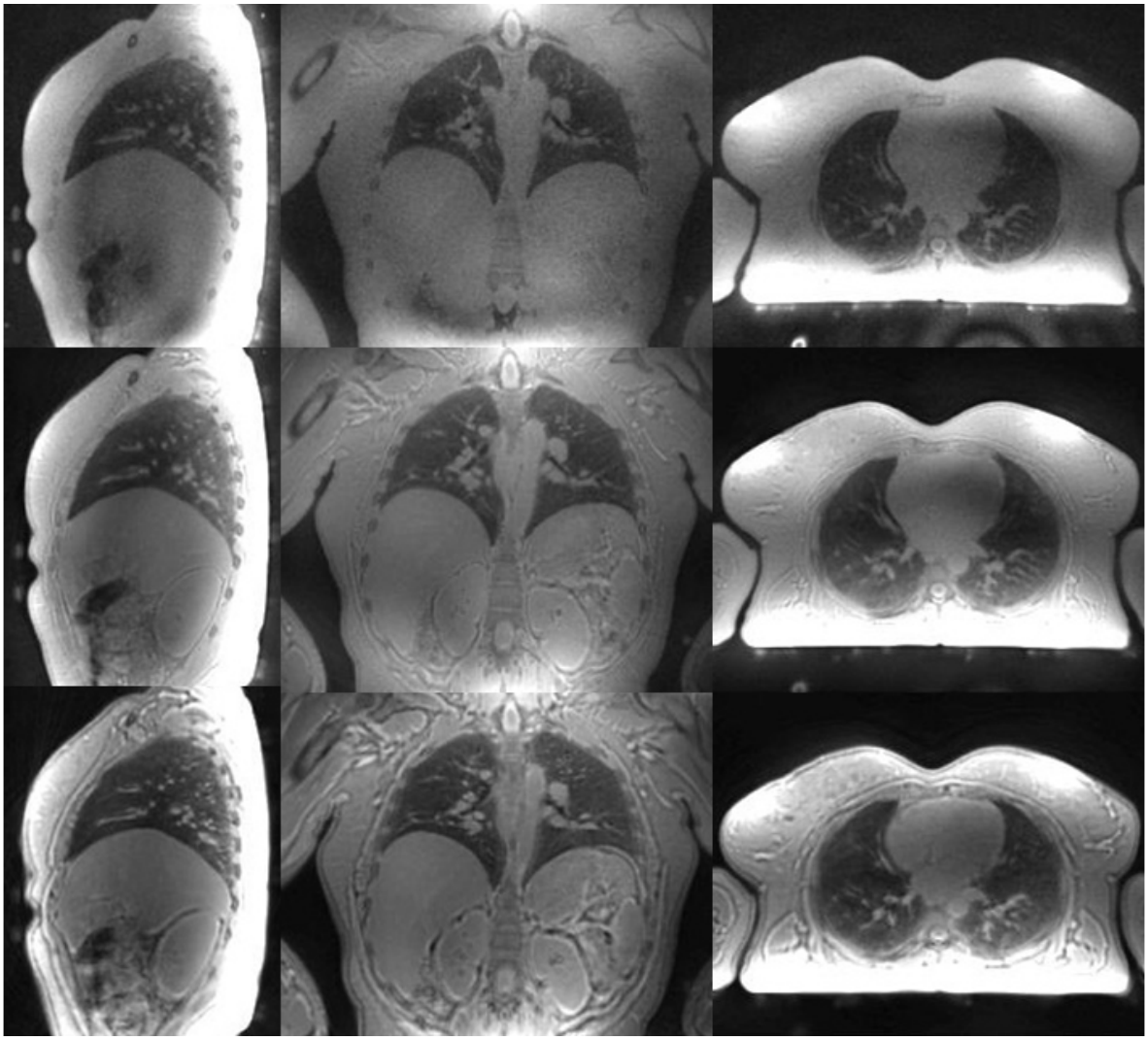

Fig. 47 *BW_{Rx} comparison on volunteer using the gated acquisition. Top row BW_{Rx} = ±125kHz; middle row BW_{Rx} =±62.5kHz, bottom row BW_{Rx} =±31.25kHz. From left to right: sagittal, coronal and axial slice. As the BW_{Rx} increases, the resolution improves, but the SNR decreases. In the images there is no intensity correction or gradient warping applied.*

BW_{Rx}	RF duration	FA	scan time	SNR	Blurriness
±125.0kHz	4μs	0.5°	7’ 03’’	24±5	0.4259
±62.5kHz	8μs	1°	12’ 39’’	33±5	0.4953
±31.25kHz	16μs	2°	25’ 35’’	41±5	0.5257

Tab. 5 *Scan parameters used for the BW_{Rx} comparison with PT on volunteer. The parameters FOV=48cm, pixel size=1.5mm, Navg=1 were kept the same for all acquisitions.*

The avoidance of the motion during acquisition was shown to produce a significant improvement on the image quality. The improvement was also preliminarily tested in phantom experiments moving the table in order to simulate the respiratory motion. Increasing the width of the acquisition window has a strong impact on the artifacts and the image blurring. Even if a wider acquisition window shortens the dead time in the scan, the artifacts are more pronounced.

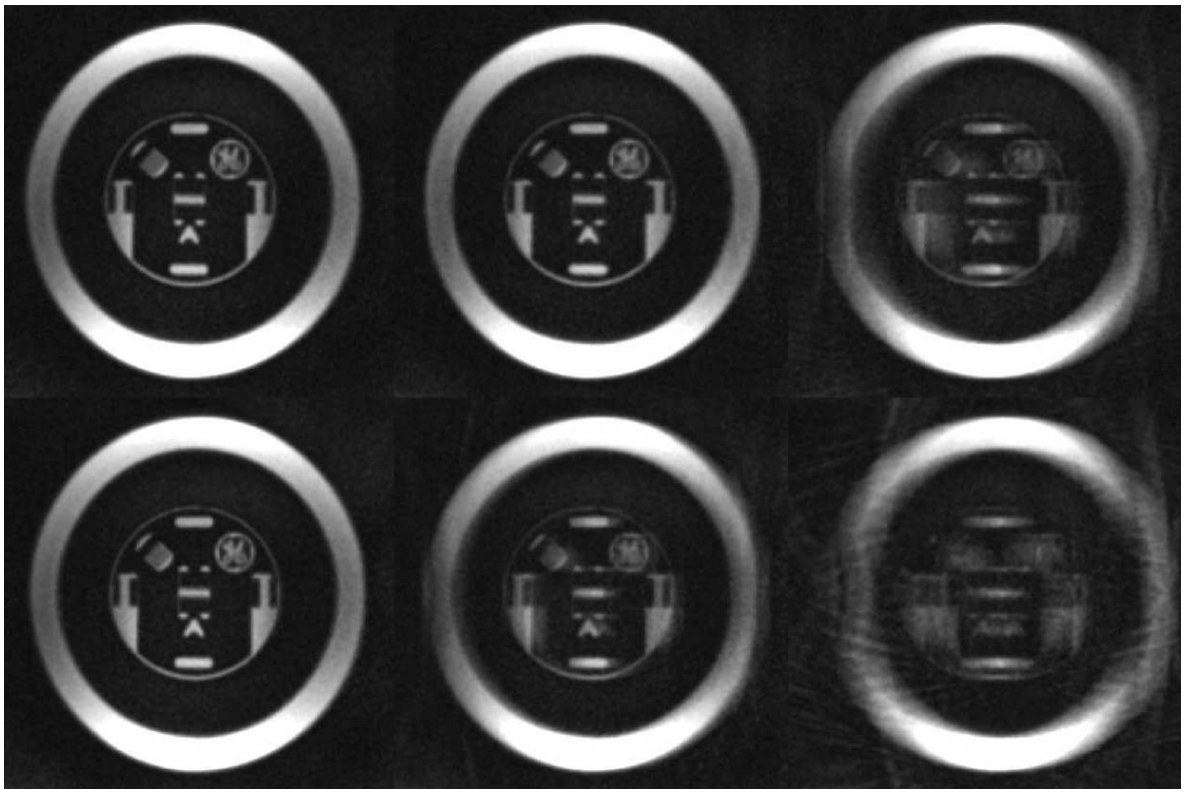

Fig. 48 *Phantom comparisons (sagittal slice) for different values of the acquisition window in the prospective triggering approach. Phantom motion was along S/I direction and had amplitude of 3cm and maximum velocity of 13mm/s. Top row: phantom not moving (left), 1400ms acquisition window (middle), 2800ms acquisition window (right). Bottom row: 700ms acquisition window (left), 2100ms acquisition window (middle), no gating (right).*

Fig. 49 compares lung images in end-expiration phase obtained with free breathing (FB), breath-hold (BH), prospective triggering (PT) and prospective gating (PG) examinations. Acquisition

parameters together with SNR and blurriness metrics are listed in Tab. 6. In the case of FB, motion artifact is visible but confined to the areas of significant motion, (i.e. the bottom of the lungs). In comparison, BH freezes respiratory motion, but achieves only limited spatial resolution and streaking due to a higher undersampling factor. Both PG and PT approaches were able to eliminate motion artifacts and obtain high-resolution and high SNR images in less than six minutes acquisition time.

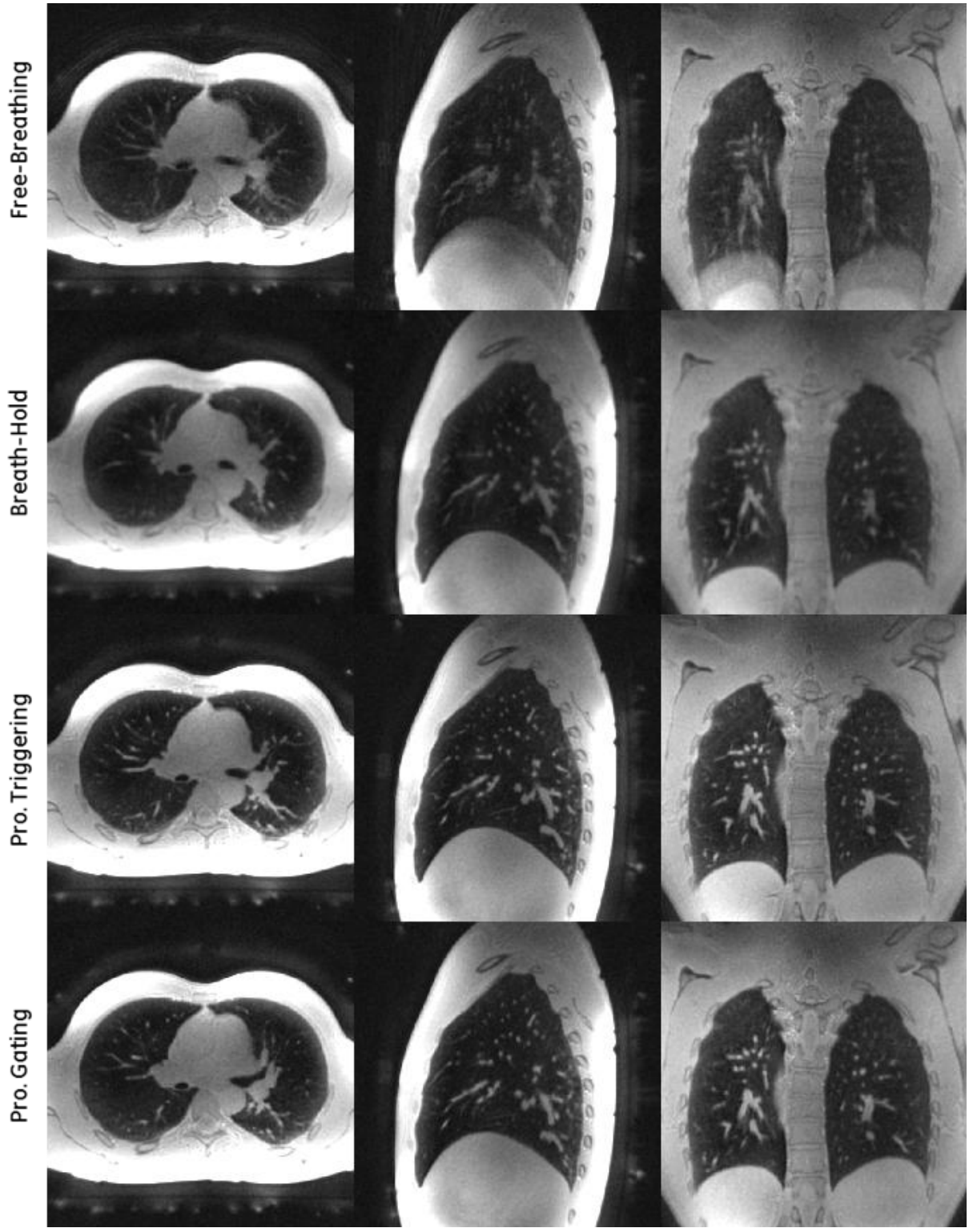

Fig. 49 *Axial (right column), sagittal (middle column) and coronal (left column) slices of isotropic 3D lung images. The free-breathing image (fist row) shows motion artifact, although*

reduced by the 3D-radial sampling. Breath-hold acquisition (second row) shows no motion artifact, but has limited image resolution and low SNR per pixel size. Both PT (third row) and PG (fourth row) acquisitions show no motion artifact with high image resolution and high SNR per pixel.

Method	scan time	FOV	pixel size	N_{avg}	SNR	diaphragm transition
PT	5’ 40’’	30cm	1.2mm	2	26±5	5±0.5mm
PG	5’ 30’’	30cm	1.2mm	2	27±5	5±0.5mm
RG	15’ 03’’	46cm	1.8mm	8	34±5	7±0.5mm
BH	31’’	30cm	1.8mm	1	29±5	8.5±0.5mm
FB	3’ 20’’	30cm	1.2mm	2	28±5	42.5±0.5mm

Tab. 6 *Scan parameters PG, RG, BH and FB examinations on volunteer. For all examinations we used BW_{Rx}=±62.5kHz, FA=1.2°, RF width 8 μs, oversampling factor=2. For lower resolution, partial volume effect makes the diaphragm transition appear wider.*

The lung images acquired are so well detailed that it is possible to distinguish the lung fissure as shown in the following figure:

Fig. 50 *Lung image acquired with the PT approach. The 1.2 resolution shows a detailed overview of the structures of the lung. The lung fissure is showed by the arrow.*

Fig. 51 shows an example of the signals acquired for lung motion detection. The belt signal (Fig. 51a) and the pencil beam navigator (Fig. 51b) were acquired during the same scan, showing good accordance and synchronism. Fig. 51c and d show the DC navigator signal and its histogram distribution, acquired over 8 repetitions. From the histogram it is possible to identify expiration and inspiration as the most prevalent motion phases.

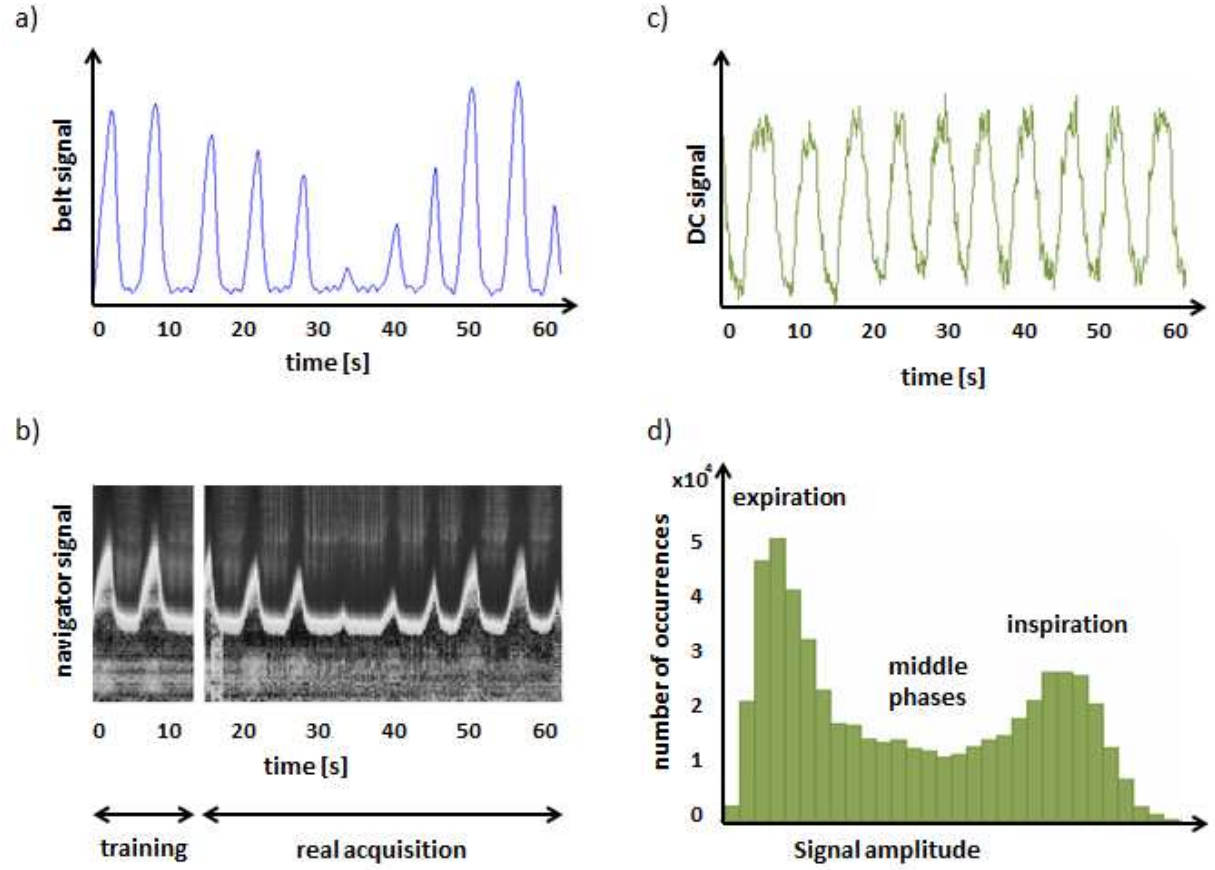

Fig. 51 *a) Respiratory belt signal over 60 sec acquisition. b) Pencil beam navigator signal synchronized with the belt signal in a). For the pencil beam navigator it is possible to distinguish a training phase from the real acquisition phase. c) DC navigator signal from a separate scan over 60 sec acquisition. d) Histogram of the navigator signal acquired over 840s (i.e. the single acquisition repeated 8 times).*

Fig. 52 illustrates high-resolution dataset with associated maximum-intensity-projection (MIP). The dataset was acquired with PT in ~9min scan time (FOV=280mm, pixel size=0.875mm,

BW=±62.5kHz, FA=1.2°, Navg=2). The MIP was performed over a slab thickness of 18.5mm and very clearly illustrates the lung vasculature.

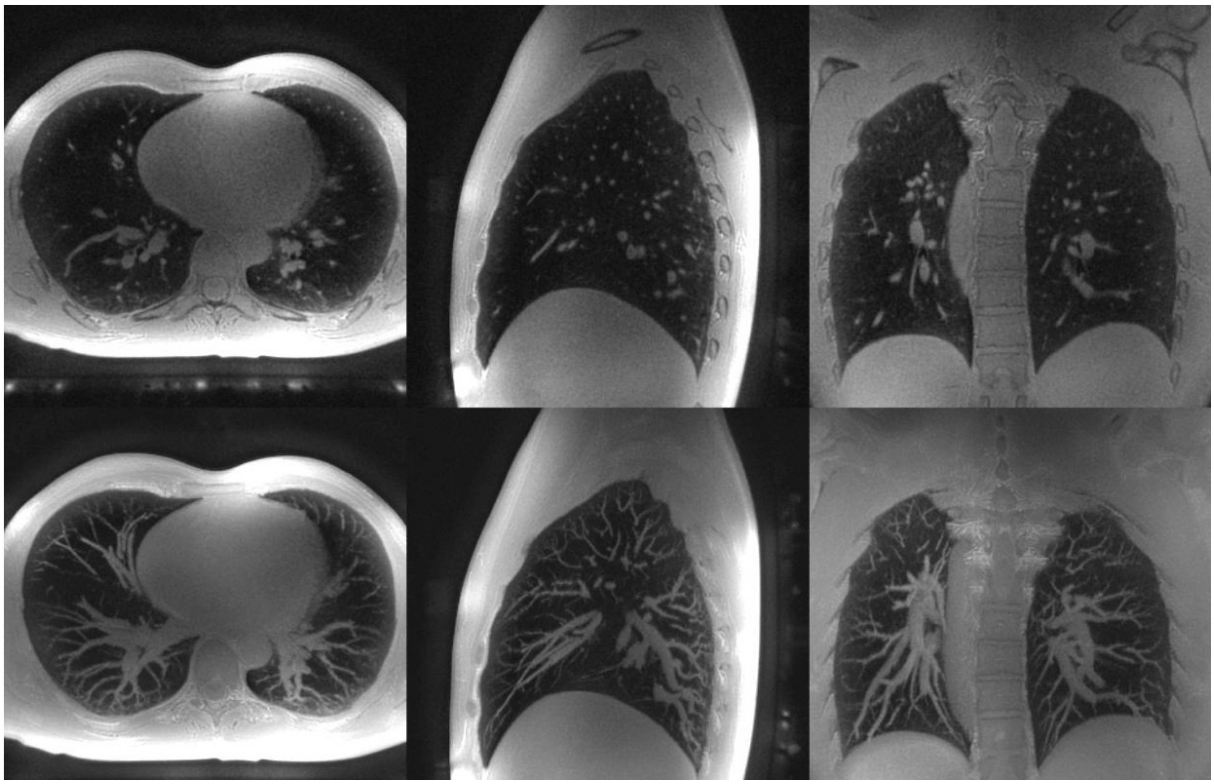

Fig. 52 *High resolution (0.875mm) PT dataset acquired over ~9min of scan. Filtered MIP (18.5mm slice thickness) is shown in the bottom row and depicts clearly even very small vessels.*

Retrospective data sorting allowed RG to reconstruct twelve phases of the respiration cycle. Four of the twelve phases are shown in Fig. 53. The motion artifact rejection in each phase depends on N_{avg}. As N_{avg} increases, each respiratory phase becomes better defined. For prevalent respiratory phases, data is collected faster, thus fewer repetitions are necessary for the reconstruction of an image clear of motion artifacts. For expiration (Phase 1), inspiration (Phase 12) and middle phases, the N_{avg} necessary to avoid motion artifact in the image is 4, 6 and 8, respectively.

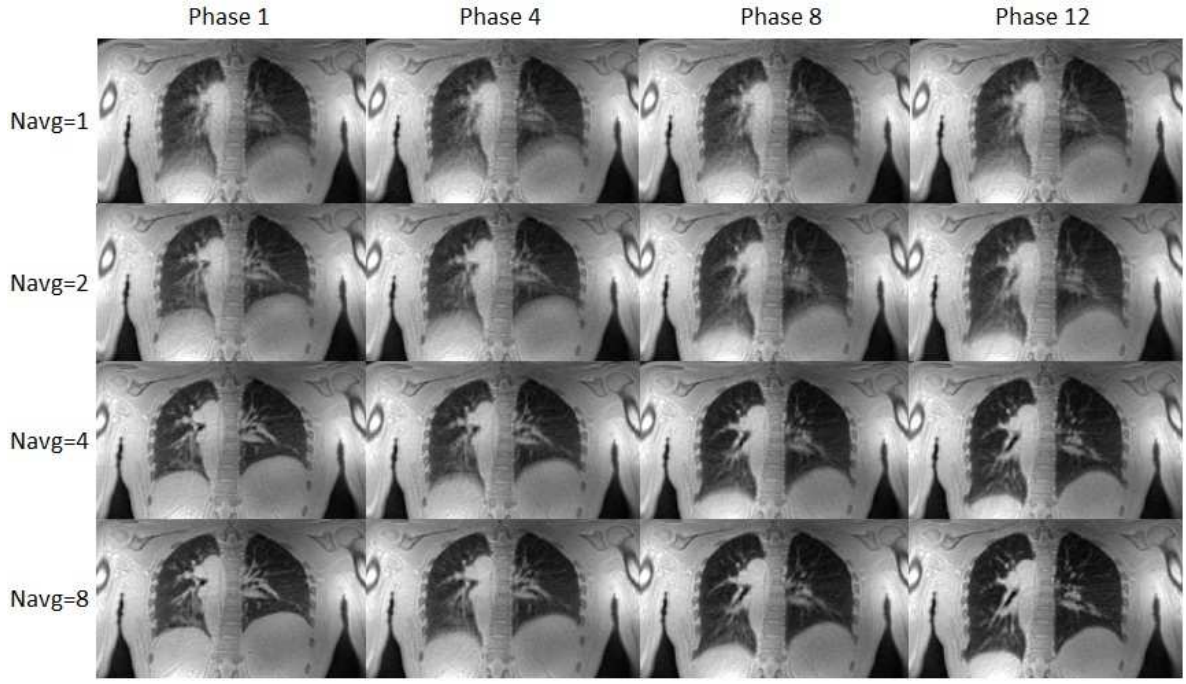

Fig. 53 *Coronal slices of 4 of the different phases reconstructed with RG. The influence of N_{avg} on the motion artifact can be observed. As N_{avg} increases, more data are collected thus the motion artifact is better rejected and the respiratory phases are better distinguished. For N_{avg}=1, respiratory phases are not distinguishable, thus the reconstruction produces a FB image in all cases. Phase 1: expiration; Phase 4 - Phase 8: middle phases; Phase 12: inspiration.*

2.3.6. **Discussion on RUFIS 3D lung imaging**

The zero-TE 3D RUFIS imaging is demonstrated to be suitable for structural whole lung imaging, with isotropic 1.2mm resolution acquired in a ~6min free-breathing scan. Compared to standard UTE methods, zero TE minimizes gradient ramping to only directional updates in between repetitions. The minimal gradient ramping practically eliminates eddy current effects and renders the pulse sequence virtually silent. Unlike UTE, the absence of eddy current effects allows the direct use of RUFIS without any previous calibration. Furthermore, a nominal echo time of zero in combination with high BW sampling enables accurate and efficient depiction of the short T_2^* lung structures in reasonable scan times. On the contrary, a high BW constrains the RF pulses width resulting in a maximum flip angle to a few degrees maximum and below the

Ernst angle. As a consequence, the images display a flat proton density contrast, which however clearly depicts the relevant lung morphology relative to the dark background.

The highest achievable resolution of this method was explored. The resolution limit results from a tradeoff between improving the imaging point spread function by increasing receive bandwidth, and decreasing SNR resulting from the limited achievable flip angle when exciting spins over wider frequency bandwidths. The blurring associated with a small receive BW is generated by both B_0 off-resonant spins and long acquisition window. Off-resonant spins are typically very common in the lung tissue, due to the several air-tissue interfaces. The long acquisition window allows the signal to decay while acquiring, thus contributing to blurring in the final image. Considering the tradeoffs between point-spread function, acquisition time, contrast behavior and SNR, an imaging bandwidth of ±62.5 kHz was found to be a good compromise.

In the acquired images it is possible to observe the coil elements used for the acquisition (following figure). This witnesses how RUFIS is suitable for the acquisition of the signal from very short T_2^* materials.

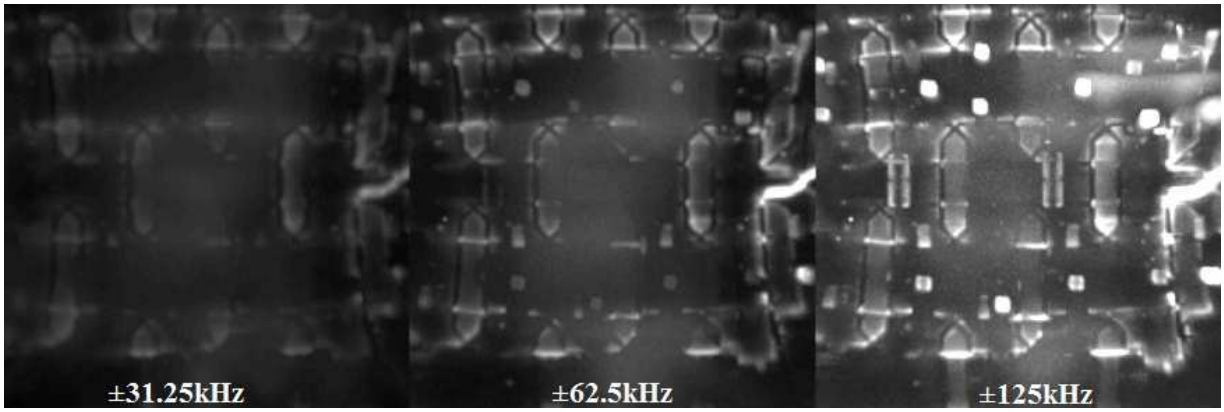

Fig. 54 *Table coil acquired with RUFIS at different receive bandwidth. For higher receive BW the acquisition is faster.*

This sequence is shown to be compatible with typically used methods of respiratory motion management, including respiratory belt triggering, a spatially selective pencil beam navigator, and a non-spatially selective DC navigator. The navigator acquisitions were interleaved between segments of radial spoke acquisitions, and did not introduce significant image artifacts or

increased scan time. Multiple time phases of a respiratory cycle were reconstructed from DC-navigated acquisitions. Twelve time phases could be reconstructed from as few as two full data acquisitions, although the image quality can be seen to improve with increasing data acquisition. A real time version of the multi-phase approach is currently being explored. The sequence is based on a pencil beam navigator acquired in real-time and routing the acquired data in a different memory location depending on the recognized respiratory phase.

In the presented results, no scan acceleration was applied beyond under-sampling by a factor of π, which is generally considered acceptable for 3D radial imaging. Higher acceleration factors and hence faster scanning would be enabled using parallel imaging, compressed sensing [135], or constrained reconstruction methods [136, 137]. In case of dynamic imaging also k-t principles [138] or GRICS-type methods [139, 140] could be applied. However, these methods are more computationally demanding, especially when applied in 3D and using non-Cartesian sampling.

Dedicated clinical studies are still needed in order to verify the utility and robustness of this method in patient populations and compare it relative to gold-standard CT. The obtained results are of particular interest for hybrid MR/PET imaging, where appropriate depiction of lung morphology is of key importance for oncology applications.

2.3.7. Conclusion about 3D RUFIS lung imaging

A 3D radial ZTE sequence was presented in this work for high resolution structural MR lung imaging. The combination of this imaging method with either prospective or retrospective gating was shown to be successful. The breathing motion also may be resolved into multiple time phases by retrospectively gating data using an interleaved DC navigator signal. The ZTE sequence is shown here to be more time efficient than UTE sequences. ZTE is also natively free from artifact arising from eddy currents thanks to the minimal gradient switching. The low flip angle, radial image acquisition can be interrupted by a variety of navigator or other signal preparations without introducing artifacts. Both prospective triggering and gating approaches were able to achieve 1.2mm spatial resolution in the clinically relevant acquisition time of around 5 minutes. Increasing resolution is found to be of limited benefit beyond 1mm due to SNR efficiency and T_2* decay constraints. The combination of good SNR, robustness to artifacts, and achievable resolution will likely make this a highly relevant clinical lung imaging sequence.

2.4. COMBINATION OF METHODS

2.4.1. RUFIS sequence applied to cardiac imaging

The RUFIS sequence was explored for cardiac imaging as well. For cardiac applications some T_1 or T_2 contrast needs to be produced in the images, otherwise the muscle will not be distinguishable from fat or blood. The T_1 preparation, the T_2 preparation and the fat suppression modules used for the head imaging were tested on the chest. Moreover a double triggering was implemented in the sequence. A first triggering was on the respiration signal and then a second one on the electrocardiogram. The double triggering had the purpose to synchronize the acquisition with the end-expiration respiratory phase and with the diastole phase of the cardiac cycle.

The obtained results showed that the preparation modules still need further improvement for the cardiac imaging in order to generate informative 3D cardiac images. The fat suppression module showed an image with some contrast on the heart (Fig. 55), but the image quality is not acceptable, comparing to the common 3D sequences used for cardiac imaging.

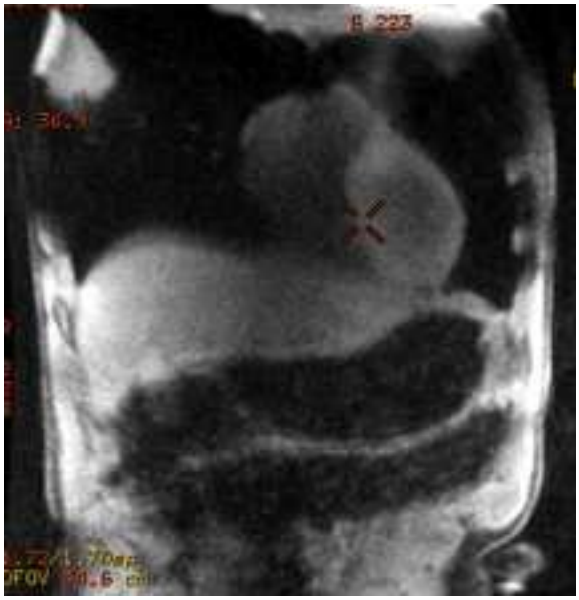

Fig. 55 *RUFIS image of the chest using a fat suppression preparation pulse. Some contrast is visible on the heart, but the image quality is not comparable to the common product sequences used for 3D imaging of the chest (e.g. the LAVA sequence [2]).*

2.4.2. Prospective triggering applied to cardiac T2 mapping

In the section about cardiac imaging a solution was shown to better fit the acquisition in the breath hold time. This could be useful for patients which can barely hold their breath for long. Alternatively the acquisition can be extended beyond the BH time using a prospective triggering as described above for lung imaging. This approach could be necessary in the cases of patients which can hardly hold their breath.

2.4.2.1. *Implementation*

A prospective triggering on the respiration signal was implemented in the T_2-mapping MEFSE sequence in order to extend the acquisition beyond the BH time. For comparison, free breathing (FB) examinations were acquired as well. The FB acquisition was performed with 1, 2 and 3 averages (N_{avg}) in order to reduce the motion artifacts in the images.
The prospective triggering approach was implemented similar to how described above for the RUFIS sequence. The triggering was double, first on the respiration signal, and then on the electrocardiogram within the acquisition window. *S*hort-axis cardiac images were acquired on 6 healthy volunteers at 3T (GE Healthcare, Waukesha, WI, USA). A six-segment model of the heart was considered to measure the average T_2 over the myocardium. The analysis of variance (ANOVA) was applied to estimate the presence of any significant difference among methods and among the segments of the heart for each method. A difference with p-value<0.01 was considered significant.

2.4.2.2. *Results and discussion*

Eight T_2-weighted images were acquired at 11ms TE increments. The scan parameters were: ETL =16, BW_{Rx}=±62.5 kHz, FOV=32, 192x128 matrix. The BH acquisition was performed on average in 24s scan time with N_{avg}=0.5. For both FB and PT multiple averages were tested. Fig. 56 shows the resulting maps obtained with the three methods. For the FB, a high N_{avg} was

necessary to reduce the motion artifacts, although the images appeared blurry. The PT approach avoided most of the motion artifacts already for N_{avg}=1, improving artifact rejection for higher N_{avg}. However the scan time associated with PT is much longer than FB (Fig. 56). According to the ANOVA-Bonferroni test, the BH approach did not show any significant difference with the PT approach for any value of N_{avg}. Conversely, the BH approach resulted to be significantly different from the FB approach for any value of N_{avg} (Tab. 7). Fig. 57 shows the six-segment model of the heart with associated average T_2 values. The ANOVA test resulted in segments significantly different in all cases. For both the BH and the PT approaches, the segments number 2 and 3 (i.e. the ones on the septum) showed a mean T_2 of 53.7ms, whereas the mean T_2 in the rest of the myocardium was 47.7ms. For the FB approach the presence of ghosting and blurring caused an increase of T_2 in segment 2 and 3 extended to segments 1 and 4 as well.

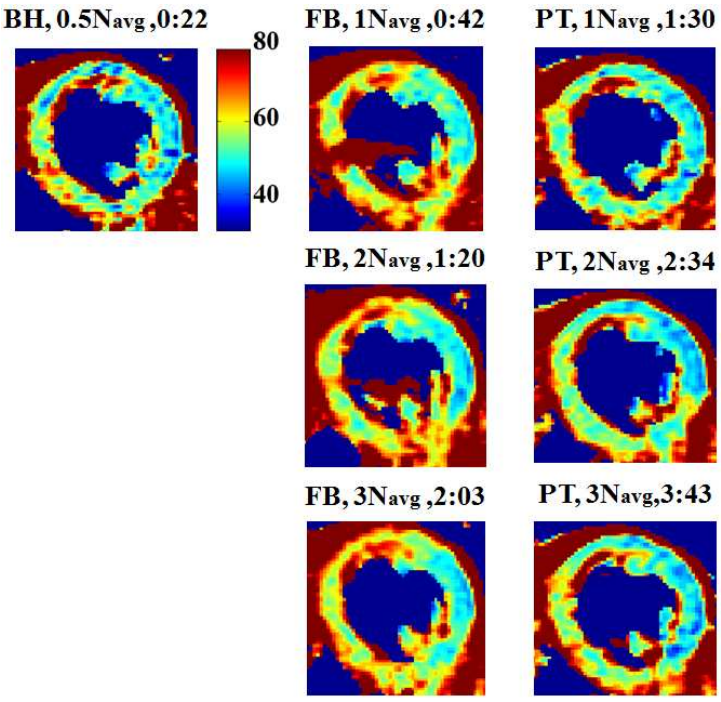

Fig. 56 *T_2 maps obtained in breath-hold (BH), in free-breathing (FB) and with prospective triggering (PT). On top of each image: the acquisition method, the number of averages (N_{avg}) and the average scan time. The same color map was used for all the images, thresholding the T_2 values between 30ms and 80ms.*

Comparisons	Mean Diff.	Std. Err.	p-value	95% CI
BH - FB_{1avg}	-8,441	1,265	<0,0001	-12,585 to -4,298
BH - FB_{2avg}	-7,355	1,163	<0,0001	-11,164 to -3,545
BH - $FB3_{avg}$	-5,998	1,193	0,0003	-9,906 to -2,091
BH - RT_{1avg}	-1,787	0,787	0,6178	-4,365 to 0,791
BH - RT_{2avg}	-1,449	0,668	0,7756	-3,638 to 0,739
BH - RT_{3avg}	-1,664	0,655	0,3273	-3,809 to 0,480

Tab. 7 *Results of the ANOVA-Bonferroni test. The BH exam is statistical equivalent to the RT, whereas it is significantly different from the FB.*

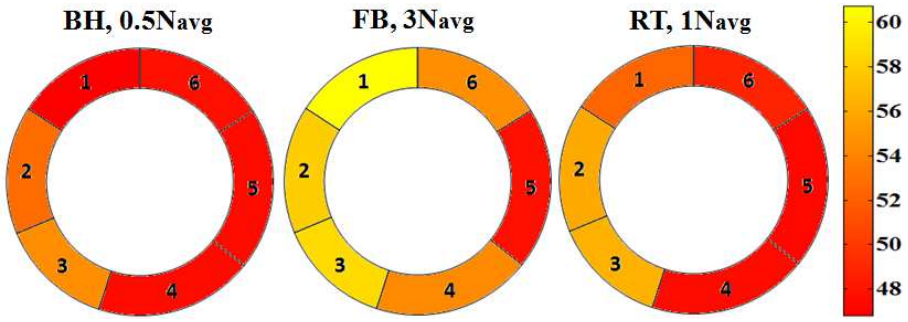

Fig. 57 *T_2 maps represented with the 6-segments model of the hear for the BH, the FB N_{avg}=3 and the RT with N_{avg}=1. The septum shows higher T_2 values than the rest of the myocardium for BH and RT. For FB the motion artifacts and the blurring generates inaccuracy in the maps.*

The MEFSE sequence was used to produce T_2-maps comparing the breath-hold approach with the respiratory triggering and the free breathing. The RT was shown to successfully produce T_2-maps statistically equivalent to the maps obtained with the BH approach. The acquisition in the PT approach was not limited to the breath-hold time, making the examination easier to prescribe and more comfortable for the patient. The FB approach showed non negligible motion artifacts which can be reduced only increasing the N_{avg}. However, the use of high N_{avg} with the FB approach produces blurry maps significantly different from the BH ones. For all methods a significant difference was found among the T_2 values of the segments. For both the BH and the RT approach, the T_2 values of the septum appeared 12.6% higher than in the rest of the myocardium. This is due to the fact that the septum is the area of the myocardium mostly protected from artifacts. For the FB approach the T_2 values of the segments were mixed because of the ghosting and the blurring, showing a higher T_2 value for the segments immediately outside of the septum as well.

CONCLUSION

In this work of thesis, the topic of MRI has been analysed in two of its main aspects: reconstruction and pulse sequence development. Both reconstruction and pulse sequence topics were related to the common thread of the avoidance of motion artifacts in the acquisitions. These topics are concrete problems in case of lung and cardiac imaging. Motion artifacts can be avoided synchronizing the acquisition with a specific phase of the motion. This is what is done in several cardiac applications. Regarding respiratory motion, it is possible to either make the acquisition fast and squeeze it in the breath-hold, or manage the motion in free breathing.

Non-Cartesian acquisition schemes are generally capable of providing a fast scans. The LS-NUFFT reconstruction method was mainly considered and compared to the gridding (GR) taking the direct summation method (DS) as reference.

In the first place a metric to recognize and measure the loss in geometric information was introduced using the 2D autocorrelation. According to this metric, the LS-NUFFT method resulted to have an error image more structured, comparing to the GR method.

Three regularization techniques (TSVD, TR and L1R) were applied to the LS-NUFFT in order to improve its performance in terms of reconstruction error. All methods kept the RMSE low for big interpolator sizes, comparing to the regularization-free approach. The TSVD method was the only one able to outperform the regularization-free reconstruction for a low size of the interpolator. The TR method resulted to be the fasted to be calculated.

Regarding the pulse sequence development, the attention has been focused on the thorax where the heart and the lungs are the main macroscopic sources of motion.

For cardiac imaging, FOV reduction methods were explored in order to better fit the acquisition in the breath-hold. The inner volume (IV) selection allowed the selection of sharp edges in the FOV avoiding aliasing. The IV excitation provided a scan time reduction from about 23s to 15s. The RF pulse imperfections produced undesired stimulated echoes (STE), causing an overestimation in the T_2 of about 20%. The use of 2D-RF pulses as an alternative to the IV approach appeared to be promising in order to obtain more accurate T_2 decays.

Regarding lung imaging, the acquisition was extended beyond the breath-hold in free breathing, addressing respiratory motion with prospective triggering (PT), prospective gating (PG) and

retrospective gating (RG). The RUFIS sequence was demonstrated to be suitable for the imaging of the lung tissue. The best compromise between SNR and spatial resolution was achieved with the receive bandwidth of ±62.5 kHz. All motion management methods were able to reconstruct a 3D high-resolution dataset with PD contrast weighting. Both PG and RG could achieve 1.2 mm isotropic resolution in clinically reasonable scan time (~6min). The RG sequence could reconstruct multiple phases of the respiration cycle at cost of higher scan time.

AKNOWLEDMENTS

I would like to express my greatest gratitude to the people who have helped and supported me throughout the whole period of my PhD. I am very grateful to professor Landini for his continuous support for the all the projects I have been working on, and for all the advice and encouragement he gave me to this day.

I would also like to thank prof. Santarelli and prof. Positano for all the advice throughout the all period of the study and the help in completing the research tasks especially about the MR reconstruction topic. Thanks to the whole engineering and medical team of FTGM in Pisa and especially to Dr. Lombardi for giving me the opportunity to work in the MR laboratory in Pisa and putting me in contact with GE Global Research in Munich.

Great thanks go to the whole GE team in Munich for all the help, the teaching the opportunities they gave me. I am very grateful to Dr. Schirmer for advising me and giving me the opportunity to work in GE and living a wonderful period of my life. Special thanks go to Dr. Wiesinger and Dr. Sacolick for allowing me to work on lung imaging and always coming up with new ideas and several inspiring suggestions to create something innovative and interesting. Thanks to Dr. Janich, Dr. Lechner and Dr. Kudielka for helping me out on the cardiac project and assisting me in the many difficulties I had to face during my period of study. Of course big thanks go to all the students as well, which made the experience in Munich unforgettable: Jonathan, Nicolas, Concetta, Renato, Tim, Vladimir, Anne and all the others. Thanks to Luisa, for giving support during my period abroad in Germany.

Thanks to all my friends which always believed in me: Davide, Rosario, Matteo and all the others always at my side. At last but not least, I wish to thank my parents for their undivided support and interest who inspired me and encouraged me to go my own way.

REFERENCES

1. Bernstein MA, King KF, Zhou XJ. Handbook of MRI Pulse Sequences. Elsevier Academic Press. 2004.

2. McRobbie DW, Moore EA, Graves MJ, Prince MR. MRI from Picture to Proton. Cambridge University Press. 2007.

3. Hu S, Lustig M, Chen AP, Crane J, Kerr J, Kelley DA, Hurd R, Kurhanewicz J, Nelson SJ, Pauly JM, Vigneron DB. Compressed sensing for resolution enhancement of hyperpolarized 13C flyback 3D-MRSI. J. Magn. Reson. 2008;192(2):258-64.

4. Lustig M, Donoho D, Pauly JM. Sparse MRI: The application of compressed sensing for rapid MR imaging. Magn. Reson. Med. 2007;58(6):1182-95.

5. Pruessmann KP, Weiger M, Scheidegger MB, Boesiger P. SENSE: sensitivity encoding for fast MRI. Magn. Reson. Med. 1999;42(5):952-62.

6. Griswold MA, Jakob PM, Heidemann RM, Nittka M, Jellus V, Wang J, Kiefer B, Haase A. Generalized autocalibrating partially parallel acquisitions (GRAPPA). Magn. Reson. Med. 2002;47(6):1202-10.

7. Lau AZ, Chen AP, Ghugre NR, Ramanan V, Lam WW, Connelly KA, Wright GA, Cunningham CH. Rapid Multislice Imaging of Hyperpolarized 13C Pyruvate and Bicarbonate in the heart. Magn. Res. Med. 2010;64(5):1323–1331.

8. Turnes CK, Romberg J. Spiral FFT: An Efficient Method For 3-D FFTs On Spiral Mri Contours. Proceedings of 2010 IEEE 17th International Conference on Image Processing.

9. Massone AM, Emslie AG, Hurford GJ, Prato M, Kontar EP, Piana M. Hard x-ray imaging of solar flares using interpolated visibilities. The Astrophysical Journal. 2009; 703: 2004–2016.

10. Mueller RK, Kaveh M, Wade G. Reconstructive tomography and applications to ultrasonics. Proc. IEEE. 1979; 67: 567–587.

11. King KF, Moran PR. A unified description of NMR imaging, data collection strategies and reconstruction. Magn. Reson. Med. 1984; 11: 1–14.

12. Jackson JI, Meyer CH, Nishimura DG, Macovski A. Selection of a convolution function for Fourier inversion using gridding. IEEE Trans. Med. Imag. 1991; 10: 473–478.

13. Rosenfeld D. An optimal and efficient new gridding algorithm using singular value decomposition. Magnetic Resonance in Medicine 1998; 40: 14–23.

14. Sedarat H, Nishimura DG. On the Optimality of the Gridding Reconstruction Algorithm, IEEE Transactions On Medical Imaging 2000; 19: no.4.

15. Kashyapa S, Yanga Z, Jacob M; Non-Iterative Regularized Reconstruction Algorithm for Non-CartesiAn MRI: NIRVANA. Magnetic Resonance Imaging. 2011; 29 : 222–229.

16. Hoge RD, Kwan RKS, Pike GB. Density Compensation Functions for Spiral MRI. Magnetic Resonance in Medicine. 1996; 38: 117–128.

17. Sarty GE. Natural k-Plane Coordinate Reconstruction Method for Magnetic Resonance Imaging: Mathematical Foundations. International Journal of Imaging Systems and Technology. 1997; 8: 519–528.

18. Pipe JG, Menon P. Sampling Density Compensation in MRI: Rationale and an Iterative Numerical Solution. Magn. Reson. Med. 1999;41: 179–186.

19. O'Sullivan JD. A Fast Sinc Function Gridding Algorithm for Fourier Inversion in Computer Tomography. IEEE Trans. Med. Imag. 1985;4(4):200-207.

20. Beatty PJ, Nishimura DG, Pauly JM. Rapid gridding reconstruction with a minimal oversampling ratio. IEEE Trans. Med. Imag. 2005;24:799-808.

21. Nguyen N, Liu QH. The Regular Fourier Matrices And Nonuniform Fast Fourier Transforms. SIAM j. Sci. Comput. 1999; 21, No. 1: 283–293.

22. Fessler JA, Sutton BP. Nonuniform Fast Fourier Transforms Using Min-Max Interpolation. IEEE Transactions On Signal Processing. 2003; 51: no. 2.

23. Sha L, Guo H, Song AW. An Improved Gridding Method For Spiral MRI Using Nonuniform Fast Fourier Transform. Journal of Magnetic Resonance. 2003; 162: 250–258.

24. Gibiino F, Positano V, Landini L, Santarelli MF. Regularization techniques on non-uniform Fast Fourier Transform. Int. J. Num. Meth. Biom. Eng. 2013;29(5):561-73.

25. Dutt A, Rokhlin V. Fast Fourier Transforms for Nonequispaced Data. SIAM j. Sci. Comput. 1993; Vol. 14, no.6: 1368–1393.
26. Dakua SP, Sahambi JS. Modified active contour model and RandomWalk approach for left ventricular cardiac MR image segmentation. Int. J. Numer. Meth. Biomed. Engng. 2011; 27:1350–1361.
27. Singh M, Mandal M, Basu A. Gaussian and Laplacian of Gaussian weighting functions for robust feature based tracking. Pattern Recognition Letters (2005); 26:1995–2005.
28. Kolybasova V, Krutitskii P, Prozorov K and Vainikko G. Numerical treatment of the Cauchy integral equation by discrete Fourier transform. Int. J. Numer. Meth. Biomed. Engng., 2011; 27: 1096–1106.
29. Chen KF and Mei SL. Accelerations of Zhao's methods for the numerical inversion of Laplace transform. Int. J. Numer. Meth. Biomed. Engng., 2011; 27: 273–282.
30. Sarty GE, Bennett R, Cox RW. Direct Reconstruction of Non-Cartesian k-space Data Using a Nonuniform Fast Fourier Transform. Magnetic Resonance in Medicine 2001; 45: 908–915.
31. Rasche V, Proksa R, Sinkus R, Börnert P, Eggers H. Resampling of Data Between Arbitrary Grids Using Convolution Interpolation. IEEE Trans. Med. Imag. 1999;18(5):385-392.
32. Moratal D, Lluch AV, Bodí V, Brummer ME. Magnetic Resonance Imaging Gridding Reconstruction Methods With and Without Density Compensation Functions. IEEE latin america transactions. 2011;9(1):774-778.
33. Pratt WK. Digital Image Processing: PISK Inside. John Wiley & Sons, Inc. New York, USA. 2001;Chapter 16.6:555-577.
34. Srinivasan GN, Shobha G., Statistical Texture Analysis. Proceedings of world academy of science, engineering and technology. 2008;2070-3740.
35. Haralick RM, Watson L. A facet model for image data. Comput. Vision Graphics Image Process. 1981;15:113–129.
36. Rubin DM. A Simple Autocorrelation Algorithm for Determining Grain Size from Digital Images of Sediment. Journal of Sedimentary Research. 2004;74(1):160-165.

37. Henry P, Adriany G, Deelchand D, Gruetter R, Marjanska M, Oz G, Seaquist ER, Shestov A, Ugurbil K. In vivo 13C NMR spectroscopy and metabolic modelling in the brain: a practical perspective. Magn. Res. Imaging. 2006;24:527–539.
38. Neurohr KJ, Barrett EJ, Shulman RG. In vivo carbon-13 nuclear magnetic resonance studies of heart metabolism, Proc. Natl. Acad. Sci. USA, 1983, 80: pp. 1603–1607.
39. Ardenkjaer-Larsen JH, Fridlund B, Gram A, Hansson G, Hansson L, Lerche MH, Servin R, Thaning M, Golman K. Increase in signal-to-noise ratio of >10,000 times in liquid-state NMR. Proc. Natl. Acad. Sci. USA. 2003;100(18):10158–10163.
40. Golman K, in't Zandt R, Thaning M. Real-time metabolic imaging. Proc. Natl. Acad. Sci. USA. 2006;103:11270–11275.
41. Menichetti L, Frijia F, Flori A, Wiesinger F, Lionetti V, Giovannetti G, Aquaro GD, Recchia FA, Ardenkjaer-Larsen JH, Santarelli MF, Lombardi M. Assessment of real-time myocardial uptake and enzymatic conversion of hyperpolarized [1-13C]pyruvate in pigs with slice selective Magnetic Resonance Spectroscopy. Contrast Media Mol Imaging. 2012;7(1):85-94.
42. Aquaro GD, Frijia F, Positano V, Menichetti L, Santarelli MF, Ardenkjaer-Larsen JH, Wiesinger F, Lionetti V, Romano SL, Bianchi G, Neglia D, Giovannetti G, Schulte RF, Recchia FA, Landini L, Lombardi M. 3D CMR Mapping of Metabolism by Hyperpolarized 13C-Pyruvate in Ischemia-Reperfusion. JACC Cardiovasc Imaging. 2013;6(6):743-4.
43. Cunningham CH, Chen AP, Lustig M, Hargreaves BA, Lupo J, Xu D, Kurhanewicz J, Hurd RE, Pauly JM, Nelson SJ, Vigneron B. Pulse sequence for dynamic volumetric imaging of hyperpolarized metabolic products. J. Magn. Res. 2008;193:139-146.
44. Theiler J, Eubank S, Longtin A, Galdrikian B. Testing for nonlinearity in time series: the method of surrogate data. Physica D. 1992;58:77–94.
45. Sussman MS, Stainsby JA, Robert N, Merchant N, Wright GA. Variable-Density Adaptive Imaging for High-Resolution Coronary Artery MRI. Magn. Reson. Med. 2002;48:753–764.
46. Pipe JC. Reconstructing MR images from undersampled data: data-weighting considerations. Magn Reson Med. 2000;43(6):867-75.

47. Brodsky EK, Holmes JH, Yu H, Reeder SB. Generalized k-Space Decomposition with Chemical Shift Correction for Non-Cartesian Water-Fat Imaging, Magnetic Resonance in Medicine. 2008;59:1151–1164.
48. Wiesinger F, Weidl E, Menzel MI, Janich MA, Khegai O, Glaser SJ, Haase A, Schwaiger M, Schulte RF. IDEAL Spiral CSI for Dynamic Metabolic MR Imaging of Hyperpolarized [1-^{13}C]Pyruvate. Magn. Reson. Med. 2012; 68: 8–16.
49. Gibiino F, Positano V, Giovannetti G, Frijia F, Menichetti L, Ardenkjaer-Larsen JH, Wiesinger F, Schulte R, De Marchi D, Lionetti V, Aquaro G, Lombardi M, Landini L, Santarelli MF. Reconstruction methods from hyperpolarized 13C chemical shift imaging spiral 3D data: Comparison between direct summation and gridding method. ISBI proceeding. 2012;614-617.
50. Hansen PC. Rank-Deficient and Discrete Ill-Posed Problems, Numerical aspect of linear inversion. SIAM Monograph on Mathematical Modeling and Computation. 1998.
51. Boyd SP, Vandenberghe L. Convex Optimization. Cambridge University Press. 2004. Material available at www.stanford.edu/.boyd.
52. Schmidt M. Least Squares Optimization with L1-Norm Regularization. CS542B Project Report. 2005.
53. Meyer C, Hu B, Nishimura D, Macovski A. Fast spiral coronary artery imaging, Magn. Reson. 1992; 28: 202–213.
54. Sussman MS, Stainsby JA, Robert N, Merchant N, Wright GA. Variable-Density Adaptive Imaging for High-Resolution Coronary Artery MRI, Magnetic Resonance in Medicine. 2002; 48: pp. 753–764.
55. Golub GH, Heath M, Wahba G. Generalized Cross-Validation as a Method for Choosing a Good Ridge Parameter. Tecnometrics. 1979; vol. 21, no. 2.
56. Pan M-s, Tang J-t, Rong Q-s, Zhang F. Medical image registration using modified iterative closest points. Int. J. Numer. Meth. Biomed. Engng. 2011 27: 1150–1166.
57. Oliveira FPM, Tavares JMRS. Registration of plantar pressure images. Int. J. Numer. Meth. Biomed. Engng. (2012), 28: 589–603.
58. Sun Y, Zhou YC, Li SG, Wei GW. A windowed Fourier pseudospectral method for hyperbolic conservation law. Journal of Computational Physisc. 2006; 214: pp. 446-490.

59. Wang Y, Wei GW, Yang S. Partial differential equation transform—Variational formulation and Fourier analysis. Int. J. Numer. Meth. Biomed. Engng. 2011; 27: 1996–2020.
60. Zheng Q, Yang S, Wei GW. Biomolecular surface construction by PDE transform. Int. J. Numer. Meth. Biomed. Engng. 2012; 28: 291–316.
61. Higgins CB, Herfkens R, Lipton MJ, Sievers R, Sheldon P, Kaufman L, Crooks LE. Nuclear magnetic resonance imaging of acute myocardial infarction in dogs: alterations in magnetic relaxation times. Am J Cardiol. 1983; 52:184–188.
62. Ratner AV, Okada RD, Newell JB, Pohost GM. The relationship between proton nuclear magnetic resonance relaxation parameters and myocardial perfusion with acute coronary arterial occlusion and reperfusion. Circulation. 1985; 71:823–828.
63. Cury RC, Shash K, Nagurney JT, Rosito G, Shapiro MD, Nomura CH, Abbara S, Bamberg F, Ferencik M, Schmidt EJ, Brown DF, Hoffmann U, Brady TJ. Cardiac Magnetic Resonance With T2-Weighted Imaging Improves Detection of Patients With Acute Coronary Syndrome in the Emergency Department. Circulation. 2008; 118(8):837–44.
64. Friedrich MG, Abdel-Aty H, Taylor A, Schulz-Menger J, Messroghli D, Dietz R The salvaged area at risk in reperfused acute myocardial infarction as visualized by cardiovascular magnetic resonance. J Am Coll Cardiol. 2008; 51:1581–1587.
65. Friedrich MG, Sechtem U, Schulz-Menger J, Holmvang G, Alakija P, Cooper LT, White JA, Abdel-Aty H, Gutberlet M, Prasad S, Aletras A, Laissy JP, Paterson I, Filipchuk NG, Kumar A, Pauschinger M, Liu P International Consensus Group on Cardiovascular Magnetic Resonance in Myocarditis. Cardiovascular magnetic resonance in myocarditis: A JACC White Paper. J Am Coll Cardiol. 2009; 53:1475-1487.
66. Butler CR, Thompson R, Haykowsky M, Toma M, Paterson I. Cardiovascular magnetic resonance in the diagnosis of acute heart transplant rejection: a review. J Cardiovasc Magn Reson. 2009; 11:7.
67. Guo H, Au WY, Cheung JS, Kim D, Jensen JH, Khong PL, Chan Q, Chan KC, Tosti C, Tang H, Brown TR, Lam WW, Ha SY, Brittenham GM, Wu EX. Myocardial T2 quantitation in patients with iron overload at 3 Tesla. J Magn Reson Imaging. 2009; 30(2):394–400.
68. Mentzer WC, Kan YW. Prospects for research in hematologic disorders: sickle cell disease and thalassemia. J Am Med Assoc. 2001; 285:640–642.

69. Tuzmen S, Schechter AN. Genetic diseases of hemoglobin: diagnostic methods for elucidating beta-thalassemia mutations. Blood Rev. 2001; 15:19–29.
70. Modell B, Khan M, Darlison M. Survival in beta thalassaemia major in the UK: data from the UK Thalassaemia Register. Lancet. 2000; 355:2051–2052.
71. Gillis P, Roch A, Brooks RA. Corrected equations for susceptibility induced T2-shortening. J Magn Reson. 1999; 137:402–407.
72. Simonetti OP, Finn JP, White RD, Laub G, Henry DA. "Black blood" T2-weighted inversion-recovery MR imaging of the heart. Radiology. 1996; 199:49–57.
73. Abdel-Aty H, Simonetti O, Friedrich MG. T2-weighted cardiovascular magnetic resonance imaging. J Magn Reson Imaging. 2007; 26:452–459.
74. Arai AE. Using magnetic resonance imaging to characterize recent myocardial injury: utility in acute coronary syndrome and other clinical scenarios. Circulation. 2008; 118:795–796.
75. Giri S, Chung YC, Merchant A, Mihai G, Rajagopalan S, Raman SV, Simonetti OP. T2 quantification for improved detection of myocardial edema. J Cardiovasc Magn Reson. 2009; 11:56.
76. Maizlin ZV, Clement JJ, Patola WB, Fenton DM, Gillies JH, Vos PM, Jacobson JA. T2 Mapping of Articular Cartilage of Glenohumeral Joint with Routine MRI Correlation—Initial Experience. Musculoskelet J Hospital Spec Surg. 2009; 5: 61–66.
77. He T, Gatehouse PD, Anderson LJ, Tanner M, Keegan J, Pennell DJ, Firmin DN. Development of a Novel Optimized Breathhold Technique for Myocardial T2 measurement in Thalassemia. J Magn Reson Imaging. 2006; 24:580–585.
78. Busse RF, Hariharan H, Vu A, Brittain JH. Fast Spin Echo Sequences With Very Long Echo Trains: Design of Variable Refocusing Flip Angle Schedules and Generation of Clinical T2 Contrast. Magn Reson Med. 2006; 55:1030–1037.
79. Huang TY, Liu YJ, Stemmer A, Poncelet BP. T2 Measurement of the Human Myocardium Using a T2-Prepared Transient-State TrueFISP Sequence. Magn Reson Med. 2007; 57:960–966.
80. Foltz WD, Al-Kwifi O, Sussman MS, Stainsby JA, Wright GA. Optimized Spiral Imaging for Measurement of Myocardial T2 Relaxation. Magn Reson Med. 2003; 49:1089–1097.
81. Stainsby JA, Ramanan V, Slavin GS, Wright GA. A comparison of methods for T2-mapping of the Myocardium. J Cardiovasc Magn Reson. 2010; 12(Suppl 1) P227.

82. Feinberg DA, Hoenninger JC, Crooks LE, Kaufman L, Watts JC, Arakawa M. Inner volume MR imaging: technical concepts and their application. Radiology. 1985; 156(3):743–747.
83. Feinberg DA, Turner R, Jakab PD, von Kienlin M. Echo-planar imaging with asymmetric gradient modulation and inner-volume excitation. Magn Reson Med. 1990; 13(1):162–169.
84. Mitsouras D, Mulkern RV, Rybicki FJ. Strategies for inner volume 3D fast spin echo magnetic resonance imaging using nonselective refocusing radio frequency pulses. Med Phys. 2006; 33(1):173–186.
85. Alley MT, Pauly JM, Sommer FG, Pelc NJ. Angiographic imaging with 2D RF pulses. Magn Reson Med. 1997; 37(2):260–267.
86. Saritas EU, Cunningham CH, Lee JH, Han ET, Nishimura DG. DWI of the spinal cord with reduced FOV single-shot EPI. Magn Reson Med. 2008; 60(2):468–473.
87. Block W, Pauly J, Kerr A, Nishimura D. Consistent fat suppression with compensated spectral-spatial pulses. Magn Reson Med. 1997; 38: 198–206.
88. Fredrickson JO, Meyer CH, Pelc NJ. Flow effects of spectral spatial excitation. In Proceedings of the 5th meeting of the ISMRM 1997. Vancouver, p. 113.
89. Schneider JT, Kalayciyan R, Haas M, Herrmann SR, Ruhm W, Hennig J, Ullmann P. Inner-volume imaging in vivo using three-dimensional parallel spatially selective excitation. Magn Reson Med. 2013; 69(5):1367–1378.
90. Pauly J, Le Roux P, Nishimura D, Macovski A. Parameter relations for the Shinnar-Le Roux selective excitation pulse design algorithm. IEEE Trans Med Imaging. 1991; 10(1):53–65.
91. Mitchell MD, Kundel HL, Axel L, Joseph PM. Agarose as a tissue equivalent phantom material for NMR imaging. Magn Reson Imaging. 1986; 4(3):263–266.
92. Guo H, Au WY, Cheung JS, Kim D, Jensen JH, Khong PL, Chan Q, Chan KC, Tosti C, Tang H, Brown TR, Lam WW, Ha SY, Brittenham GM, Wu EX. Myocardial T2 quantitation in patients with iron overload at 3 Tesla. J Magn Reson Imaging. 2009; 30(2):394–400.
93. von Knobelsdorff-Brenkenhoff F, Prothmann M, Dieringer MA, Wassmuth R, Greiser A, Schwenke C, Niendorf T, Schulz-Menger J. Myocardial T1 and T2 mapping at 3 T: reference values, influencing factors and implications. J Cardiovasc Magn Reson. 2013; 15(1):53.
94. Henning J. Multiecho Imaging Sequences with Low Refocusing Flip Angles. J Magn Reson. 1988; 78, 397–407.

95. Bonny JM, Zanca M, Boire JY, Veyre A. T2 maximum likelihood estimation from multiple spin-echo magnitude images. Magn Reson Med. 1996; 36(2):287–293.
96. Gibiino F, Lechner-Greite S, Schirmer T, Landini L, Janich MA. Inner volume T2 mapping of myocardium for MRI. Abstract 47 Eur Soc Magn Res Med Biol. 2013.
97. Lebel RM, Wilman, AH, Transverse relaxometry with stimulated echo compensation. Magn Reson Med. 2010; 64: 1005–1014.
98. Bammer R, Auer M, Keeling SL, Augustin M, Stables LA, Prokesch RW, Stollberger R, Moseley ME, Fazekas F. Diffusion tensor imaging using single-shot SENSE-EPI. Magn Reson Med. 2002; 48: 128–136.
99. Bydder M, Atkinson D, Larkman DJ, Hill DL, Hajnal JV. SMASH navigators. Magn Reson Med. 2003; 49: 493–500.
100. Hatabu H, Alsop DC, Listerud J, Bonnet M, Gefter WB. T2* and proton density measurement of normal human lung parenchyma using submillisecond echo time gradient echo magnetic resonance imaging. Eur J Radiol. 1999; 29:245–252.
101. Stock KW, Chen Q, Hatabu H, Edelman RR. Magnetic resonance T2* measurements of the normal human lung in vivo with ultra-short echo times. Magn Reson imaging. 1999; 17:997–1000.
102. Yu J, Xue Y, Song HK. Comparison of lung T2* during free-breathing at 1.5 T and 3.0 T with ultrashort echo time imaging. Magn Reson Med. 2011; 66:248–254.
103. Wild JM, Marshall H, Bock M, Schad LR, Jakob PM, Puderbach M, Molinari F, Van Beek EJ, Biederer J. MRI of the lung (1/3): methods. Insights Imaging. 2012 Aug;3(4):345-53.
104. Biederer J, Beer M, Hirsch W, Wild J, Fabel M, Puderbach M, Van Beek EJ. MRI of the lung (2/3). Why … when … how? Insights Imaging. 2012 Aug;3(4):355-71.
105. Biederer J, Mirsadraee S, Beer M, Molinari F, Hintze C, Bauman G, Both M, Van Beek EJ, Wild J, Puderbach M. MRI of the lung (3/3)-current applications and future perspectives. Insights Imaging. 2012 Aug;3(4):373-86
106. Wielpütz M, Kauczor H. MRI of the lung: state of the art. Diagn Interv Radiol. 2012; 18:344-353.
107. Weick S, Breuer FA, Ehses P, Völker M, Hintze C, Biederer J and Jakob PM. DC-gated high resolution three-dimensional lung imaging during free-breathing. J Magn Reson Imaging. 2013; 37: 727–732.

108. Rajaram S, Swift AJ, Capener D, Telfer A, Davies C, Hill C, Condliffe R, Elliot C, Hurdman J, Kiely DG, Wild JM. Lung morphology assessment with balanced steady-state free precession MR imaging compared with CT. Radiology. 2012 May;263(2):569-77.

109. Bieri O. Ultra-fast steady state free precession and its application to in vivo $_1$H morphological and functional lung imaging at 1.5 Tesla. Magn Reson Med. 2013 Jun 28.

110. Hatabu H, Gaa J, Tadamura E, Edinburgh KJ, Stock KW, Garpestad E, Edelman RR. MR imaging of pulmonary parenchyma with a half-Fourier single-shot turbo spin-echo (HASTE) sequence. Eur J Radiol. 1999 Feb;29(2):152-9.

111. Bergin CJ, Pauly JM, Macovski A. Lung parenchyma: projection reconstruction MR imaging. Radiology. Jun 1991; 179(3):777-781.

112. Johnson KM, Fain SB, Schiebler ML and Nagle S. Optimized 3D ultrashort echo time pulmonary MRI. Magn Reson Med. 2012 Dec.

113. Kauczor H, Surkau R, Roberts T. MRI using hyperpolarized noble gases. Eur Radiol 1998; 8:820–827.

114. Mugler JP III, Driehuys B, Brookeman JR, et al. MR imaging and spectroscopy using hyperpolarized 129Xe gas: preliminary human results. Magn Reson Med 1997; 37:809–815.

115. Pullinger B, Profka H, Ardenkjaer-Larsen JH, Kuzma NN, Kadlecek S, Rizi RR. Metabolism of hyperpolarized [1–13C]pyruvate in the isolated perfused rat lung-An ischemia study. NMR Biomed 2012; 25:1113–1118.

116. Ohno Y, Hatabu H, Murase K, Higashino T, Nogami M, Yoshikawa T, Sugimura K. Primary pulmonary hypertension: 3D dynamic perfusion MRI for quantitative analysis of regional pulmonary perfusion. AJR Am J Roentgenol 2007; 188:48–56.

117. Mai VM, Berr SS. MR perfusion imaging of pulmonary parenchyma using pulsed arterial spin labeling techniques: FAIRER and FAIR. J Magn Reson Imaging 1999; 9:483–487.

118. Lewis CE, Prato FS, Drost DJ, Nicholson RL. Comparison of respiratory triggering and gating techniques for the removal of respiratory artifacts in MR imaging. Radiology. 1986;160:803– 810.

119. Gibiino F, Sacolick L, Menini A, Landini L, Wiesinger F. Free-breathing lung MRI using 3D radial zero-TE imagin. In Proceedings: European Society of Magnetic Resonance in Medicine and Biology, October 2013.

120. Menini A, Gibiino F, Odille F, Sacolick L, and Wiesinger F. Free-breathing, zero TE MRI for 3D respiratory motion quantification. In Proceedings: European Society of Magnetic Resonancein Medicine and Biology, October 2013.
121. Morita S, Suzuki K, Machida H, Fujimura M, Ohnishi T, Imura C, Ueno E.Compression belt for navigator-triggered trueFISP whole-heart coronary magnetic resonance angiography: study in healthy volunteers. Magn Reson Med Sci. 2008;7(2):79-83.
122. Hafner S. Fast imaging in liquids and solids with the back-projection Low Angle ShoT (BLAST) technique. Magnetic Resonance Imaging. 1994; 12(7):1047-1051.
123. Madio DP, Lowe IJ. Ultra-fast imaging using low flip angles and fids. Magn Reson Med. 1995; 34: 525–529.
124. Wu Y, Ackerman JL, Chesler DA, Graham L, Wang Y, Glimcher MJ. Density of organic matrix of native mineralized bone measured by water- and fat-suppressed proton projection MRI. Magn Reson Med. 2003;50:59–68.
125. Weiger M, Pruessmann KP, Hennel F. MRI with zero echo time: hard versus sweep pulse excitation. Magn Reson Med. 2011 Aug;66(2):379-89.
126. Grodzki DM, Jakob PM, Heismann B. Ultrashort echo time imaging using pointwise encoding time reduction with radial acquisition (PETRA). Magn Reson Med. 2012; 67:510–518.
127. Sacolick L, Wiesinger F, Kelley DAC, Khalighi MM, Rutt BK. 7 Tesla zero-echo time imagingn of the head. Abstract 52, ESMRMB 2013.
128. Grodzki DM, Jakob PM, Heismann B. Correcting slice selectivity in hard pulse sequences. J Magn Reson. 2012 Jan;214(1):61-7
129. Rahmer J, Börnert P, Groen J, Bos C. Three-dimensional radial ultrashort echo-time imaging with T_2 adapted sampling. Magn Reson Med. 2006; 55: 1075–1082.
130. Wong STS, Roos MS. A strategy for sampling on a sphere applied to 3D selective RF pulse design. MRM. 32:778-784 (1994).
131. Nehrke K, Manke D. Advanced Navigator Techniques. International journal of Bioelectromagnetism. 2000, Volume 2, Number 2.
132. Brau AC, Brittain JH. Generalized self-navigated motion detection technique: Preliminary investigation in abdominal imaging. Magn Reson Med. 2006 Feb;55(2):263-70.

133. Larson AC, White RD, Laub G, McVeigh ER, Li D, Simonetti OP.Self-gated cardiac cine MRI. Magn Reson Med. 2004 Jan;51(1):93-102.
134. Crete F, Dolmiere T, Ladret P, Nicolas M. The Blur Effect: Perception and Estimation with a new no-reference perceptual blur metric. Published in "SPIE Electronic Imaging Symposium Conf Human Vision and Electronic Imaging, San Jose : États-Unis d'Amérique (2007)".
135. Lustig M, Donoho D, Pauly JM. Sparse MRI: The application of compressed sensing for rapid MR imaging. Magn Reson Med. 2007 Dec;58(6):1182-95.
136. Block KT, Uecker M, Frahm J. Undersampled radial MRI with multiple coils. Iterative image reconstruction using a total variation constraint. Magn Reson Med. 2007; 57:1086—1098.
137. Knoll F, Clason C, Bredies K, Uecker M, Stollberger R. Parallel imaging with nonlinear reconstruction using variational penalties. Magn Reson Med. 2012 Jan;67(1):34-41.
138. Tsao J, Boesiger P, Pruessmann KP. k-t BLAST and k-t SENSE: dynamic MRI with high frame rate exploiting spatiotemporal correlations. Magn Reson Med. 2003; 50(5):1031–1042.
139. Odille F, Vuissoz PA, Marie PY, Felblinger J. Generalized reconstruction by inversion of coupled systems (GRICS) applied to free-breathing MRI. Magn Reson Med. 2008; 60(1):146–157.
140. Usman M, Atkinson D, Odille F, Kolbitsch C, Vaillant G, Schaeffter T, Batchelor PG, Prieto C. Motion corrected compressed sensing for free-breathing dynamic cardiac MRI. Magn Res Med. 2013; 70(2):504–516.